SURFER v3.0 : a fast model with ice sheet tipping points and carbon cycle feedbacks for short and long-term climate scenarios

Victor Couplet[1], Marina Martínez Montero[1], and Michel Crucifix[1]

[1]Earth and Life Institute, UCLouvain, Louvain-la-Neuve, Belgium

Correspondence: Victor Couplet (victor.couplet@uclouvain.be)

Abstract. Simple climate models that are computationally inexpensive, transparent, and easy to modify are useful for assessing climate policies in the presence of uncertainties. This motivated the creation of SURFER v2.0, a model designed to estimate the impact of CO_2 emissions and solar radiation modification on global mean temperatures, sea-level rise, and ocean pH. However, SURFER v2.0 is unsuitable for simulations beyond a few thousand years because it lacks some carbon cycle processes. This is problematic for assessing the long-term evolution of the Earth system, particularly the dynamics of ice sheets and the resulting sea level rise. Here, we present SURFER v3.0, an extension to SURFER v2.0 that allows for accurate simulation of the climate, carbon cycle, and sea level rise on time scales ranging from decades to millions of years. We incorporated in the model a dynamic cycling of alkalinity in the ocean, a carbonate sediments reservoir, and weathering fluxes. With these additions, we show that SURFER v3.0 reproduces results from a large class of models, ranging from centennial CMIP6 projections to 1 Myr runs performed with the cGENIE model of intermediate complexity. We show that compared to SURFER v2.0, including long-term carbon-cycle processes in SURFER v3.0 leads to a stabilisation of the Greenland ice sheet for the middle of the road emission scenarios, and a significant reduction in sea level rise contribution from Antarctica for high emissions scenarios.

1 Introduction

Human activities have significantly altered Earth's climate by releasing greenhouse gases, primarily carbon dioxide (CO_2) and methane (CH_4), into the atmosphere at unprecedented rates (IPCC, 2021a). The consequences of these emissions are already palpable, with 2024 marking the warmest year on record (WMO, 2025). Moreover, the frequency and intensity of extreme weather events such as heatwaves, droughts, and heavy precipitations have increased and are projected to increase further under global warming (IPCC, 2021b). While these impacts are immediate and observable, others unfold over longer time frames. For instance, the melting polar ice caps will contribute to sea level rise for centuries, and even millennia, after emissions of greenhouse gases are reduced or stopped (Clark et al., 2016; Breedam et al., 2020). There is also growing concern over climate tipping points, where potentially abrupt and irreversible changes could occur and lead to cascades of unforeseen consequences in the long term trajectories of the Earth system (Lenton et al., 2008, 2019; Armstrong McKay et al., 2022; Steffen et al., 2018).

Making informed decisions about climate change thus necessitates a comprehensive examination across multiple temporal scales, to balance the immediate needs of current populations with the imperative of safeguarding the planet's habitability for

future generations (Raworth, 2012). To this end, climate models are indispensable for scientists and policymakers. They come in different sizes and complexities (see section 3.2 in Goosse, 2015). On the one side of the complexity spectrum, state-of-the-art Earth system models include detailed representation of physical and biogeochemical processes. However, due to their size and complexity, they are hard to analyse and computationally expensive to run, with most simulations ending in 2100 (for example, this is the case in most CMIP6 experiments). On the other side of the spectrum, conceptual box models trade complexity and spatial resolution for speed and simplicity. They provide valuable insights into fundamental climate processes and feedbacks, facilitating transparent and intuitive assessments of long-term climate trends. Due to their low computational cost, they can be run many times, with different choices of parameters and for different forcing scenarios. This allows an extensive exploration of mitigation and adaptation strategies, such as to take into account possible errors caused by simplifications and other lacks of knowledge.

This is the spirit in which SURFER was designed (Martínez Montero et al., 2022). SURFER v2.0 is a model based on nine ordinary differential equations designed to estimate global mean temperature increase, sea level rise and ocean acidification in response to CO_2 emissions and aerosols injections. It is fast, easy to understand and modify, making it appropriate for use in policy assessments. For example, in Montero et al. (2023), it helped assess the long-term sustainability of short term climate policies based on a novel commitment metric. Yet, SURFER v2.0 lacks some processes in its carbon cycle implementation. It can only simulate quantities reliably for up to two or three millennia, and only accounts for carbon dioxide emissions in the carbon cycle. Here, we introduce an extended version of the model with new processes, SURFER v3.0. Among other things, we have added: a representation of atmospheric methane, a distinction between land-use and fossil emissions, an additional oceanic layer, a dependence of the solubility and dissociation constants on temperature and pressure, a dynamic representation of alkalinity, a sediments box, and weathering processes.

The present paper is structured as follow. We explain in detail the new additions of SURFER v3.0 in section 2. In section 3, we compare the results of SURFER v3.0 to other models on time scales ranging from centuries to a million year. We first show that SURFER v3.0 can reproduce the historical record. Then, we show that SURFER v3.0 is in the range of IPCC class models for different quantities modelled up to 2100 and 2300 AD. We next compare the CO_2 draw-down computed by SURFER over 10000 years to models that participated in the LTMIP project. Lastly, we compare SURFER v3.0 outputs to 1 Myr runs performed with the cGENIE climate model of intermediate complexity. In section 4, we show that including new processes in the carbon cycle reduces the committed sea level rise (SLR) estimations on millennial time scales compared to SURFER v2.0. In section 5 we discuss the advantages and limitations of our model. Finally, in section 6, we conclude and provide some perspectives on future research.

2 Model specification

The nine ordinary differential equations of SURFER v2.0 describe the exchanges of carbon between four different reservoirs (atmosphere, upper ocean layer, deeper ocean layer and land), the evolution of temperature anomalies of two different reservoirs

(upper ocean layer and deeper ocean layer), the volumes of Greenland and Antarctic ice sheets, and the sea level rise related to glaciers (Martínez Montero et al., 2022). In version v3.0, we have added :

60   – an ocean layer of intermediate depth,

    – a sediment box with $CaCO_3$ accumulation and burial fluxes,

    – dynamic alkalinity cycling between the 3 ocean layers,

    – an explicit description of the soft-tissue and carbonate pumps in the ocean,

    – volcanic outgassing and weathering fluxes,

65   – an equation for the methane evolution in the atmosphere,

    – a temperature and depth (pressure) dependence of the solubility and dissociation constants,

    – a second equation for the land reservoir that allows for a better distinction between land-use and fossil greenhouse gas emissions.

SURFER v3.0 now consists of 17 coupled ordinary differential equations, while keeping its original architecture. It contains
70 three main components, for, respectively, the carbon cycle, climate, and the sea-level. The model is forced by land-use and fossil emissions of CO_2 and CH_4, and by aerosols injections. State variables defining the model components, carbon and energy fluxes between those components, and forcings are schematically summarised in Figure 1.

In this section, we explain in detail the model implementation. Sub-sections 2.1, 2.2, and 2.3 focus respectively on the implementation of the the carbon, climate and sea-level rise components. In sub-section 2.4 we show how the model was
75 calibrated and how the initial conditions are chosen. Sub-section 2.5 discusses the algorithmic implementation and speed.
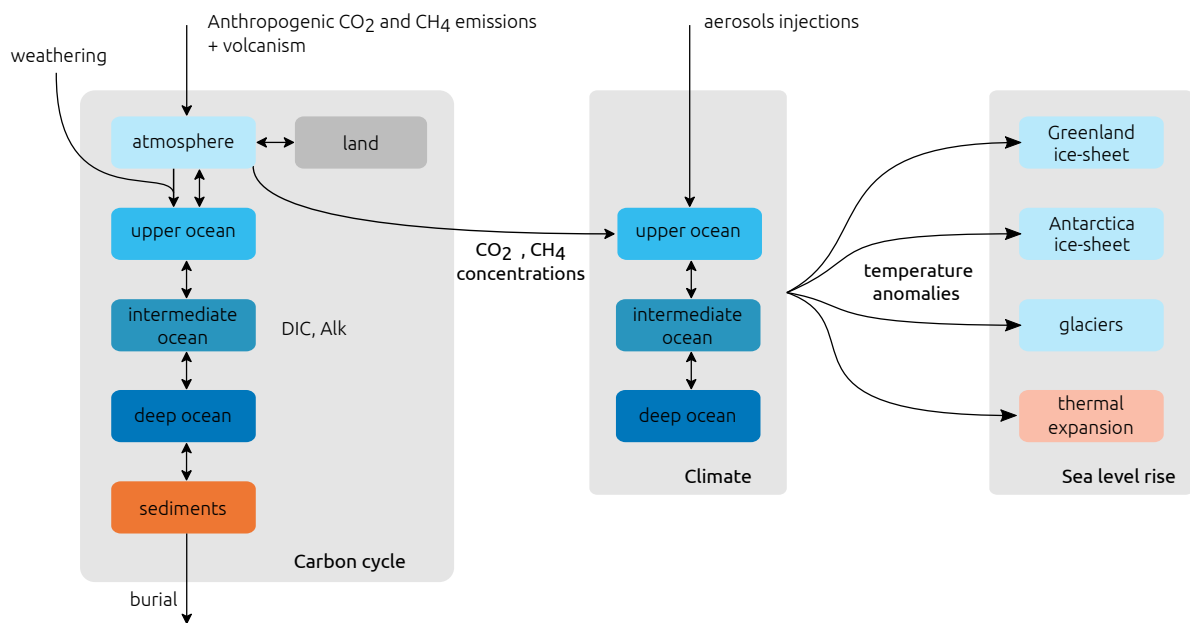
Figure 1. Conceptual diagram of SURFER v3.0.

2.1 Carbon cycle component

The equations for the carbon cycle component of SURFER v3.0 are given by

$$\frac{dM_A}{dt} = V + E_{\text{fossil}}^{CO_2} + E_{\text{land-use}}^{CO_2} - F_{A\to U} - F_{A\to L} + F_{CH_4,\text{ox}} - E_{\text{natural}}^{CH_4} - F_{\text{weathering}} \,, \tag{1}$$

$$\frac{dM_A^{CH_4}}{dt} = E_{\text{fossil}}^{CH_4} + E_{\text{land-use}}^{CH_4} + E_{\text{natural}}^{CH_4} - F_{CH_4,\text{ox}} \,, \tag{2}$$

$$\frac{dM_L}{dt} = F_{A\to L} - E_{\text{land-use}}^{CO_2} - E_{\text{land-use}}^{CH_4} \,, \tag{3}$$

$$\frac{dM_U}{dt} = F_{A\to U} - F_{U\to I} + F_{\text{river}} \,, \tag{4}$$

$$\frac{dM_I}{dt} = F_{U\to I} - F_{I\to D} \,, \tag{5}$$

$$\frac{dM_D}{dt} = F_{I\to D} - F_{\text{acc}} \,, \tag{6}$$

$$\frac{d\tilde{Q}_U}{dt} = -\tilde{F}_{U\to I} + \tilde{F}_{\text{river}} \,, \tag{7}$$

$$\frac{d\tilde{Q}_I}{dt} = \tilde{F}_{U\to I} - \tilde{F}_{I\to D} \,, \tag{8}$$

$$\frac{d\tilde{Q}_D}{dt} = \tilde{F}_{I\to D} - \tilde{F}_{\text{acc}} \,, \tag{9}$$

$$\frac{dM_S}{dt} = F_{\text{acc}} - F_{\text{burial}} \,. \tag{10}$$

They describe the fluxes of carbon between six reservoirs, the atmosphere (A), the land (L), the upper (U), intermediate (I), and deep (D) ocean layers, and the deep sea sediments (S). M_A and $M_A^{CH_4}$ are the masses of carbon in the atmosphere in CO_2 and CH_4 forms respectively. M_L is the mass of carbon on land (in vegetation and soils) and M_S is the mass of carbon in the erodible $CaCO_3$ deep sea sediments. M_U, M_I and M_D are the masses of dissolved inorganic carbon in the ocean layers, while $\tilde{Q}_U$, $\tilde{Q}_I$, $\tilde{Q}_D$ are total alkalinities. All these quantities are expressed in PgC, and the fluxes in $PgC\,yr^{-1}$ (equation 14 explains what this means for alkalinity).

Variable names are chosen to be self-explanatory, and tildes indicate quantities and fluxes related to alkalinity. Volcanism (V) and anthropogenic CO_2 emissions ($E_{\text{fossil}}^{CO_2}$, $E_{\text{land-use}}^{CO_2}$) increase the CO_2 content of the atmosphere. Methane anthropogenic emissions ($E_{\text{fossil}}^{CH_4}$, $E_{\text{land-use}}^{CH_4}$) as well as natural emissions ($E_{\text{natural}}^{CH_4}$) increase the CH_4 content in the atmosphere. Methane is rapidly oxidized into CO_2 ($F_{CH_4,\text{ox}}$). Atmosphere and land reservoirs exchange CO_2 through photosynthesis and respiration (combined in $F_{A\to L}$). Weathering ($F_{\text{weathering}}$) removes carbon dioxide from the atmosphere through chemical reactions with rocks and minerals. The products of these reactions are then transported to the ocean by the rivers (F_{river}, $\tilde{F}_{\text{river}}$). Carbon is exchanged between the different layers of the ocean by mixing and the different carbon pumps ($F_{U\to I}$, $F_{I\to D}$, $\tilde{F}_{U\to I}$, $\tilde{F}_{I\to D}$). A fraction of the carbon accumulates as sediments on the ocean floor (F_{acc}, $\tilde{F}_{\text{acc}}$) where it can be permanently buried (F_{burial}) and removed from the system. Ultimately, plate tectonics movements transport this carbon in the mantle of the Earth (not explicitly modelled in SURFER) where it will be transformed back to CO_2 and eventually emitted in the atmosphere through volcanism, closing the cycle (for a detailed description of the full carbon cycle, see e.g., Archer, 2010)

105   We detail the implementation of the above fluxes in sections 2.1.4 to 2.1.9. Before that, we motivate the addition of a
new oceanic layer (section 2.1.1) and discuss the treatment of alkalinity (section 2.1.2) and of the solubility and dissociation
constants (section 2.1.3).

2.1.1   Additional ocean layer

SURFER v2.0 used two ocean layers: an upper layer (U) of 150 m depth and a deep layer (D) of 3000 m depth. In SURFER
110   v3.0 we use three ocean layers: an upper layer (U) of 150 m depth, an intermediate layer (I) of 500 m depth, and a deep
layer (D) of 3150 m depth. Overall, the total ocean depth in SURFER v3.0 is greater than in SURFER v2.0 and closer to
the global mean estimate ($\sim$3700 m). The new intermediate layer allows a smoother transition between the upper and deeper
layers which have different properties (temperature, salinity, pH, ...), see Figure 3. It also allows a faster carbon transport out of
the upper layer, because the exchange with the new intermediate layer is faster than with the old deep layer. This modification
115   partly fixes two problems we had in SURFER v2.0, and which are visible in Figure 7: CO_2 uptake by the ocean was too
slow, and the surface pH decreased too fast (surface ocean acidified too quickly, see Martínez Montero et al., 2022). Indeed,
since the dissolved CO_2 now leaves the upper layer quicker, the surface ocean can absorb CO_2 from the atmosphere at faster
rates. Moreover, with reduced "stagnation" of dissolved CO_2 in the upper layer, surface acidity increases slower (pH decreases
slower). Differences in atmosphere-to-ocean carbon flux and surface ocean pH between SURFER v2.0 and SURFER v3.0 are
120   shown in Figure 7.

2.1.2   Total alkalinity

Dissolved inorganic carbon (DIC) is defined as the sum of the carbonate species: carbonate ions CO_3^{2-}, bicarbonate ions HCO_3^-
and $H_2CO_3^*$ which represents a mix of aqueous carbon dioxide, CO_2(aqueous) and carbonic acid H_2CO_3. For concentrations,
we have

125   $$DIC = [H_2CO_3^*] + [HCO_3^-] + [CO_3^{2-}].   \quad (11)$$

Alkalinity, on the other hand, is defined as the excess of bases over acids in water (Middelburg et al., 2020):

$$Alk = [HCO_3^-] + 2[CO_3^{2-}] + [OH^-] - [H^+] + [B(OH)_4^-] + \text{minor bases}.   \quad (12)$$

Intuitively, it measures the ability of a water mass to resist changes in pH when an acid is added. This happens for example
when excess CO_2 in the atmosphere dissolves in seawater (see eqs R1-R3). Alkalinity thus plays a crucial role in buffering
130   ocean acidification, which is important for many marine organisms who depend on stable pH levels for their survival and
growth (Ross et al., 2011). Being related to the concentrations of dissolved inorganic carbon species (CO_3^{2-} and HCO_3^-),
alkalinity also has a role in regulating the oceanic uptake of atmospheric CO_2. In SURFER v2.0, alkalinity is considered
constant and is furthermore approximated by carbonate alkalinity $Alk \approx Alk_C = [HCO_3^-] + 2[CO_3^{2-}]$. In SURFER v3.0, we
include $CaCO_3$ sediment dissolution, and this requires having variable alkalinity (equations 7-9). We estimate alkalinity based
135   on the carbonate, borate and water self-ionisation alkalinity (CBW), which includes the contributions of the hydroxide ions

6

$[\mathrm{OH}^-]$, free protons $[\mathrm{H}^+]$ and borate ions $[\mathrm{B(OH)_4^-}]$:

$$\mathrm{Alk} \approx \mathrm{Alk}_{CBW} = [\mathrm{HCO_3^-}] + 2[\mathrm{CO_3^{2-}}] + [\mathrm{OH}^-] - [\mathrm{H}^+] + [\mathrm{B(OH)_4^-}]. \tag{13}$$

This treatment produces more accurate computations of the concentration of chemical species than SURFER v2.0, specifically $[\mathrm{H}^+]$ and thus pH, but comes at a greater computational cost. See appendix C for more details.

140   We use units of PgC for the variables representing alkalinity $\tilde{Q}_\mathrm{U}$, $\tilde{Q}_\mathrm{I}$, and $\tilde{Q}_\mathrm{D}$ even though our working approximation now include terms that do no contain carbon. We do this for purely practical reasons, as all other variables of the carbon cycle component are also in PgC. The alkalinity concentration Alk_i for the layer $i \in \{\mathrm{U, I, D}\}$ in $\mu\mathrm{mol\,kg^{-1}}$, a more common unit, is simply given by

$$\mathrm{Alk}_i = \frac{\tilde{Q}_i}{W_i \bar{m}_\mathrm{C}} \times 10^{18}, \tag{14}$$

145   where W_i is the weight in kg of ocean layer i, and $\bar{m}_\mathrm{C}$ is the molar mass of carbon in $\mathrm{mol\,kg^{-1}}$. This is the same equation as for the conversion from dissolved inorganic carbon mass in PgC to concentration in $\mu\mathrm{mol\,kg^{-1}}$

$$\mathrm{DIC}_i = \frac{M_i}{W_i \bar{m}_\mathrm{C}} \times 10^{18}. \tag{15}$$

The weight of layer i is given by

$$W_i = \frac{h_i \bar{m}_\mathrm{w} m_\mathrm{O}}{h_\mathrm{U} + h_\mathrm{I} + h_\mathrm{D}}, \tag{16}$$

150   with $\bar{m}_\mathrm{w}$ the molar mass of water and m_O the number of moles in the ocean.

2.1.3   Solubility and dissociation constants

When atmospheric CO_2 enters the ocean, it undergoes a series of chemical reactions

$$\mathrm{CO_{2(gas)} + H_2O} \quad \rightleftharpoons \quad \mathrm{H_2CO_3^*}, \tag{R1}$$

$$\mathrm{H_2CO_3^*} \quad \rightleftharpoons \quad \mathrm{HCO_3^- + H^+}, \tag{R2}$$

155
$$\mathrm{HCO_3^-} \quad \rightleftharpoons \quad \mathrm{CO_3^{2-} + 2H^+}. \tag{R3}$$

These reactions are fast and we assume that they are in equilibrium (Sarmiento and Gruber, 2006). The relationships between the equilibrium concentrations of the different chemical species are determined by the dissociation constants :

$$K_1 = \frac{[\mathrm{H^+}][\mathrm{HCO_3^-}]}{[\mathrm{H_2CO_3^*}]}, \tag{17}$$

$$K_2 = \frac{[\mathrm{H^+}][\mathrm{CO_3^{2-}}]}{[\mathrm{HCO_3^-}]}, \tag{18}$$

160   Similarly, we have for the equilibrium concentrations of OH^- and $\mathrm{B(OH)_4^-}$

$$K_\mathrm{w} = [\mathrm{H^+}][\mathrm{OH^-}], \tag{19}$$

$$K_\mathrm{b} = \frac{[\mathrm{H^+}][\mathrm{B(OH)_4^-}]}{[\mathrm{H_3BO_3}]}, \tag{20}$$

where we additionally assume that the total equilibrium boron concentration is proportional to salinity (Uppström, 1974) :

$$TB = \left[B(OH)_4^-\right] + [H_3BO_3] = c_b \cdot S, \tag{21}$$

with $c_b = 11.88\,\mu\text{mol kg}^{-1}\text{psu}^{-1}$. The solubility of CO_2 in seawater, K_0, relates the concentration of $H_2CO_3^*$ and the partial pressure of dissolved CO_2, p_{CO_2} :

$$K_0 = \frac{[H_2CO_3^*]}{p_{CO_2}}. \tag{22}$$

In SURFER v2.0, K_0, K_1 and K_2 were constant. In SURFER v3.0, K_0, K_1, K_2, K_b, and K_w depend on temperature and salinity based on Weiss (1974); Mehrbach et al. (1973); Dickson and Millero (1987); Millero (1995); Dickson (1990). Salinity is assumed to be invariant on time, so we effectively only have a dependence on temperature . We also introduce a pressure (depth) dependence for K_1, K_2, K_w, and K_b, based on Millero (1995). This allows a better characterisation of pH in the deep ocean layer. Details on the parametrisations are in appendix B.

2.1.4 $F_{A \to U}$

We derive an expression for the atmosphere-to-ocean flux $F_{A \to U}$ in a slightly different way than in SURFER v2.0. The sea-air CO_2 exchange is proportional to the difference in CO_2 partial pressure between the atmosphere and the surface ocean layer (Goosse, 2015). We have

$$F_{A \to U} = \bar{m}_C A_O \rho k K_0 (p_{CO_2}^A - p_{CO_2}^U), \tag{23}$$

where A_O is the ocean surface area (in m^2), ρ is the density of sea-water (in kg m^3), $\bar{m}_C$ is the molar mass of carbon (in kg mol^{-1}), k is the gas transfer velocity (in m yr^{-1}) and K_0 is the solubility constant of CO_2 (in $\text{mol kg}^{-1}\text{atm}^{-1}$). This same expression is used by Lenton (2000) and Zeebe (2012), for carbon cycles models of similar complexity, with a multiplication by the molar mass of carbon $\bar{m}_C$ added here to obtain a flux in kg yr^{-1} instead of mol yr^{-1}. We can express $p_{CO_2}^A$ and $p_{CO_2}^U$ in terms of model variables M_A and M_U

$$F_{A \to U} = \bar{m}_C A_O \rho k K_0 (p_{CO_2}^A - p_{CO_2}^U), \tag{24}$$

$$= \bar{m}_C A_O \rho k K_0 \left(\frac{M_A}{m_A \bar{m}_C} \cdot 1\,\text{atm} - \frac{M_U'}{W_U \bar{m}_C K_0}\right), \tag{25}$$

$$= \frac{A_O \rho k}{m_A} K_0 \left(M_A \cdot 1\,\text{atm} - \frac{m_A}{W_U K_0} \frac{M_U'}{M_U} M_U\right), \tag{26}$$

$$= \bar{k}_{A \to U} K_0 \left(M_A \cdot 1\,\text{atm} - \frac{m_A}{W_U K_0} B_U(M_U, \tilde{Q}_U, T_U) M_U\right). \tag{27}$$

Here, M_U' represents the mass of $H_2CO_3^*$ in the upper ocean layer. The factor $1\,\text{atm}$ is introduced for unit consistency and if M_A and M_U are expressed in PgC, then the flux will be in PgC yr^{-1}. We have defined $\bar{k}_{A \to U} = \frac{A_O \rho k}{m_A}$. We would recover the equation of SURFERv2.0 with $k_{A \to U} = \bar{k}_{A \to U} K_0$, but K_0 now depends on temperature. There are two advantages of proceeding as we did here compared to SURFER v2.0. First the coefficient $\bar{k}_{A \to U}$ is a function of well-identifed physical

quantities. Second, we have not used the equilibrium condition for $F_{A \to U}(t_{PI})$ for the derivation of our expression, meaning that we can use it to constrain other quantities. Indeed, once $\bar{k}_{A \to U}$ and M_A are set, the equilibrium condition $F_{A \to U}(t_{PI}) = -(F_{CaCO_3,0} + F_{CaSiO_3,0})$ will determine M'_U (see section 2.4.2).

The term B_U is a factor tracking the ocean's buffer capacity. In SURFER v2.0, it was a function of M_U only. Now, the buffer
195   factor also depends on the variable alkalinity ($\tilde{Q}_U$) and on temperature through the dissociation constants:

$$B_U \left(M_U, \tilde{Q}_U, T_U \right) \equiv \frac{M'_U}{M_U} = \frac{[H_2CO_3^*]_U}{DIC_U} = \left(1 + \frac{K_1}{[H^+]_U} + \frac{K_1 K_2}{[H^+]_U^2} \right)^{-1}. \tag{28}$$

To obtain this equation, we have used equations 17 and 18 to write DIC (eq 11) in terms of $[H_2CO_3^*]_U$ and $[H^+]$. In SURFER v2.0, we could compute analytically $[H^+]$ and B_U as a function of M_U and $\tilde{Q}_U$. We cannot do that anymore because we use a more complete approximation for alkalinity. We still compute $[H^+]$ as a function of M_U and $\tilde{Q}_U$ (and the dissociation
200   constants), but we have to numerically solve a degree 5 equation in $[H^+]$. Appendix C explains how we proceed.

2.1.5 $F_{U \to I}$, $F_{I \to D}$, $\tilde{F}_{U \to I}$, and $\tilde{F}_{I \to D}$

We now focus on carbon transport within the ocean. The processes and fluxes included in SURFER v3.0 are schematised in Figure 2. Carbon enters the upper ocean layer (U) through CO_2 exchanges with the atmosphere and through the riverine influx of weathering products. CO_2 intake from the atmosphere increases DIC but doesn't change alkalinity (see equations R1-R3).
205   This is why we have a $F_{A \to U}$ DIC flux, but no $\tilde{F}_{A \to U}$ alkalinity flux. The riverine influx of weathering products increases DIC and alkalinity in the same amount (1:1 ratio); see section 2.1.7. We divide the exchange of carbon between the ocean layers into three parts which we briefly explain below: the carbonate pump, the soft-tissue pump, and residual processes. For a comprehensive treatment of these processes, see Sarmiento and Gruber (2006).

In the surface layer, calcifying organisms take up bicarbonate ions to form their calcium carbonate ($CaCO_3$) shells (forward
210   reaction R4).

$$Ca^{2+} + 2HCO_3^- \rightleftharpoons CO_2 + H_2O + CaCO_3. \tag{R4}$$

These organisms eventually die and sink to the bottom ocean. On the way down, some of the $CaCO_3$ is dissolved (reverse reaction R4), resulting in a downward transport of DIC and alkalinity at a 1:2 ratio. This is the carbonate pump. We represent the export of $CaCO_3$ at a depth of 150 m (so from layer U to I) by P^{CaCO_3}. A fraction $\phi_I^{CaCO_3}$ of this export simultaneously
215   dissolves in the intermediate layer (I) and a fraction $\phi_D^{CaCO_3}$ simultaneously dissolves in the deep layer (D), which leaves a fraction $1 - \phi_I^{CaCO_3} - \phi_D^{CaCO_3}$ reaching the sediments . Of that $CaCO_3$ that reaches the bottom of the ocean, some dissolves and some is permanently buried (details on this in section 2.1.6).

In the surface layer, organisms also take up carbon through photosynthesis (primary production, forward reaction R5).

$$106CO_2 + 16NO_3^- + HPO_4^{2-} + 122H_2O + 18H^+ \rightleftharpoons (CH_2O)_{106}(NH_3)_{16}(H_3PO_4) + 138O_2. \tag{R5}$$
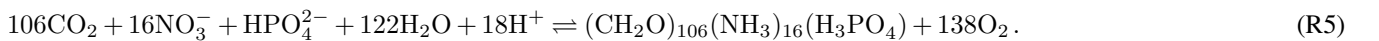
220   The CO_2 is transformed into organic carbon that will eventually sink to the bottom ocean. On the way down, some of the organic carbon is remineralised (reverse reaction R5), resulting in a downward transport of DIC. This is the soft-tissue pump
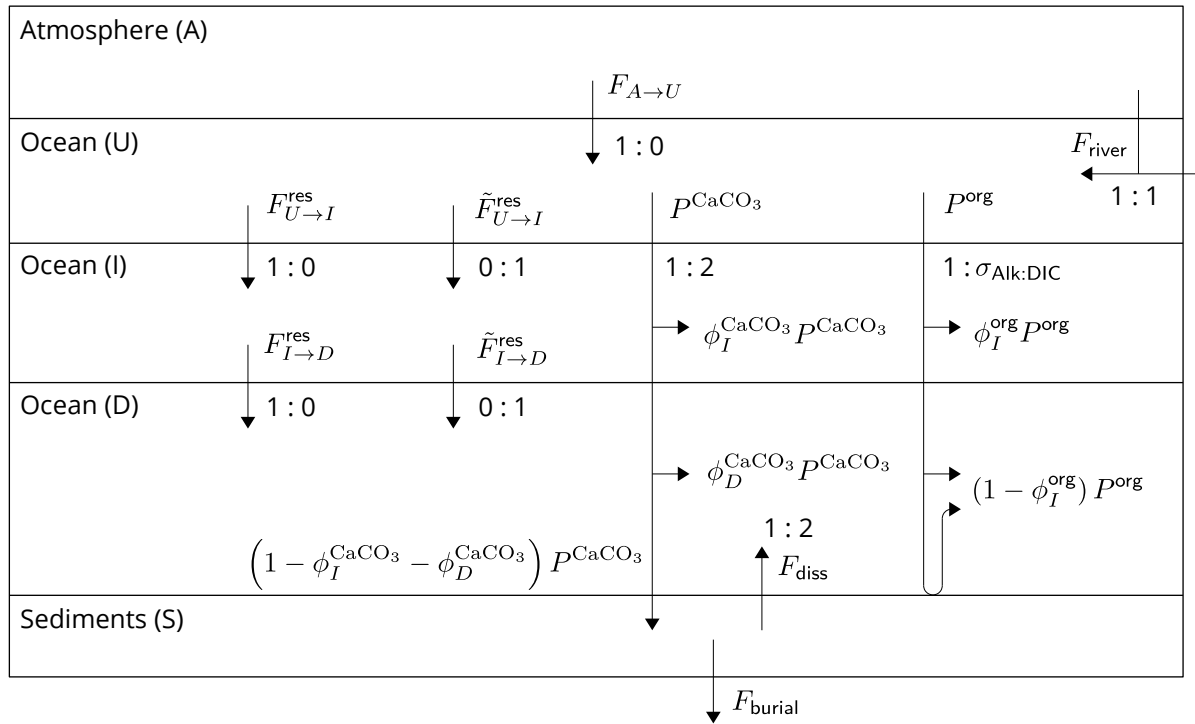
Figure 2. Schematic diagram of the DIC and Alk fluxes in SURFER v3.0. The ratios are ratios of DIC to alkalinity changes, i.e a $a : b$ ratio indicates that for a DIC change of a moles, there is an associated alkalinity change of b moles.

(Volk and Hoffert, 1985). It also acts on alkalinity, mainly through the uptake and release of H^+ needed for the transformation of inorganic nitrate (NO_3^-) into organic nitrogen. Primary production of organic matter increases alkalinity, while remineralisation decreases alkalinity. We represent the ratio of alkalinity to DIC change for primary production and remineralisation with the parameter $\sigma_{\text{Alk:DIC}}$. We represent the export of organic carbon at a depth of 150 m (so from layer U to I) by P^{org}. We consider that all this organic carbon is simultaneously remineralised in the water column, with a fraction ϕ_I^{org} remineralised in the intermediate layer (I), and a fraction $\phi_D^{\text{org}} = 1 - \phi_I^{\text{org}}$ remineralised in the deep layer (D). In reality, some organic carbon accumulates on the sea-floor sediments where a large part is remineralised and only a small amount is permanently buried (Sarmiento and Gruber, 2006). Here, by setting $\phi_D^{\text{org}} = 1 - \phi_I^{\text{org}}$, we neglect this burial and effectively consider that all organic carbon that falls on sediments is remineralised.

Apart from the carbonate and soft-tissue pumps, forming the biological pumps, other processes are responsible for the transport of carbon between the ocean layers. Ocean circulation and mixing will propagate variations in DIC caused by spatial and temporal variations of air-sea gas exchanges. This is termed the gas exchange pump by Sarmiento and Gruber (2006). For example, a component of the gas exchange pump is the solubility pump (Volk and Hoffert, 1985): cold waters have a higher solubility and are thus enriched in CO_2, they are also denser and will sink in the high latitudes, resulting in a downward

transport of DIC. Besides, upwelling is responsible for an upward transport of DIC and alkalinity, necessary to counteract the carbonate and soft-tissue pumps (Goosse, 2015). We gather all the processes related to ocean circulation and mixing in the residual terms $F_{U \to I}^{res}$ and $F_{I \to D}^{res}$, $\tilde{F}_{U \to I}^{res}$ and $\tilde{F}_{I \to D}^{res}$. We consider the residual fluxes of DIC and alkalinity to be independent because some processes such as the solubility pump only act on DIC.

240   Based on the above considerations, the masses of dissolved inorganic carbon and the mass of carbon in the sediments evolve according to the following equations:

$$\frac{dM_U}{dt} = F_{A \to U} - P^{CaCO_3} - P^{org} - F_{U \to I}^{res} + F_{river} , \tag{29}$$

$$\frac{dM_I}{dt} = \phi_I^{CaCO_3} P^{CaCO_3} + \phi_I^{org} P^{org} + F_{U \to I}^{res} - F_{I \to D}^{res} , \tag{30}$$

$$\frac{dM_D}{dt} = \phi_D^{CaCO_3} P^{CaCO_3} + \left(1 - \phi_I^{org}\right) P^{org} + F_{I \to D}^{res} + F_{diss} , \tag{31}$$

$$\frac{dM_S}{dt} = (1 - \phi_I^{CaCO_3} - \phi_D^{CaCO_3}) P^{CaCO_3} - F_{diss} - F_{burial} . \tag{32}$$

We recover equations 1-10 by setting

$$F_{U \to I} = F_{U \to I}^{CaCO_3} + F_{U \to I}^{org} + F_{U \to I}^{res} , \tag{33}$$

$$F_{I \to D} = F_{I \to D}^{CaCO_3} + F_{I \to D}^{org} + F_{I \to D}^{res} , \tag{34}$$

$$F_{acc} = (1 - \phi_I^{CaCO_3} - \phi_D^{CaCO_3}) P^{CaCO_3} - F_{diss} , \tag{35}$$

with the fluxes associated to the carbonate pump defined as

$$F_{U \to I}^{CaCO_3} = P^{CaCO_3} , \tag{36}$$

$$F_{I \to D}^{CaCO_3} = (1 - \phi_I^{CaCO_3}) P^{CaCO_3} , \tag{37}$$

and the fluxes associated to the soft-tissue pump defined as

$$F_{U \to I}^{org} = P^{org} , \tag{38}$$

$$F_{I \to D}^{org} = (1 - \phi_I^{org}) P^{org} . \tag{39}$$

Consequently, for the carbonate alkalinity fluxes, we have

$$\tilde{F}_{U \to I} = 2 \times F_{U \to I}^{CaCO_3} + \sigma_{Alk:DIC} \times F_{U \to I}^{org} + \tilde{F}_{U \to I}^{res} , \tag{40}$$

$$\tilde{F}_{I \to D} = 2 \times F_{I \to D}^{CaCO_3} + \sigma_{Alk:DIC} \times F_{I \to D}^{org} + \tilde{F}_{I \to D}^{res} , \tag{41}$$

$$\tilde{F}_{acc} = 2 \times F_{acc} . \tag{42}$$

260   In the experiments presented here (sections 3 and 4), we keep P^{CaCO_3}, $\phi_I^{CaCO_3}$, $\phi_D^{CaCO_3}$, P^{org}, and ϕ_I^{org} constant. This is an idealisation. Production and export of $CaCO_3$ and organic matter are biological processes and, in reality, depend on the temperature, pH, salinity, nutrient concentration and other properties of the ocean. For example, changes in primary production

(and thus export of organic matter) may have contributed to the CO_2 changes during the glacial-interglacial cycles (Kohfeld and Ridgwell (2009)). In the future, changes in the biological pumps are also possible and might lead to additional feedbacks in the carbon cycle (Henson et al., 2022; Planchat et al., 2023).

For the residual exchange terms, we adopt a linear formalism with exchanges coefficients, similarly as in SURFER v2.0:

$$F_{U \to I}^{res} = k_{U \to I} M_U - k_{I \to U} M_I \,, \tag{43}$$

$$F_{I \to D}^{res} = k_{I \to D} M_I - k_{D \to I} M_D \,, \tag{44}$$

$$\tilde{F}_{U \to I}^{res} = \tilde{k}_{U \to I} \tilde{Q}_U - \tilde{k}_{I \to U} \tilde{Q}_I \,, \tag{45}$$

$$\tilde{F}_{I \to D}^{res} = \tilde{k}_{I \to D} \tilde{Q}_I - \tilde{k}_{D \to I} \tilde{Q}_D \,. \tag{46}$$

2.1.6 F_{acc}, $\tilde{F}_{acc}$, and F_{burial}

The $CaCO_3$ raining on the ocean floor either accumulates and gets buried in sediments, or dissolves, depending on the saturation state of the ocean waters with respect to CO_3^{2-} (Archer et al., 1998; Zeebe and Westbroek, 2003). Typically, the upper ocean is supersaturated in CO_3^{2-} while the deeper ocean is under-saturated, mainly due to the pressure dependence of $CaCO_3$ solubility (Sarmiento and Gruber, 2006). This means that most of the accumulation in sediments will happen in a region above where most of the dissolution happens. A transition zone separates the accumulation and dissolution regions. The top boundary of the transition zone is the lysocline, defined as the depth where the calcium carbonate content of sediments starts to decrease sharply, or in other words, the depth below which the rate of dissolution of $CaCO_3$ starts to increase significantly. The bottom boundary of the transition zone is called the carbonate (or calcite) compensation depth (CCD) and is the depth at which the rate of $CaCO_3$ dissolution is equal to the rate of supply through the $CaCO_3$ rain. Below this depth, no $CaCO_3$ is preserved in the sediments. The depth of the transition zone varies between places and ocean basins but is generally between 3000 and 5000 m deep (Sarmiento and Gruber, 2006). We may thus safely consider in our model that both dissolution and accumulation happen in the deep ocean layer (D), and that is why we group both processes in a single term, F_{acc} which can be positive or negative, negative values indicating net dissolution.

Estimates indicate that carbonate accumulation in shallow waters may be comparable in magnitude to that occurring in open-ocean deep sediments (Milliman, 1993; Milliman and Droxler, 1996; Vecsei, 2004). However, shallow waters are characterised by significantly higher sedimentation rates, necessitating distinct models or parameterisations (Ridgwell and Hargreaves, 2007). Moreover, factors such as carbonate fixation by corals and algae must also be taken into account. Given the significant uncertainty surrounding these processes and the lack of reliable data to quantify them, we excluded them from our model. This approach is equivalent to assuming that $CaCO_3$ accumulation on shelves and the weathering flux required to balance it remain constant throughout the simulations (Archer et al., 1998; Ridgwell and Hargreaves, 2007), despite potential influences from human activities (Andersson and Mackenzie, 2004).

In the open-ocean deep sediments, the local dissolution rate depends on the concentration of $CaCO_3$ in the sediments and the saturation state of pore water around the sediments with respect to carbonate (Sarmiento and Gruber, 2006). We thus assume that the globally integrated dissolution flux is a function of two variables only: the deep ocean mean concentration of CO_3^{2-},

and the total mass of erodible $CaCO_3$ sediments. We use the following parametrisation

$$F_{\text{diss}} = \begin{cases} (1 - \phi_{\text{I}}^{CaCO_3} - \phi_{\text{D}}^{CaCO_3})P^{CaCO_3} & \text{if } M_{\text{S}} = 0 \text{ and } D > (1 - \phi_{\text{I}}^{CaCO_3} - \phi_{\text{D}}^{CaCO_3})P^{CaCO_3}, \\ D & \text{otherwise}, \end{cases} \quad (47)$$

with

$$D = F_{\text{diss},0} + \alpha_{\text{diss}}\left([CO_3^{2-}]_{\text{D}} - [CO_3^{2-}]_{\text{D}}(t_{\text{PI}})\right) + \beta_{\text{diss}}\left(M_{\text{S}} - M_{\text{S}}(t_{\text{PI}})\right)$$
$$+ \gamma_{\text{diss}}\left([CO_3^{2-}]_{\text{D}} - [CO_3^{2-}]_{\text{D}}(t_{\text{PI}})\right)\left(M_{\text{S}} - M_{\text{S}}(t_{\text{PI}})\right). \quad (48)$$
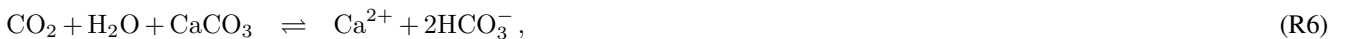
The first case in equation 47 indicates that if the erodible sediments reservoir is empty, the dissolution flux can't exceed the $CaCO_3$ rain flux, regardless of the saturation state of deep waters. The accumulation fluxes of DIC and alkalinity, F_{acc} and $\tilde{F}_{\text{acc}}$, are then given by equations 35 and 42. A similar parametrisation is proposed and tested in Archer et al. (1998), but they use the CO_3^{2-} concentration at a particular point in the deep pacific and the mass of $CaCO_3$ in the bioturbated layer of the sediments as their two variables, instead of the mean deep ocean CO_3^{2-} and the mass of erodible $CaCO_3$. They show that the parametrised version of their model is comparable to the non-parametrised one, except for a dissolution spike in the first 1000-2000 years following the fossil fuel emissions and invasion in the ocean. We choose the coefficient of our parametrisation based on theirs. Details can be found in section 2.4.1.

In the sediments, the bioturbated layer is the layer where sediments are mixed by biological activity (bioturbation). Dissolution only occurs in the top few centimetres near the sediment-ocean interface but can effectively reach deeper because of bioturbation (Sarmiento and Gruber, 2006). If the dissolution rate is greater than the rain rate of $CaCO_3$ on the sea floor, the sediments will lose $CaCO_3$ until the bioturbated layer becomes saturated with non-erodible material. At this point, dissolution stops and deeper carbonates are isolated from the carbon cycle. This explains why the effective reservoir of sediment carbonates to be accounted for here (M_{S}), has a limited size, which is estimated to be around 1600 PgC as of today (Archer et al., 1998). The erodible depth is defined as the lower boundary of the erodible sediments inventory (Archer et al., 1998). By definition, $CaCO_3$ sediments that move below the erodible depth will never be dissolved and we say that they are buried. Locally, the burial rate depends on the rain rate of non-erodible material and the concentration of $CaCO_3$ in sediments at the erodible depth. We assume that the former is constant and that the total burial flux only depends on the total mass of erodible $CaCO_3$. We use the following linear parametrisation

$$F_{\text{burial}} = \alpha_{\text{burial}}M_{\text{S}}. \quad (49)$$

2.1.7 V, $F_{\text{weathering}}$, $F_{\text{river influx}}$, $\tilde{F}_{\text{river influx}}$

Continental weathering of carbonate and silicate rocks can absorb CO_2 out of the atmosphere through the following reactions (Berner et al., 1983; Walker et al., 1981) :

$$CO_2 + H_2O + CaCO_3 \quad \rightleftharpoons \quad Ca^{2+} + 2HCO_3^-, \quad (R6)$$
$$2CO_2 + H_2O + CaSiO_3 \quad \rightleftharpoons \quad Ca^{2+} + 2HCO_3^- + SiO_2. \quad (R7)$$

13

Let us consider F_{CaCO_3} and F_{CaSiO_3} the fluxes of Ca^{2+} produced by these two processes. For carbonate weathering (equation R6), the production of one mole of Ca^{2+} consumes one mole of carbon (CO_2) from the atmosphere and produces two moles of DIC and alkalinity that are transported by the rivers to the ocean. For the silicate weathering (equation R7), the production of one mole of Ca^{2+} consumes two moles of carbon (CO_2) from the atmosphere and produces two moles of DIC and alkalinity that are transported by the rivers to the ocean. Hence, we set

$$F_{\text{weathering}} = F_{CaCO_3} + 2F_{CaSiO_3} \tag{50}$$

$$F_{\text{river influx}} = 2F_{CaCO_3} + 2F_{CaSiO_3} \tag{51}$$

$$F_{\text{river influx}}^{alk} = 2F_{CaCO_3} + 2F_{CaSiO_3} \tag{52}$$

Like with alkalinity, we use $\mathrm{PgC\,yr^{-1}}$ for F_{CaCO_3} and F_{CaSiO_3}, even though they are defined as fluxes of Ca^{2+}. To go from $\mathrm{Tmol\,yr^{-1}}$ to $\mathrm{PgC\,yr^{-1}}$, one just has to divide by the molar mass of carbon $12 \cdot 10^{-3}\,\mathrm{mol\,kg^{-1}}$.

For every two moles of DIC produced by carbonate weathering, one mole of carbon is taken from the atmosphere reservoir and one mole of carbon comes from carbonate rocks on land, which are not explicitly described as a reservoir in our model. This extra mole is thus treated as an external source of carbon, like volcanism. The carbon entering the ocean from weathering fluxes will eventually precipitate back as $CaCO_3$ in the sediments, which releases CO_2. Thus, the net effect of carbonate weathering is to transfer $CaCO_3$ from rocks on land to sediments in the ocean, but with no long-term net effect on the atmospheric CO_2. On the other hand, since silicate weathering consumes one more mole of CO_2 from the atmosphere for the same Ca^{2+} flux, its net effect is to remove carbon from the atmosphere. At equilibrium, this net removal is compensated by volcanic outgassing.

The F_{CaCO_3} and F_{CaSiO_3} fluxes aren't constant and depend on many factors (for a review, see Kump et al., 2000). For example, temperature affects the rates of reactions R6 and R7, water run-off on land influences how much under-saturated water will come in contact with rocks for weathering, and vegetation may affect the acidity of soils and thus the rates of dissolution. Colbourn et al. (2013) provide parametrisations of all these processes for the model of terrestrial rock weathering RockGEM, which was included in the GENIE Earth system modelling framework. They showed that the temperature feedback was the dominant factor, and we choose to consider this one only, especially given that SURFER lacks a representation of the hydrological cycle. Following their parametrisation, we set

$$F_{CaCO_3} = F_{CaCO_3,0}(1 + k_{Ca}\delta T_U), \tag{53}$$

$$F_{CaSiO_3} = F_{CaSiO_3,0}e^{k_T \delta T_U}, \tag{54}$$

where k_{Ca} and k_T are constants and δT_U is the temperature anomaly of the upper ocean (and atmosphere) modeled by SURFER. This is also the parametrisation used by Lord et al. (2016) in their cGENIE simulations, which we will use as a basis for comparison with SURFER (see section 3.4).

2.1.8 Methane

The evolution of the methane concentration in the atmosphere is mainly controlled by 3 processes: natural and anthropogenic emissions increase the CH_4 concentration whereas oxidation into CO_2 decreases it (Saunois et al., 2020).

Anthropogenic emissions can be divided in two sources, fossil emissions ($E_{\text{fossil}}^{\text{CH}_4}$) and land-use emissions ($E_{\text{land-use}}^{\text{CH}_4}$). Fossil emissions come from the industry sector and the use and exploitation of fossil fuels. Land-use emissions result from agriculture (rice production, cattle, ...), agricultural waste burning, and burning of biomass such as forests, grasslands and peat. Natural emissions ($E_{\text{natural}}^{\text{CH}_4}$) mainly come the from anaerobic decomposition of organic matter in wetlands, but also from freshwater systems, termites, and geological sources such as volcanoes, permafrost and methane hydrates. For a detailed treatment of the different methane emissions see Saunois et al. (2020). The rate of natural emissions may depend on temperature, and if they increase upon global warming, this could lead to positive feedbacks and eventually tipping points (Nisbet et al., 2023; Fewster et al., 2022; Archer et al., 2009). For simplicity, we assume constant natural emissions. To ensure the conservation of carbon, land-use CH_4 emissions are taken from the land reservoir, while natural CH_4 emissions are taken directly from the CO_2 atmospheric reservoir of carbon. The reason for this difference is explained in the next section.

Oxidation of methane ($F_{\text{CH}_4,\text{ox}}$, equation R8) is the main sink of methane out of the atmosphere and releases CO_2:

$$CH_4 + 2O_2 \rightarrow CO_2 + 2H_2O \,. \tag{R8}$$

We describe this a simple decay process :

$$F_{\text{CH}_4,\text{ox}} = -\frac{M_{\text{A}}^{\text{CH}_4}}{\tau_{\text{CH}_4}} \,, \tag{55}$$

where τ_{CH_4} is the atmospheric CH_4 lifetime. In principle, it may vary depending on temperature and on the availability of the hydroxyl radical OH, which is necessary for the intermediate steps of reaction R8, and which itself depends on the concentrations of CH_4, N_2O, CO and other trace gases (Skeie et al., 2023). However, for simplicity, we choose to keep τ_{CH_4} constant and set its value to 9.5 yr. We add the product of oxidation to M_{A}.

2.1.9 Land reservoir and land-use emissions

In SURFER v3.0, we distinguish greenhouse gas emissions caused by fossil fuel use from those caused by land use. While fossil CO_2 and CH_4 emissions are directly added to the atmosphere, land-use CO_2 and CH_4 emissions ($E_{\text{land-use}}^{\text{CO}_2}$ and $E_{\text{land-use}}^{\text{CH}_4}$) must be taken from the land reservoir (eq 3). In SURFER v2.0, based on the outputs of the ZECMIP experiments (Jones et al., 2019; MacDougall et al., 2020), we parametrised the carbon flux from the land to the atmosphere in the following way

$$F_{\text{A}\to\text{L}} = k_{\text{A}\to\text{L}} \left(\beta_{\text{L}} M_{\text{A}(t_{\text{PI}})} \left(1 - \frac{M_{\text{A}}(t_{\text{PI}})}{M_{\text{A}}} \right) - (M_{\text{L}} - M_{\text{L}}(t_{\text{PI}})) \right). \tag{56}$$

This is equivalent to saying that M_{L} relaxes to an equilibrium mass $M_{\text{L}}^{\text{eq}}(M_{\text{A}})$ equal to

$$M_{\text{L}}^{\text{eq}}(M_{\text{A}}) = \beta_{\text{L}} M_{\text{A}}(t_{\text{PI}}) \left(1 - \frac{M_{\text{A}}(t_{\text{PI}})}{M_{\text{A}}} \right) + M_{\text{L}}(t_{\text{PI}}), \tag{57}$$

with a timescale $1/k_{\text{A}\to\text{L}}$.

Now suppose that we have a certain amount of land-use emissions; we transfer some carbon out of the land reservoir into the atmosphere reservoir, and let the model evolve without changing anything else. Then the $F_{\text{A}\to\text{L}}$ flux, as it is, will increase

and land will absorb the carbon lost until initial equilibrium is reached again. Physically, this means that the forest that was replaced by grassland or crop fields has grown back to its original size. In the real world, this may happen, but if the land is managed (e.g. for agriculture), the forest does not regrow. To take this into account, we subtract the cumulative CO_2 land-use emissions from the equilibrium mass to which M_L relaxes

$$M_L^{eq}(M_A, t) = \beta_L M_{A(t_{PI})}\left(1 - \frac{M_A(t_{PI})}{M_A}\right) + M_L(t_{PI}) - \int_{t_0}^{t} E_{\text{land-use}}^{CO_2}(t)\,. \tag{58}$$

This is the same procedure as in the model from Lenton (2000), except that they subtract only a fraction of the cumulative land-use emissions, allowing for some forest regrowth. Here we subtract all land-use emissions because, in principle, the negative emissions coming from forest regrowth should already be accounted for in the net reported land-use emissions (IPCC, 2021a, p.688). We can rewrite the new $F_{A \to L}$ flux as

$$F_{A \to L} = k_{A \to L}\left(\beta_L M_{A(t_{PI})}\left(1 - \frac{M_A(t_{PI})}{M_A}\right) - (M_L - M_{L^*})\right)\,, \tag{59}$$

where M_L^* is a new model variable, the evolution of which is described by

$$\frac{dM_L^*}{dt} = -E_{\text{land-use}}^{CO_2}(t)\,, \tag{60}$$

with $M_L^*(t_{PI}) = M_L(t_{PI})$.

We haven't included methane land-use emissions in equations 58-60. This means that the carbon mass in CH_4 form taken from the land reservoir is reabsorbed by land once methane is oxidized back to CO_2. In other words, methane land-use emissions do not cause a net addition of CO_2 in the atmosphere through oxidation. This makes sense if you consider methane emissions coming from the anaerobic decomposition of organic matter in rice cultures or cattle stomachs. Indeed, the decomposed organic matter was formed not too long before by absorbing CO_2 from the atmosphere through photosynthesis, so when the methane oxidises into CO_2, it closes the loop and there is no net effect on atmospheric CO_2.

The same reasoning applies to most natural emissions of methane which arise from wetlands: they do not cause a net increase of atmospheric CO_2 concentrations. In principle, these natural methane emissions should be subtracted from the land carbon reservoir, as anthropogenic land-use emissions, and there should be a non-zero atmosphere-to-land equilibrium flux that compensates the CO_2 created from oxidation. However, this is impossible with our parametrisation of the atmosphere-to-land flux, which is zero at preindustrial times by construction. To avoid introducing yet another parameterisation or a more detailed representation of the carbon on land and to maintain carbon conservation, we merely subtract the natural emissions directly from the CO_2 mass of carbon in the atmosphere. This approach is justified by our assumption that the natural methane production-oxidation cycle is in equilibrium.

Natural CH_4 emissions coming from geological processes such as volcanism or natural gas leaks would have a net impact on CO_2 levels but they are negligible compared to emissions coming from wetlands (Saunois et al., 2020). Natural CH_4 emissions coming from permafrost would also have a lasting effect on CO_2 concentrations because the organic matter from which they originate was formed thousands of years before. Accounting for emissions from permafrost would require yet another parametrisation, and we rather neglected them in SURFER v3.0.

2.2 Climate component

The equations for the climate component are essentially the same as in SURFER v2.0, with the addition of an oceanic box and the radiative forcing due to methane. The atmosphere is considered to be in thermal equilibrium with the surface ocean layer (U). The evolutions of temperature anomalies for the three oceanic layers are dictated by

$$c_{vol} h_U \frac{d\delta T_U}{dt} = F\left(M_A, M_A^{CH_4}, I\right) - \beta \delta T_U - \gamma_{U \to I} \left(\delta T_U - \delta T_I\right), \tag{61}$$

$$c_{vol} h_I \frac{d\delta T_I}{dt} = \gamma_{U \to I} \left(\delta T_U - \delta T_I\right) - \gamma_{I \to D} \left(\delta T_I - \delta T_D\right), \tag{62}$$

$$c_{vol} h_D \frac{d\delta T_D}{dt} = \gamma_{I \to D} \left(\delta T_I - \delta T_D\right), \tag{63}$$

where $F\left(M_A, M_A^{CH_4}, I\right)$ is the anthropogenic radiative forcing. Its expression is given by

$$F\left(M_A, M_A^{CH_4}, I\right) = F_{2\times} \log_2 \left(\frac{M_A}{M_A(t_{PI})}\right) + \alpha_{CH_4} \sqrt{M_A^{CH_4} - M_A^{CH_4}(t_{PI})} - \alpha_{SO_2} \exp\left(-(\beta_{SO_2}/I)^{\gamma^{SO_2}}\right). \tag{64}$$

The first two terms describe the contribution of CO_2 and methane to an increased greenhouse effect. The third term corresponds to solar radiation modification in the form of SO_2 injections (Martínez Montero et al., 2022).

2.3 Sea level rise sub-model

Sea level rise is estimated as the sum of four contributions: thermal expansion, and melt from the mountain glaciers, the Greenland ice sheet, and the Antarctic ice sheet:

$$S_{tot} = S_{th} + S_{gl} + S_{GIS} + S_{AIS}. \tag{65}$$

Compared to SURFER v2.0, we only change the parametrisation of thermal expansion, where we need to add a term to take into account the new intermediate layer.

$$S_{th} = \alpha_U h_U \delta T_U + \alpha_I h_I \delta T_I + \alpha_D h_D \delta T_D. \tag{66}$$

Here α_i is the thermal expansion coefficient corresponding to layer $i \in \{U, I, D\}$. The other contributions are the same as in Martínez Montero et al. (2022). We recall them here, and more details are provided in the original publication.

The evolution of the sea-level rise contribution from glaciers is given by the equation

$$\frac{dS_{gl}}{dt} = \frac{1}{\tau_{gl}} \left(S_{gleq}\left(\delta T_U\right) - S_{gl}\right), \tag{67}$$

with

$$S_{gleq}\left(\delta T_U\right) = S_{gl\,pot} \tanh\left(\frac{\delta T_U}{\zeta}\right). \tag{68}$$

Here τ_{gl} is a relaxation timescale, $S_{gl\,pot}$ is the potential sea level rise due to mountain glaciers and ζ is a sensitivity coefficient.

17

The contributions from Greenland and Antarctica are given by

$$S_{\text{GIS}} = S_{\text{GIS}}\left(1 - V_{\text{GIS}}(t)\right), \quad S_{\text{AIS}} = S_{\text{AIS}}\left(1 - V_{\text{AIS}}(t)\right), \tag{69}$$

where S_{GIS} and S_{AIS} are the sea-level rise potential of Greenland's and Antarctic ice sheet and V_{GIS}, V_{AIS} are the volume fractions of the ice sheets with respect to their preindustrial volume. The evolution of ice sheets volumes are described with the equation

$$\frac{\mathrm{d}V}{\mathrm{d}t} = \mu\left(V, \delta T_{\text{U}}\right) \underbrace{\left(-V^3 + a_2 V^2 + a_1 V + c_1 \delta T_{\text{U}} + c_0\right)}_{H}, \tag{70}$$

with

$$\mu\left(V, \delta T_{\text{U}}\right) = \begin{cases} 1/\tau & \text{if } H > 0 \text{ or } (H < 0 \text{ and } V > 0), \\ 0 & \text{if } H < 0 \text{ and } V = 0, \end{cases} \tag{71}$$

and

$$\tau = \tau_- + \frac{\tau_+ - \tau_-}{2}\left(1 + \tanh\left(\frac{H}{k_\tau}\right)\right). \tag{72}$$

The time scales τ_+ and τ_- are associated with the asymmetric processes of freezing and melting. The first case in equation 71 was separated in two cases in SURFER v2.0, depending on the sign of H. In SURFER v3.0, we introduce a smooth transition between τ_+ and τ_- when H changes sign. This formulation effectively prevents small fluctuations around the equilibrium having different timescales (when H is close to zero). The parameter k_τ controls the smoothness of the transition, SURFER v2.0 being recovered with $k_\tau = \infty$. The constant parameters (a_2, a_1, c_1, c_0) are given in terms of $(T_+, V+), (T_-, V_-))$, which are the bifurcation points of the steady state structure induced by equation 70:

$$a_2 = \frac{3\left(V_- + V_+\right)}{2}, \tag{73}$$

$$a_1 = -3V_- V_+, \tag{74}$$

$$c_1 = -\frac{\left(V_+ - V_-\right)^3}{2\left(T_+ - T_-\right)}, \tag{75}$$

$$c_0 = +\frac{T_+ V_-^2\left(V_- - 3V_+\right) - T_- V_+^2\left(V_+ - 3V_-\right)}{2\left(T_- - T_+\right)}. \tag{76}$$

These relationships allow SURFER to be easily calibrated on the steady-state structure of more complex ice-sheet models.

2.4 Calibration and initial conditions

We calibrate the parameters and initial conditions of the model using known physics, observations, model results, and the hypothesis that the carbon cycle was at equilibrium during preindustrial times. This follows standard practice, even though processes involving longer time scales active at glacial-interglacial time scales are not necessarily in balance (Brovkin et al.,

2016). We assume

$$0 = V - F_{A\to U}(t_{PI}) - F_{A\to L}(t_{PI}) + F_{CH_4,ox}(t_{PI}) - E_{nat}^{CH_4} - F_{weathering}(t_{PI}), \tag{77}$$

$$0 = E_{nat}^{CH_4} - F_{CH_4,ox}(t_{PI}), \tag{78}$$

$$0 = F_{A\to L}(t_{PI}), \tag{79}$$

$$0 = F_{A\to U}(t_{PI}) - F_{U\to I}(t_{PI}) + F_{river}(t_{PI}), \tag{80}$$

$$0 = F_{U\to I}(t_{PI}) - F_{I\to D}(t_{PI}), \tag{81}$$

$$0 = F_{I\to D}(t_{PI}) - F_{acc}(t_{PI}), \tag{82}$$

$$0 = -\tilde{F}_{U\to I}(t_{PI}) + \tilde{F}_{river}(t_{PI}), \tag{83}$$

$$0 = \tilde{F}_{U\to I}(t_{PI}) - \tilde{F}_{I\to D}(t_{PI}), \tag{84}$$

$$0 = \tilde{F}_{I\to D}(t_{PI}) - \tilde{F}_{acc}(t_{PI}), \tag{85}$$

$$0 = F_{acc}(t_{PI}) - F_{burial}(t_{PI}). \tag{86}$$

From equations 83-85 we get that $\tilde{F}_{acc}(t_{PI}) = \tilde{F}_{I\to D}(t_{PI}) = \tilde{F}_{U\to I}(t_{PI}) = \tilde{F}_{river}(t_{PI}) = 2F_{CaCO_3,0} + 2F_{CaSiO_3,0}$. The dissolution/precipitation of $CaCO_3$ produces/consumes moles of DIC and alklanity at a 1:2 ratio (see section 2.1.6), hence we have $F_{acc}(t_{PI}) = \frac{1}{2}\tilde{F}_{acc}(t_{PI}) = F_{CaCO_3,0} + F_{CaSiO_3,0}$. We then get from equations 81,82 and 86 that $F_{U\to I}(t_{PI}) = F_{I\to D}(t_{PI}) = F_{burial}(t_{PI}) = F_{acc}(t_{PI}) = F_{CaCO_3,0} + F_{CaSiO_3,0}$. Equation 80 gives us $F_{A\to L}(t_{PI}) = -(F_{CaCO_3,0} + F_{CaSiO_3,0})$, equation 78 tells us that $E_{nat}^{CH_4} = F_{CH_4,ox}(t_{PI})$, and finally, from equation 77 we find $V = F_{CaSiO_3,0}$. Equation 79 provides no extra information since $F_{A\to L}(t_{PI}) = 0$ by construction. Developing the expressions of the carbon fluxes, we get the following system of equations :

$$V = F_{CaSiO_3,0}, \tag{87}$$

$$E_{nat}^{CH_4} = \frac{M_A^{CH_4}(t_{PI})}{\tau_{CH_4}}, \tag{88}$$

$$0 = 0, \tag{89}$$

$$\bar{k}_{A\to U}K_0\left(M_A(t_{PI}) - \frac{m_A}{W_U K_0}M_U'(t_{PI})\right) = -(F_{CaCO_3,0} + F_{CaSiO_3,0}), \tag{90}$$

$$P^{CaCO_3} + P^{org} + k_{U\to I}M_U(t_{PI}) - k_{I\to U}M_I(t_{PI}) = F_{CaCO_3,0} + F_{CaSiO_3,0}, \tag{91}$$

$$(1 - \phi_I^{CaCO_3})P^{CaCO_3} + (1 - \phi_I^{org})P^{org} + k_{I\to D}M_I(t_{PI}) - k_{D\to I}M_D(t_{PI}) = F_{CaCO_3,0} + F_{CaSiO_3,0}, \tag{92}$$

$$2P^{CaCO_3} + \sigma_{Alk:DIC}P^{org} + \tilde{k}_{U\to I}\tilde{Q}_U(t_{PI}) - \tilde{k}_{I\to U}\tilde{Q}_I(t_{PI}) = 2(F_{CaCO_3,0} + F_{CaSiO_3,0}), \tag{93}$$

$$2(1 - \phi_I^{CaCO_3})P^{CaCO_3} + \sigma_{Alk:DIC}(1 - \phi_I^{org})P^{org} + \tilde{k}_{I\to D}\tilde{Q}_I(t_{PI}) - \tilde{k}_{D\to I}\tilde{Q}_D(t_{PI}) = 2(F_{CaCO_3,0} + F_{CaSiO_3,0}), \tag{94}$$

$$(1 - \phi_I^{CaCO_3} - \phi_D^{CaCO_3})P^{CaCO_3} - F_{diss,0} = F_{CaCO_3,0} + F_{CaSiO_3,0}, \tag{95}$$

$$\alpha_{burial}M_S(t_{PI}) = F_{CaCO_3,0} + F_{CaSiO_3,0}. \tag{96}$$

The equilibrium hypothesis effectively provides us with constraints linking some parameters and initial conditions. In section 2.4.1 we discuss the choice and calibration of the model parameters. A sensitivity analysis for most parameters is presented in appendix D. In section 2.4.2, we provide a set of initial conditions for the model.

2.4.1 Parameters

Carbon cycle component

The parameters that control the CO_2 uptake by vegetation (β_L, $k_{A\to L}$) and the CO_2 uptake by the ocean on short time scales ($k_{U\to I}$ and $\tilde{k}_{U\to I}$) are tuned to reproduce historical observations of CO_2 concentrations (Figure 4), historical estimations of land and ocean sinks (Figure 6) as well as historical and SSP runs of CMIP6 (Figures 7 and 8). The parameters $k_{I\to D}$ and $\tilde{k}_{I\to D}$, which control the ocean carbon uptake on multi-centennial to multi-millennial time scales, are chosen to produce a reasonable fit with the 1 Myr runs of cGENIE (see section 3.4). Overall, the calibration to other models is performed qualitatively, without optimising well-defined metrics.

The parameter $\bar{k}_{A\to U}$ is defined as $\bar{k}_{A\to U} = A_O\rho k/m_A$. With ocean area $A_O = 361 \times 10^{12}$ m^2, mean sea water density $\rho = 1026$ kg m^{-3}, gas transfer velocity $20\,\mathrm{cm\,h^{-1}} = 0.2 \cdot 365 \cdot 24\,\mathrm{m\,yr^{-1}}$ (Yang et al., 2022), and number of moles in the atmosphere $m_A = 1.727 \times 10^{20}$ mol, we obtain $\bar{k}_{A\to U} = 4.7$ kg(mol yr)$^{-1}$. The parameter β_L, which controls the amount of CO_2 uptake by vegetation (see eq 59), is set to 1.7. This is the same value as for SURFER v2.0, which was calibrated on the outputs of the ZECMIP experiments (Jones et al., 2019). The parameter $k_{A\to L}$ is set to 0.044, which is an increase by a factor 1.75 compared to SURFER v2.0. This is done to have a better match with historical CO_2 concentrations.

The parameters that dictate the DIC and alkalinity exchanges between the ocean layers are physically determined by the oceanic circulation, hence we expect them to be similar ($k_{i\to j} \approx \tilde{k}_{i\to j}$ for $i, j \in \{U,I,D\}$), but we do not require them to be equal because some processes such as the solubility pump can impact DIC and alkalinity independently. Yet, for simplicity, we set both $k_{U\to I}$ and $\tilde{k}_{U\to I}$ to 0.13 yr^{-1}, and both $k_{I\to D}$ and $\tilde{k}_{I\to D}$ to 0.009 yr^{-1}. Then, $k_{I\to U}$ and $\tilde{k}_{I\to U}$, $k_{D\to I}$ and $\tilde{k}_{D\to I}$ are computed from equations 91-94. We have

$$k_{I\to U} = \left(P^{\mathrm{CaCO_3}} + P^{\mathrm{org}} - (F_{\mathrm{CaCO_3},0} + F_{\mathrm{CaSiO_3},0}) + k_{U\to I}M_U(t_{\mathrm{PI}})\right)\frac{1}{M_I(t_{\mathrm{PI}})}, \tag{97}$$

$$k_{D\to I} = \left((1-\phi_I^{\mathrm{CaCO_3}})P^{\mathrm{CaCO_3}} + (1-\phi_I^{\mathrm{org}})P^{\mathrm{org}} - (F_{\mathrm{CaCO_3},0} + F_{\mathrm{CaSiO_3},0}) + k_{I\to D}M_I(t_{\mathrm{PI}})\right)\frac{1}{M_D(t_{\mathrm{PI}})}, \tag{98}$$

$$\tilde{k}_{I\to U} = \left(2P^{\mathrm{CaCO_3}} + \sigma_{\mathrm{Alk:DIC}}P^{\mathrm{org}} - 2(F_{\mathrm{CaCO_3},0} + F_{\mathrm{CaSiO_3},0}) + \tilde{k}_{U\to I}\tilde{Q}_U(t_{\mathrm{PI}})\right)\frac{1}{\tilde{Q}_I(t_{\mathrm{PI}})}, \tag{99}$$

$$\tilde{k}_{D\to I} = \left(2(1-\phi_I^{\mathrm{CaCO_3}})P^{\mathrm{CaCO_3}} + \sigma_{\mathrm{Alk:DIC}}(1-\phi_I^{\mathrm{org}})P^{\mathrm{org}} - 2(F_{\mathrm{CaCO_3},0} + F_{\mathrm{CaSiO_3},0}) + \tilde{k}_{I\to D}\tilde{Q}_I(t_{\mathrm{PI}})\right)\frac{1}{\tilde{Q}_D(t_{\mathrm{PI}})}. \tag{100}$$

With the choices for the other parameters described hereafter, we obtain $k_{I\to U} = 0.0383$ yr^{-1}, $\tilde{k}_{I\to U} = 0.0392$ yr^{-1}, $k_{D\to I} = 1.44 \times 10^{-3}$ yr^{-1}, and $\tilde{k}_{D\to I} = 1.43 \times 10^{-3}$ yr^{-1}. Overall, this corresponds to a time scale range of 7.7 - 26.1 yr ($1/k_{U\to I}$ - $1/k_{I\to U}$) for the oceanic carbon exchanges between surface and intermediate layers, and a time scale range of 111.1 - 693.8 yr ($1/k_{I\to D}$ - $1/k_{D\to I}$) for the oceanic carbon exchanges between intermediate and deep layers. This also gives preindustrial DIC fluxes of 175 PgC yr^{-1} for subduction ($k_{U\to I}M_U(t_{\mathrm{PI}})$) and 183 PgC yr^{-1} for obduction ($k_{I\to U}M_I(t_{\mathrm{PI}})$). Although these

20

carbon fluxes are an order of magnitude greater than the fluxes from the biological pumps, they are much less studied, and estimates in the literature are rare. IPCC AR5 gave estimates of $90 \, \mathrm{PgC \, yr^{-1}}$ and $101 \, \mathrm{PgC \, yr^{-1}}$ for subduction and obduction respectively (Stocker et al., 2013), while IPCC AR6 gave estimates of $264 \, \mathrm{PgC \, yr^{-1}}$ and $275 \, \mathrm{PgC \, yr^{-1}}$ (Levy et al., 2013; Canadell et al., 2021).

The $CaCO_3$ export out of the ocean surface has been estimated between 0.6 and $1.8 \, \mathrm{PgC \, yr^{-1}}$ (see supplementary material in Sulpis et al. (2021) and references therein). Sulpis et al. (2021) provide a tighter range of 0.77 to $1.06 \, \mathrm{PgC \, yr^{-1}}$, of which 0.34 to $0.53 \, \mathrm{PgC \, yr^{-1}}$ are dissolved in the water column before reaching the sediments. We set P^{CaCO_3} to $1 \, \mathrm{PgC \, yr^{-1}}$, which is also the value given in Sarmiento and Gruber (2006) for the open-ocean export at a $100 \, \mathrm{m}$ depth. We set $\phi_I^{CaCO_3} = 0.15$ and $\phi_D^{CaCO_3} = 0.39$. This gives us a total of $0.54 \, \mathrm{PgC \, yr^{-1}}$ dissolved in the water column and $0.46 \, \mathrm{PgC \, yr^{-1}}$ that rains on the sediments, which is close to estimates from Sulpis et al. (2021) and Sarmiento and Gruber (2006, see Figure 9.1.1).

Estimates of the export of organic carbon out of the euphotic zone range from 4 to $12 \, \mathrm{PgC \, yr^{-1}}$ (DeVries and Weber (2017), and references therein). The euphotic zone is the uppermost layer of the ocean that receives sunlight and where photosynthesis can happen. Since the remineralisation of organic matter is quite fast in the water column, estimates of carbon export vary greatly depending on the specific definition of the euphotic zone and its depth. Based on a data-assimilated model, DeVries and Weber (2017) give an estimate of $9.1 \pm 0.2 \, \mathrm{PgC \, yr^{-1}}$ for the organic carbon export out of the euphotic zone and an estimate of $6.7 \, \mathrm{PgC \, yr^{-1}}$ for the organic carbon export at $100 \, \mathrm{m}$ depth. In our model, we set the organic carbon export P^{org} at a 150 m depth to $7 \, \mathrm{PgC \, yr^{-1}}$, which corresponds to the estimate given for the open ocean in Sarmiento and Gruber (2006), and we set $\phi_I^{org} = 0.72$. Equation R5 suggests that for a 106-mole decrease in DIC due to organic matter production, alkalinity will increase by 17 moles (the uptake of 18 moles of H^+ increases alkalinity by 18 moles, while the uptake of HPO_4^{2-}, which is one of the minor bases included in the full definition of alkalinity (eq 12), decreases alkalinity by one mole). Here, we follow Sarmiento and Gruber (2006) and set $\sigma_{Alk:DIC}$ to $-16/117$, meaning that for 1 mole uptake of DIC in organic matter production, alkalinity is increased by $16/117 = 0.14$ moles. Setting $\sigma_{Alk:DIC} = -16/117$ instead of $\sigma_{Alk:DIC} = -17/106$ doesn't result in much change, as can be seen from the sensitivity analysis in appendix D.

For our parametrisation of $CaCO_3$ dissolution, we need to calibrate 4 parameters. The value of $F_{diss,0}$ is computed using equilibrium conditions. From equation 95, we obtain

$$F_{diss,0} = (1 - \phi_I^{CaCO_3} - \phi_D^{CaCO_3})P^{CaCO_3} - (F_{CaCO_3,0} + F_{CaSiO_3,0}) \tag{101}$$

With the choice of P^{CaCO_3}, $\phi_I^{CaCO_3}$, $\phi_D^{CaCO_3}$ described above, and the choice for $F_{CaCO_3,0}$, $F_{CaSiO_3,0}$ described below, we get $F_{diss,0} = 0.33 \, \mathrm{PgC \, yr^{-1}}$. The parameters α_{diss}, β_{diss} and γ_{diss} are obtained based on a parametrisation provided in Archer et al. (1998) for accumulation (rain minus dissolution). The values we use are given in Table 2.

We split the total weathering flux evenly between silicate and carbonate weathering ($F_{CaCO_3,0} = F_{CaSiO_3,0}$) and we set them such as to obtain a preindustrial burial flux of $0.13 \, \mathrm{PgC \, yr^{-1}}$. This is the estimate given in Sarmiento and Gruber (2006). For comparison, the IPCC AR6 WG1 gives an estimate of $0.2 \, \mathrm{PgC \, yr^{-1}}$. From equation 89, we have $F_{CaCO_3,0} + F_{CaSiO_3,0} = \alpha_{burial}M_S(t_{PI}) = F_{burial}(t_{PI}) = 0.13 \, \mathrm{PgC \, yr^{-1}}$, which gives us $F_{CaCO_3,0} = F_{CaSiO_3,0} = 0.065 \, \mathrm{PgC \, yr^{-1}}$ or $5.42 \, \mathrm{Tmol \, yr^{-1}}$. This implies preindustrial CO_2 consumption fluxes of $5.42 \, \mathrm{Tmol \, yr^{-1}}$ for carbonate weathering ($F_{CaCO_3,0}$)

and 10.84 Tmol yr^{-1} for silicate weathering ($2 \times F_{CaSiO_3,0}$). These values are relatively low compared to literature estimates of $8.6 - 12.3$ Tmol yr^{-1} and $11.7 - 17.9$ Tmol yr^{-1}, respectively (Colbourn et al., 2015, and references therein). Nevertheless, they are close to the values from Lord et al. (2016), whose 1 Myr cGENIE runs we use as a calibration target for SURFER v3.0. This being said, setting higher preindustrial weathering fluxes, and particularly higher carbonate weathering fluxes, has a minimal impact on simulated atmospheric CO_2 concentrations, as demonstrated in Appendix D.

From these choices, we get $\alpha_{burial} = (F_{CaCO_3,0} + F_{CaSiO_3,0})/M_S(t_{PI}) = 0.13/M_S(t_{PI})$. Volcanic outgassing is set to $V = F_{CaSiO_3,0} = 0.065$ PgC yr^{-1} as per equation 87. The IPCC estimate is 0.1 PgC yr^{-1}. Following Colbourn et al. (2013), we set k_{Ca} to 0.049 K^{-1} and k_T to

$$k_T = \frac{1000 E_a}{R T_0^2}, \tag{102}$$

where R is the gas constant (in J K^{-1}mol^{-1}), T_0 is the global mean preindustrial temperature (in K) and E_a is the activation energy for dissolution (in kJ mol^{-1}). West et al. (2005) provide an estimate for the activation energy: $E_a = 74 \pm 29$ kJ mol^{-1}. With $T_0 = T_U(t_{PI}) = 288.38$ K (as set in section 2.4.2), this gives a range for k_T between 0.065 K^{-1} and 0.149 K^{-1}. We set $k_T = 0.095$ K^{-1}. Together with the other parameter choices, this leads to long-term CO_2 atmospheric which fit well the ones simulated by Lord et al. (2016) with cGENIE (see Section 3.4). We note that more recent work provided updated estimates for the action energy E_a as low as 22 kJ mol^{-1}, which would imply lower values for k_T than the ones we are using (Brantley et al., 2023). On the other hand, using a higher value may help compensate for the absence of a simulated hydrological cycle, which is critical for representing silicate and carbonate weathering fluxes but whose response to anthropogenic emissions is less certain than that of temperature (Kukla et al., 2023; Maher and Chamberlain, 2014).

Natural methane emissions are set to $E_{nat}^{CH_4} = M_A^{CH_4}(t_{PI})/\tau_{CH_4}$. With $M_A^{CH_4}(t_{PI})$ chosen as in section 2.4.2 and $\tau_{CH_4} = 9.5$ yr, we get natural emissions of 0.157 PgC yr^{-1} or 209 TgCH$_4$ yr^{-1}. This is in the range of the top-down estimate of the IPCC (176-243 TgCH$_4$ yr^{-1}) and a bit below the bottom-up estimate range (245-484 TgCH$_4$ yr^{-1}) (Canadell et al., 2021).

Climate component

For the parametrisation of the heat exchange between the ocean layers, we first distinguished $\gamma_{U \to I}$ and $\gamma_{I \to D}$, and ended up setting $\gamma_{U \to I} = \gamma_{I \to D} = 0.8357$ W m^{-2} °C^{-1}. This is the value chosen for the unique γ in SURFER v2.0. This gives us a transient climate response (TCR) of 1.9 °C , well in the likely range of 1.4°C - 2.2°C given by the IPCC (Forster et al., 2021). In section 4 we show that this choice gives a good fit to the estimated heat uptake by the deep ocean in the period 1971-2018.

For the contribution of methane to the radiative forcing F_{CH_4} (in W m^{-2}), we use a common parametrisation (Myhre et al., 1998)

$$F_{CH_4} = 0.036 \sqrt{C_{CH_4} - C_{CH_4}(t_{PI})}, \tag{103}$$

where C_{CH_4} is the methane atmospheric concentration in ppb. We have

$$C_{CH_4} = \frac{M_A^{CH_4}}{\bar{m}_C m_A} 10^{21}, \tag{104}$$

Table 1. Physical parameters and geometry.

Symbol	Comment	Value
m_A	number of moles in the atmosphere	1.727×10^{20} mol
m_O	number of moles in the ocean	7.8×10^{22} mol
$\bar{m}_C$	carbon molar mass	12×10^{-3} kg mol^{-1}
$\bar{m}_w$	water molar mass	18×10^{-3} kg mol^{-1}
c_{vol}	sea water volumetric heat capacity	0.13 W yr m^{-3} $^\circ$C^{-1}
R	gas contant	8.314 J mol^{-1}K^{-1}
h_U	upper layer depth	150 m
h_I	intermediate layer depth	500 m
h_D	deep layer depth	3150 m
W_U	upper layer weight	$h_U \bar{m}_w m_O / (h_U + h_I + h_D)$
W_I	intermediate layer weight	$h_I \bar{m}_w m_O / (h_U + h_I + h_D)$
W_D	deep layer weight	$h_D \bar{m}_w m_O / (h_U + h_I + h_D)$
z_U	upper layer depth mid-depth point	75 m
z_I	intermediate layer mid-depth point	400 m
z_D	deep layer mid-depth point	2225 m

where $M^{\mathrm{CH_4}}$ is expressed in PgC, and thus

$$\alpha_{\mathrm{CH_4}} = 0.036 \sqrt{\frac{10^{21}}{\bar{m}_C m_A}} \,. \tag{105}$$

SLR component

The thermal expansion coefficient (for the density) of a water parcel is defined as $\alpha = \frac{1}{\rho} \frac{\partial \rho}{\partial t}|_{P,S}$, where ρ, P, and S are the density, the pressure and salinity of that water parcel. To obtain the averaged thermal expansion coefficients for each ocean layer α_U, α_I and α_D, we proceed in three steps, as in Williams et al. (2012). First, we use the GLODAPv2.2016b mapped climatology (Lauvset et al., 2016) to compute the thermal expansion coefficient at each ocean point. To do this, we use the International Thermodynamic Equation Of Seawater - 2010 (TEOS-10) and the Python implementation of the GSW Oceanographic toolbox of TEOS-10 (McDougall and Barker, 2011). Second, we average over each horizontal level of the GLODAPv2.2016b climatology to obtain a vertical profile of the thermal expansion coefficient. Third, we average over each of our defined ocean layers, using the areas of each horizontal level as weights for the horizontally averaged values of the thermal expansion coefficient. We obtain $\alpha_U = 2.20 \times 10^{-4}$ K^{-1}, $\alpha_I = 1.61 \times 10^{-4}$ K^{-1} and $\alpha_D = 1.39 \times 10^{-4}$ K^{-1}. This is close to the values used in SURFER v2.0 ($\alpha_U = 2.3 \times 10^{-4}$ K^{-1} and $\alpha_D = 1.3 \times 10^{-4}$ K^{-1}). In section 4, we show that these expansion coefficients give a good fit to the thermosteric sea level rise on multi-millennial time scales as simulated by the Earth

System Model of Intermediate Complexity UVic 2.8. All other parameters of the sea level rise component are as in SURFER v2.0 and are recapped in tables 4 and 5.

2.4.2 Initial conditions

610 As in SURFER v2.0, the initial mass of carbon in atmospheric CO_2, $M_A(t_{PI})$, is set such as to have a preindustrial atmospheric CO_2 concentration of 280 ppm. We have

$$M_A(t_{PI}) = 280 \times 10^{-18} m_A \bar{m}_C = 580.27 \, \text{PgC}. \tag{106}$$

The initial mass of carbon in atmospheric CH_4, $M_A^{CH_4}(t_{PI})$, is set such as to have a preindustrial atmospheric CH_4 concentration of 720 ppb. We have

615 $$M_A^{CH_4}(t_{PI}) = 720 \times 10^{-21} m_A \bar{m}_C = 1.49 \, \text{PgC}. \tag{107}$$

The initial mass of carbon in land soils and vegetation $M_L(t_{PI})$ is set to 2200 PgC, as in SURFER v2.0. Hence, we have $M_L^*(t_{PI}) = M_L(t_{PI}) = 2200 \, \text{PgC}$. The initial mass of carbon in erodible $CaCO_3$ sediments, $M_S(t_{PI})$, is set to 1600 PgC, following Archer et al. (1998).

For each ocean layer, we have 17 quantities (T, S, K_0, K_1, K_2, K_w, K_b, $[H^+]$, $[H_2CO_3^*]$, $[HCO_3^-]$, $[CO_3^{2-}]$, $[OH^-]$,

620 $[H_3BO_3]$, $[H(BO)_4^-]$, DIC, Alk, p_{CO_2}) that are linked by a nonlinear system of 13 equations (equations 11, 13, 17-22, B1, B2-B5 (+B7)). Hence, only $17 - 13 = 4$ of these quantities may be set independently. Equation B7 for the pressure dependence of the dissociation constants isn't counted because it can be combined with equations B2-B5. For each ocean layer, we will set initial temperature, salinity, alkalinity and DIC, except for the surface layer where we set $[H_2CO_3^*]$ instead of DIC. This is because equilibrium conditions give a constraint on the $H_2CO_3^*$ mass (and thus $[H_2CO_3^*]$) in the upper layer. Equation 90 gives

625 us

$$M_U'(t_{PI}) = \frac{W_U K_0}{m_A} M_A(t_{PI}) + \frac{W_U}{\bar{k}_{A \to U} m_A} (F_{CaSiO_3,0} + F_{CaCO_30}). \tag{108}$$

We obtain $M_U'(t_{PI}) = 6.94 \, \text{PgC}$ and $[H_2CO_3^*]_U(t_{PI}) = M_U'(t_{PI})/(W_U \bar{m}_C) \times 10^{18} = 10.43 \, \mu\text{mol kg}^{-1}$. To set the other quantities, we use the GLODAPv2.2016b mapped climatologies (Lauvset et al., 2016), which include climatologies for temperature, salinity, alkalinity, dissolved inorganic carbon, preindustrial dissolved inorganic carbon and pH, among other biogeochemical

630 variables, which were computed based on data gathered between 1972 and 2013. The dissolved inorganic carbon data is normalized to 2002, and the pH is computed based on temperature, alkalinity and the normalised DIC. We compute the global averages of these data fields over our defined ocean layers by the same averaging method as used for computing the thermal expansion coefficients (see section 2.4.1). The values obtained are in table 6.

We set the initial (and constant) salinities S_U, S_I, S_D of our ocean layers to the computed averages from the GLODAP data.

635 The temperatures of the ocean layers are defined as

$$T_i(t) = T_{i,0} + \delta T_i(t) \qquad \text{for } i \in \{U, I, D\}. \tag{109}$$

By definition, the initial conditions for the temperature anomalies δT_i are zero. We set $T_{i,0}$ such that $T_i(t = 2002)$, obtained from experimental runs, is approximately equal to the temperature average computed from the GLODAP data. We set $\tilde{Q}_U(t_{PI})$, $\tilde{Q}_I(t_{PI})$, $\tilde{Q}_D(t_{PI})$, $M_I(t_{PI})$, and $M_D(t_{PI})$ based on the computed averages for DIC and Alk, converted to carbon masses with equations 14 and 15. $M_U(t_{PI})$ is computed the from the fixed $[H_2CO_3^*]_U(t_{PI})$, S_U, $T_{U,0}$, $Alk_U(t_{PI})$. Details for the computation are provided in appendix C. We obtain $M_U(t_{PI}) = 1344.78\,\mathrm{PgC}$, which corresponds to $DIC_U(t_{PI}) = 2022.08\,\mathrm{\mu mol\,kg^{-1}}$. This is only 0.22% off compared to the averaged value for the upper layer obtained from GLODAP. The total dissolved inorganic carbon in the ocean is 37772 PgC, which is close to the 38000 PgC estimate from the IPCC (Canadell et al., 2021).

For the sea level rise components, as in SURFER v2.0, we set $S_{gl}(t_{PI}) = 0$, $V_{GIS}(t_{PI}) = 1$, and $V_{AIS}(t_{PI}) = 1$. All initial conditions a recapped in table 7.

In Figure 3, we compare the horizontally averaged vertical depth profiles of GLODAP to the vertical profiles of SURFER v3.0 for different model quantities. The vertical profiles of SURFER are computed by running the model from 1750 to 2002, forced with historical CH_4 and CO_2 emissions, and starting from the initial conditions described above. We observe that the chosen initial conditions produce a model state in 2002 that matches the GLODAP data.

2.5 Numerics

The model is implemented in Python 3.0. using the library solve_ivp with the integration method LSODA. The LSODA method has an automatic stiffness detection and switches accordingly between an Adams and BDF method (Petzold, 1983). The local error estimates are kept below $atol + rtol \times abs(y)$ where $atol$ and $rtol$ are parameters that control the relative and absolute accuracy and where y is a model variable. By default, we set $atol$ to 10^{-3} for the variables $M_A^{CH_4}$ M_S, δT_U, δT_I, δT_D, S_{gl}, V_{GIS}, V_{AIS}, and we set $atol$ to 10^{-6} for the other variables. The reason for this difference is that the variables in the first group can have small or near zero values, meaning that $atol$ will dominate the local error estimate. If it is too small, the solver takes too many steps and is slow. We set $rtol$ to 10^{-6} for all variables. The code is compiled with Numba and the model runs fast. When forced with CO_2 and CH_4 emissions of a given SSP scenario, runs of 10^3 to 10^6 years take typically around 60 milliseconds on a laptop with processor Intel® Core™ i5-10210U CPU @ 1.60GHz × 8. The run time is not a linear function of simulated time because the LSODA method uses an adaptive time step.

3 Numerical results and comparisons

In this following section, we test SURFER v3.0 and show that it is an adequate representation of the real climate system. We show that it reproduces well-known dynamics of the carbon cycle and we compare it with outputs of other models over a large range of time scales.

3.1 Historical period

We show here that SURFER v3.0 is able to reproduce the measured historical CO_2 and CH_4 concentrations, and the estimated land and ocean carbon sinks. We perform a historical run by starting SURFER in 1750 with the parameters and initial conditions

described in section 2.4. We force the model with fossil and land-use emissions of CO_2 and CH_4. Emissions from other greenhouse gases such as nitrous oxide (N_2O), ozone (O_3), halogenated gases and aerosols are not taken into account. Figures 4 and 5 show the historical CO_2 and CH_4 concentrations as simulated by SURFER v3.0 compared to the measurements from Köhler et al. (2017). SURFER v3.0 is in good agreement with the historical CO_2 observations, with a difference of at most $\sim$6 ppm, which is better than SURFER v2.0. For methane concentrations, SURFERv3.0 is in relatively good agreement with the historical observations, although it doesn't capture well the apparent stabilisation in the 2000s. The cause for this stabilisation is not totally clear (Turner et al., 2019). Main hypothesises include a decline in fossil emissions (Chandra et al., 2024), and a shortening of the lifetime of atmospheric CH_4, due to increasing concentrations of the hydroxyl radical caused by changes in emissions of other gases such as N_2O and carbon monoxide (CO) (Skeie et al., 2023). These processes are not modelled in SURFER v3.0, where the atmospheric lifetime of CH_4 is kept constant.

In Figure 6, we compare the partitioning of CO_2 emissions in the atmosphere, land and ocean reservoirs with the estimates from the Global Carbon Budget (GCB) (Friedlingstein et al., 2022). Fossil and land-use CO_2 emissions used in SURFER v3.0 up to the year 1990 are the estimates provided by the GCB, and and after that, we start using the emission values provided for the SSP scenarios. These are slightly different than the estimates from the GCB (see appendix A), which explains the small mismatch visible in Figure 6. In SURFER, we compute the ocean sink as $S_{ocean} = F_{A \to U} - F_{A \to U}(t_{PI})$, following the definition of Hauck et al. (2020), the land sink as $S_{land} = F_{A \to L} - F_{A \to L}(t_{PI}) = F_{A \to L}$, and the atmospheric growth as $\frac{dM_A}{dt}$. These quantities simulated by SURFER v3.0 for the historical period are very close to the estimates from the GCB. For the years 2000 to 2010, the GCB gives a mean estimate of $2.3 \pm 0.4 \, \mathrm{PgC \, yr^{-1}}$ for the ocean sink, $2.7 \pm 0.5 \, \mathrm{PgC \, yr^{-1}}$ for the land sink, and $4 \pm 0.02 \, \mathrm{PgC \, yr^{-1}}$ of atmospheric growth. Values simulated in SURFER v3.0 are respectively $2.16 \, \mathrm{PgC \, yr^{-1}}$, $3.05 \, \mathrm{PgC \, yr^{-1}}$ and $3.96 \, \mathrm{PgC \, yr^{-1}}$, with only the atmospheric growth being just below the GCB estimated range. The cumulative budgets are also very similar: of the total amount of emissions in the period 1850-2014, the GCB estimates that around $26\pm5\%$ are absorbed by the ocean, $31\pm7\%$ are absorbed by the land and $40\pm1\%$ stay in the atmosphere, while for SURFER v3.0, those numbers are respectively 24%, 37% and 41%. In the GCB, there is a cumulative budget imbalance of 15 PgC for the years 1850-2014, which arises from errors in independent estimates of emissions and sinks, as well as from missing terms in the budget computation. In SURFER v3.0, however, carbon is explicitly conserved and the budget imbalance (B_{im}) only results from the definition of the sinks, which don't capture processes such as methane oxidation or changes in carbonate and silicate weathering fluxes. Indeed, we have

$$B_{im} = E_{fossil}^{CO_2} + E_{land\text{-}use}^{CO_2} - \left(\frac{dM_A}{dt} + S_{ocean} + S_{land} \right) \tag{110}$$

$$= -V + F_{A \to U}(t_{PI}) + F_{weathering} - \left(F_{CH_4,ox} - E_{natural}^{CH_4} \right) \tag{111}$$

$$= (F_{weathering} - F_{weathering}(t_{PI})) - \left(F_{CH_4,ox} - E_{natural}^{CH_4} \right), \tag{112}$$

and the cumulative budget imbalance for the years 1850-2014 is -15 PgC, with a contribution of +1 PgC from increased weathering fluxes and -16 PgC from methane oxidation.

26

3.2 CMIP6 projections

We now compare SURFER v3.0 to the CMIP6 ensemble for the SSP1-2.6 and SSP3-7.0 scenarios. As for the historical runs in section 3.1, SURFER v3.0 is forced with CO_2 and CH_4 fossil and land-use emissions, but no other greenhouse gases nor aerosols. Runs are started in 1750 and results for atmospheric CO_2, temperature, surface ocean pH, ocean carbon uptake and land carbon uptake are plotted in Figure 7. Additionally, we compare with outputs from SURFER v2.0, forced with the total CO_2 emissions and run with the parameters and initial conditions described in Martínez Montero et al. (2022).

As already shown in Figure 4, SURFER v3.0 reproduces well the historical CO_2, and for the SPP scenario projections, falls within the lower range of the CMIP6 model ensemble. SURFER v3.0 can simulate a global mean temperature anomaly that generally remains within the CMIP6 range, considering only the effects of CO_2 and methane. This is because the contributions from the other major drivers of temperature changes such as nitrous oxide (N_2O), ozone (O_3), halogenated gases and aerosols approximately cancel each other (Forster et al., 2021, see Figure 7.8). However, between 1960 and 2015, the cooling effect of aerosols from anthropogenic and volcanic sources was likely more significant, and without accounting for this, SURFER v3.0 simulates temperatures slightly above the CMIP6 range.

Surface pH as simulated by SURFER v3.0 generally aligns with the CMIP6 range for both the historical period and SSP projections, an improvement over SURFER v2.0 which showed too rapid ocean acidification. This improvement is primarily due to the addition of a new intermediate layer in SURFER v3.0, which facilitates faster carbon transfer out of the upper ocean layer, thereby slowing surface acidification. This enhanced carbon transfer to intermediate and deep ocean layers also allows the ocean to absorb CO_2 more efficiently. As a result, the ocean carbon uptake in SURFER v3.0 now falls within the CMIP6 model range. The land carbon uptake in SURFER v3.0 and v2.0 are very similar, and both are in the range of CMIP6 models, which is quite large and demonstrates a higher uncertainty.

In Figure 8, we compare the land and ocean sinks of SURFER to four CMIP6 models and one EMIC that have been run to the year 2300 under the SSP1-2.6, SSP3-4.3, and SSP5-8.5 scenarios. We observe that SURFERv3.0 remains within the range of CMIP6-class models even for these longer time scales. For all three scenarios, the land sink is expected to become negative at some point, indicating that the land reservoir will release some of the carbon it had previously absorbed (Canadell et al., 2021; Tokarska et al., 2016; Zickfeld et al., 2013). For the SSP1-2.6 and SSP-3.4 scenarios, this negative land sink in CMIP6 models is attributed to the land carbon-concentration feedback: as CO_2 concentrations decrease after strong negative emissions, vegetation releases carbon. For the SSP5-8.5 scenario, the negative land sink is rather due to a stronger land carbon-climate feedback, where warming leads to a release CO_2 from the land reservoir, for example through increased decomposition rates (Tokarska et al., 2016). In SURFER, the parametrisation of the atmosphere-to-land flux, ($F_{A \to L}$) depends on the atmospheric CO_2 concentration (M_A) but not on temperature, effectively including only a carbon-concentration feedback. This explains why, for the SSP5-8.5 scenario, the land sink in SURFER only becomes slightly negative around 2250, when the atmospheric CO_2 concentrations begin to decline. Despite this, the land sink from SURFER remains mostly in the range of the other models, which is quite large and reflects the large uncertainty in processes related to the terrestrial biosphere.

3.3 LTMIP

In the previous sections, we have seen that SURFER v3.0 can reproduce the historical record and outputs from CMIP6-class models for projections up to 2300. Here, we focus on longer time scales and compare SURFER v3.0 with results from the LTMIP (Long Tail Model Intercomparison Project, Archer et al., 2009). In these experiments, several models were used to assess the CO_2 draw-down from the atmosphere for 10000 years, after emissions pulses of 1000 PgC and 5000 PgC. For each emission pulse, 5 experiments are performed with different physical processes progressively included to assess their impact on atmospheric CO_2 uptake. These experiences are named with a combination of letters indicating the processes included: climate feedbacks (C), sediments (S), weathering (W), and vegetation (V). We reproduce these experiments with SURFER v3.0 by successively reducing the number of active processes. For, the CSWV experiment, we use the standard version of SURFER v3.0. For the CSW experiment, we set $k_{A \to L} = 0$, so that vegetation is kept constant and has no influence on carbon uptake ($F_{A \to L} = 0$). For the CS experiment, we additionally keep the weathering fluxes F_{CaCO_3} and F_{CaSiO_3} constant and equal to their preindustrial values, thus eliminating weathering feedbacks. For the C experiment, we further keep the accumulation and burial fluxes constant and equal to their preindustrial values, thus effectively eliminating interactions with the sediments. Finally for the baseline experiment, on top of all the modifications described above, we keep the solubility and dissociation constants constant. In this last case, SURFER v3.0 is very similar to SURFER v2.0.

Results for these five experiments are visible in Figure 9 for the 1000 PgC pulse, and in Figure 10 for the 5000 PgC pulse. Overall, SURFER v3.0 falls within the range of other models, except in the following cases: the 5000 PgC baseline experiment after 1000 years, the 5000 PgC C experiment between years 1000 and 5000, and the CSWV experiments after year 1000, where SURFER v3.0 simulates slightly lower atmospheric CO2 levels than the other models. For the baseline experiment, SURFER v2.0 doesn't absorb CO_2 from the atmosphere fast enough in the first thousand years after the emission pulse. As already mentioned, this is improved in SURFER v3.0 thanks to the addition of a third oceanic layer at intermediate depth.

We can define and quantify the climate, sediment, weathering, and vegetation feedbacks by taking the difference in simulated atmospheric CO_2 between consecutive experiments (C-baseline, CS-C, CSW-CS, and CSWV-CSW). Results are plotted in Figure 11 for the 1000 PgC pulse, and in Figure 12 for the 5000 PgC pulse. Not all experiments were performed for each model so feedbacks can't always be computed. All experiments are only available for CLIMBER and SURFER v3.0. Overall, the feedbacks in SURFER v3.0 fall within the range of the other models, demonstrating that the associated processes are reasonably well simulated by SURFER. For 5000 PgC pulse experiments, the climate feedback in SURFER v3.0 is very similar to the LOSCAR and GEOCYC models but quite different to the other models. This is probably explained by SURFER V3.0, as well as LOSCAR and GEOCYC, all missing a dynamic ocean circulation and hence feedbacks associated with temperature-induced circulation changes. The sediment feedback in SURFER v3.0 for the 1000 PgC is in the higher range (more negative) of the other models, which is consistent with the dissolution flux being generally larger (accumulation more negative) than in the other models (see Figure 13). For the 5000 PgC, the sediment feedback in SURFER v3.0 is in the mid-to-lower range of the other models, despite the dissolution flux still being in the higher range. In general, other than oceanic invasion, vegetation

has the biggest impact on CO_2 uptake before the year 1000, while sediments have the biggest impact between the year 1000 and 10000.

3.4 cGENIE

Only a few models of intermediate complexity have been run for 100 kyr or more to investigate the carbon cycle's response to (anthropogogenic) CO_2 emissions. Some examples include cGENIE (Colbourn et al., 2013, 2015; Lord et al., 2016), and CLIMBER-X (Kaufhold et al., 2024). Here, we compare SURFER v3.0 with the 1 Myr runs performed with the cGENIE model of intermediate complexity (Lord et al., 2016). This model comprises a 2-D Energy-Moisture Balance atmosphere, a 3-D frictional geostrophic ocean circulation model, and a representation of the global carbon cycle, with ocean cycling of DIC, alkalinity, and a nutrient (PO_4), $CaCO_3$ marine sediments, and terrestrial weathering (Edwards and Marsh, 2005; Ridgwell et al., 2007; Ridgwell and Hargreaves, 2007; Colbourn et al., 2013). For the runs presented here (Lord et al., 2016), cGENIE was used without the terrestrial biosphere module and its associated carbon fluxes. The model had 8 ocean levels, with the surface layer being 175 meters deep, comparable to the surface layer in SURFER v3.0.

We perform equivalent runs in SURFER v3.0 with $k_{A \to L} = 0$ to neglect the role of vegetation. Results are plotted in Figures 14 and 15 for atmospheric CO_2, global mean temperature, ocean surface pH, ocean surface calcite saturation state and $CaCO_3$ content in sediments. Ocean surface calcite saturation state, Ω_U, is defined as

$$\Omega_U = \frac{[CO_3^{2-}]_U [Ca^{2+}]_U}{K_{sp}^{CaCO_3}}. \tag{113}$$

The solubility product $K_{sp}^{CaCO_3} = [CO_3^{2-}]_{sat}[Ca^{2+}]_{sat}$ depends on salinity, temperature and pressure (Mucci, 1983; Millero, 1995). For the computation of Ω_U, we use parametrisations of $K_{sp}^{CaCO_3}$ described in appendix B, and we assume that $[Ca^{2+}]_U$ is constant and equal to $0.01028 \, \mathrm{mol \, kg^{-1}}$ (Sarmiento and Gruber, 2006).

Overall, SURFER v3.0 reproduces well the behaviour of cGENIE. For all emission pulses, the relative difference in simulated atmospheric CO_2 with cGENIE doesn't exceed 18%, is lower than 8% after 1000 yrs and below 5% after 50 kyr. These are smaller differences than those between models for the LTMIP experiments (see Figures 9 and 10). This good agreement for millenial and longer time scales was expected, as SURFER v3.0 was qualitatively tuned to cGENIE's long-term atmospheric CO_2 output. The agreement in ocean surface pH is also very strong, with absolute differences below 0.06 pH units after 5 years, below 0.04 pH units after 1000 years, and below 0.02 pH units after 50 kyr, corresponding to relative difference below 1% after 5 years for all emissions pulses. Because the carbon exchanges between the atmosphere and the surface ocean reach equilibrium relatively fast, the good agreement for ocean surface pH directly results from the good agreement for atmospheric CO_2 concentrations. Regarding temperatures, peak warming occurs later in SURFER v3.0 than in cGENIE, primarily because SURFER models only ocean temperatures, leading to slower global warming compared to cGENIE, which also accounts for the thermal balance of the continents.

After 1 Myr, the state is almost back to equilibrium in SURFER v3.0, with atmospheric CO_2 concentrations ranging from 280.68 ppm for the 1000 PgC emission pulse, to 292.08 ppm for the 20000 PgC pulse. Carbon is removed from the atmo-

sphere through a range of processes. First, atmospheric CO_2 dissolves in the upper ocean layer following the reaction

$$CO_2 + H_2O + CO_3^{2-} \rightleftharpoons 2HCO_3^- , \tag{R9}$$

800 which is equivalent to reactions R1-R3. This causes a decrease in ocean surface pH (acidification) and consumes CO_3^{2-}, which results in a decrease of the surface calcite saturation state. Both these effects are observable in SURFER v3.0 and cGENIE. On centennial to millennial timescales, the CO_3^{2-} anomaly mixes into the ocean interior and deep waters become less saturated, causing an increase in the dissolution of deep-sea $CaCO_3$ sediments and a release of carbonate ions. Some of these carbonate ions can then react with CO_2 (reaction R9), leading to further oceanic CO_2 uptake. This process is called sea-floor

805 neutralisation, as it is the dissolution of previously deposited deep-sea sediments that allows the neutralisation of atmospheric CO_2 (Archer et al., 1997, 1998). Moreover, the increased dissolution of $CaCO_3$ sediments compared to the preindustrial state creates an imbalance between the alkalinity input to the ocean by weathering and the alkalinity output by accumulation. This replenishes the ocean CO_3^{2-} concentration and the erodible $CaCO_3$ sediments stock while leading to a further uptake of atmospheric CO_2. This second process is called terrestrial neutralisation, as it is the (imbalanced) dissolution of carbonate

810 and silicate rocks on land that neutralise the atmospheric CO_2 (Archer et al., 1997, 1998; Ridgwell and Hargreaves, 2007). We observe an overshoot in surface calcite saturation state and deep sea ocean sediment content compared to the preindustrial situation in both SURFER v3.0 and cGENIE because of increased weathering rates due to warming. The extra $CaCO_3$ in the sediments will eventually be buried, leading to a permanent transfer of carbon to the geological reservoir.

4 Sea level rise and importance of long time scale processes

815 So far, we have focused primarily on the carbon cycle, as the additions to SURFER v3.0 are related to it. In this section, we examine sea-level rise (SLR), which is computed as the sum of four contributions: thermosteric (thermal expansion), glaciers, Greenland and Antarctica. The parametrisation for thermosteric sea level rise in SURFER v3.0 is essentially the same as in SURFERv2.0, with the key differences being the use of three 3 ocean layers instead of two, and the use of new thermal expansion coefficients. In subsection 4.1, we verify that these changes still provide a reasonable approximation of

820 thermosteric SLR. The parameterisations for glaciers, Greenland and Antarctica remain unchanged between SURFER v2.0 and SURFER v3.0, so any difference in SLR contributions under a given forcing scenario results only from differences in simulated temperatures. We investigate the SLR contribution from the ice sheets in subsection 4.2.

4.1 Thermosteric sea level rise and ocean heat content

Heat transfer in SURFER v3.0's ocean is controlled by the parameters $\gamma_{U \to I}$ and $\gamma_{I \to D}$. The heat accumulated in ocean layers,

825 along with the corresponding temperature increases, determine thermosteric sea level rise. To ensure that our chosen values for $\gamma_{U \to I}$, $\gamma_{I \to D}$, and for the thermal expansion coefficients are reasonable, we compare the ocean heat content and thermosteric sea level rise in SURFER v3.0 with IPCC estimates for 1971-2018 (Figure 16).

SURFER v3.0 simulates significantly higher ocean heat content above 700 m (layers U+I) than the IPCC estimates, resulting in a larger thermosteric sea level rise. This discrepancy arises for two reasons. First, in SURFER, all energy imbalance is absorbed by the ocean, with no energy allocated to warming the land and atmosphere or for melting glaciers and ice sheets. Consequently, the ocean warms more than it should. Second, and more importantly, SURFER v3.0 doesn't account for faster and larger land temperature increases, which causes the global mean temperature rise to be higher when averaged over land and oceans. In other words, SURFER assumes that the global mean temperature is equivalent to the ocean's mean surface temperature. As a result, SURFER needs more energy to reproduce observed global mean temperatures, and overestimates surface ocean temperatures. For the ocean below 700 m (layer D in SURFER), the ocean heat content and the thermosteric sea level rise simulated by SURFER v3.0 matches the IPCC estimates quite well. This indicates that the oceanic heat transport at depth is a little too slow, which compensates for the ocean receiving more energy than it should.

We also check that our parametrisation for thermosteric sea level rise is valid on longer time scales. In Figure 17, we compare outputs from the intermediate complexity model UVic, versions 2.8 and 2.9 (Eby et al., 2009; Clark et al., 2016), to outputs from SURFER v2.0 and SURFER v3.0. The UVic 2.8 and UVic 2.9 models both include a sediment module and have equilibrium climate sensitivities around 3.5°C, the same as in SURFER. Emission scenarios used to force the models follow historical estimates of CO_2 emissions up to the year 2000. Following this, cumulative emissions of either 1280 or 3840 PgC are added between the years 2000 and 2300. For more details on the experimental setup, see Clark et al. (2016).

SURFER v3.0 has a faster and larger atmospheric CO_2 uptake than both UVic 2.8 and UVic 2.9. This is consistent with the LTMIP experiments (figures 9 and 10) where UVic 2.8 was already the model with the smallest CO_2 uptake after 10000 years for the CSWV experiments. UVic 2.9 has an even slower CO_2 uptake than UVic 2.8 due to the difference in the sediments representation (Clark et al., 2016). For SURFER v2.0, the atmospheric CO_2 concentration reaches equilibrium after $\sim$4000 years since it only takes into account the process of ocean CO_2 invasion. These differences in atmospheric CO_2 concentrations lead to relatively large differences in global mean surface temperatures. Nevertheless, the thermosteric SLR is comparable in all models, except for UVic 2.9 under the 3840 PgC scenario, where it is larger than for the other models. The thermosteric SLR from SURFER v3.0 is close to the one from UVic 2.8 for both scenarios, even though the simulated temperature is lower in SURFER v3.0. This is again a consequence of SURFER not simulating land temperatures. The global mean ocean temperature increase in UVic 2.8 is smaller than its global mean temperature increase, and probably comparable to the mean ocean temperature observed in SURFER v3.0. SURFER v3.0 and SURFER v2.0 also have comparable thermosteric SLR despite SURFER v2.0 simulating a larger temperature increase. This is because the ocean in SURFER v3.0 is deeper than in SURFER v2.0 (3800 m deep vs 3150 m) and has thus more potential for expansion.

4.2 Ice sheets

In SURFER v2.0, atmospheric CO_2 concentrations, and hence temperatures, stabilise a few thousand years after the end of emissions. In SURFER v3.0, thanks to new processes added in the carbon cycle, CO_2 drawdown from the atmosphere continues until return to preindustrial conditions, leading to lower temperatures than in SURFER v2.0 on millennial and longer time scales. Since ice sheets respond on the millennial time scale, we expect these differences to have a significant impact on

their melting. To test this, we force both SURFER v3.0 and SURFER v2.0 with the CO_2 emissions from five SSP scenarios (SSP1-2.6, SSP2-4.5, SSP4-6.0, SSP3-7.0, SSP5-8.5) which cover a range of possibles futures. Simulations last for 500 kyr and results are plotted in Figure 18.

865   In SURFER, the ice sheets are designed as tipping elements (see section 2.3). For both SURFER v2.0 and SURFER v3.0, and under all scenarios, the simulated temperature increase overshoots the critical warming threshold of the Greenland ice sheet. However, the Greenland ice sheet doesn't always collapse. Indeed, in general, tipping can be avoided if the overshoot duration is short relative to the effective time scale of the tipping element (Ritchie et al., 2019, 2021). For SURFER v2.0 this happens for the SSP1-2.6 scenario. For all other scenarios, the temperature stabilises past the critical threshold and thus

870   Greenland eventually transitions to a completely melted state. In SURFER v3.0, thanks to a greater decrease in temperature after reaching a maximum, Greenland overshoots safely its critical threshold also under SSP2-4.5 and SSP4-6.0 scenarios. This happens even though peak warming reaches 2.62 °C and 3.18 °C respectively, well above the Greenland ice sheet's critical threshold of 1.52 °C (as set in SURFER). For these scenarios, This leads to a ∼6 m reduction in the long-term sea level rise contribution simulated by SURFER v3.0 compared to SURFER v2.0.

875   Meanwhile, The Antarctic Ice Sheet doesn't tip in our simulations, regardless of using SURFER v2.0 or SURFER v3.0. This is because the critical warming threshold for the Antarctic ice sheet, set to 6.8 °C in SURFER, is much higher than that for Greenland and seldom reached, even for the SSP5-8.5 scenario. However, despite no changes in the tipping behaviour, differences in simulated temperatures still give rise to large differences in SLR contribution, particularly for high-emission scenarios. The long-term sea level rise contributions from Antarctica for the SSP3-7.0 and SSP5-8.5 scenarios are respectively

880   reduced by ∼8 m and ∼18 m in SURFER v3.0 compared to SURFERv2.0.

5   Discussion

Our primary goal with SURFER v3.0 was to improve the representation of carbon cycle dynamics to enable simulations of the Earth system on multi-millennial time scales. To this end, we have added to SURFER v2.0 a dynamic and more precise representation of alkalinity, an explicit representation of the carbonate and soft-tissue pumps, a sediments reservoir with associated

885   accumulation and burial fluxes, and weathering as well as volcanic out-gassing fluxes. We have shown that these additions allow for an accurate simulation of carbon cycle dynamics on multi-millennial time scales by comparing SURFER v3.0 to the outputs from the LTMIP experiments, and to the outputs of cGENIE for 1 Myr runs. Furthermore, we showed that the stabilisation of atmospheric CO_2 and temperature at lower levels in SURFER v3.0 than in SURFER v2.0 leads to a significant reduction in simulated sea level rise. While this outcome is robust, the tipping behavior of the Greenland ice sheet in response

890   to specific emissions scenarios is sensitive to the choice of model parameters. For the parameter set used in this study (see Tables 2 and 3), we found that, in contrast to SURFER v2.0, Greenland avoids tipping in SURFER v3.0 under intermediate emissions scenarios SSP2-4.5 and SSP4-6.0.

A secondary goal with SURFER v3.0 was to improve on SURFER v2.0 for the decadal to centennial time scales. This was done by adding an ocean layer of intermediate depth, a temperature and pressure dependence of the solubility and dissociation

constants, a representation of atmospheric methane, and by carefully setting the initial conditions of the oceanic variables
based on the GLODAP dataset. We have shown that SURFER v3.0 successfully reproduces the historical CO_2 and CH_4
concentrations, the estimated historical land and ocean sinks, the CMIP6 ensemble mean for the evolution of different quantities
under the SSP1-2.6 and SSP3-7.0 scenarios, and that in all these tasks it performs equally well or better than SURFER v2.0.

In summary, SURFER v3.0 outperforms SURFER v2.0 on all time scales, and despite having doubled the number of differ-
ential equations, it stays fast, transparent and easy to modify. This manuscript contains all the equations for the model, all the
parameter values, and the initial conditions for all the variables. SURFER v3.0 is coded in Python, which is one of the most
widely used open-source programming languages. The code of the model, as well as the code for all the figures, is available
online in a Jupyter notebook, providing already a wide range of example use cases.

Of course, many coupled atmosphere-ocean box models of the carbon cycle already exist, some of them including carbonate
sediments and weathering processes (Keir, 1988; Munhoven and François, 1996; Lenton and Britton, 2006; Zeebe, 2012;
Köhler and Munhoven, 2020). These models, often primarily focused on the ocean, offer a more complex representation of the
carbon cycle than SURFER v3.0. For instance, BICYCLE-SE (Köhler and Munhoven, 2020) includes 1 atmospheric box, 10
ocean boxes (5 surface boxes), ocean cycling of DIC, alkalinity, dissolved oxygen, and phosphate, sediment columns in each
ocean basin and at various depths, and 7 terrestrial biosphere boxes. Still, despite being simpler, SURFER v3.0 effectively
captures the essential dynamics of the carbon cycle, as demonstrated in the precedent sections.

Moreover, SURFER includes a dynamic representation of temperature and sea level rise, which is often lacking in other
models where those quantities are constant or prescribed. Among existing models, the one from Lenton and Britton (2006)
is the closest to SURFER v3.0, with 4 ocean boxes, 10 sediment boxes, 2 terrestrial biosphere boxes, and a weathering flux
parameterisation. As in SURFER v3.0, its carbon cycle is coupled with an energy balance representation of global mean
temperature and both models can be classified as "simple Earth system models". While it is possible to integrate SURFER's
temperature equations and sea level rise parameterisation into other models, we believe the unique combination of included
processes, simplicity, transparency, and speed makes SURFERv3.0 a valuable addition to the literature, on top of being a
worthwhile update to SURFER v2.0.

Although we are quite satisfied with SURFER's capabilities, we are certainly not claiming it is *the one model to rule them
all*. Indeed, being that simple comes with several limitations that we discuss here.

First, SURFER v3.0 lacks horizontal resolution. In particular, SURFER v3.0 has no high latitude ocean surface box, which
is a feature of most ocean carbon cycle box models and could help with simulating more realistically the atmosphere-to-ocean
CO_2 flux. The lack of spatial resolution also implies that SURFER v3.0 doesn't represent land temperatures, hence equating
global mean temperatures with ocean mean surface temperatures. As shown in section 4.1, this leads to an overestimation of
ocean surface temperature and thermosteric SLR for historical and SSP forced runs.

Additionally, several oceanic and land carbon-climate feedbacks are missing in SURFER v3.0. For example, there is no
dynamic ocean circulation and as such, changes in atmosphere-to-ocean CO_2 fluxes resulting from climate-induced changes in
the oceanic circulation are not represented. This was suggested in section 3.3 by comparing the "climate feedback" of SURFER
v3.0 with other models for the 5000 PgC pulse LTMIP experiment. A second example is the organic matter and $CaCO_3$

930 productions in the upper ocean layer that are kept constant, neglecting eventual changes in marine ecosystem production and associated carbon uptake. Last but not least, is our parametrisation of atmosphere-to-land carbon flux, which depends on the atmospheric CO_2 concentration, but not on temperature. As explained in section 3.2, this is probably the reason why SURFER's land sink stays positive longer than other models for high-emission scenarios. Furthermore, this parametrisation doesn't account for hypothesised tipping elements such as the Amazon and boreal forests or the permafrost, which may release

935 important amounts of greenhouse gases past critical warming thresholds (Armstrong McKay et al., 2021).

Moreover, SURFER lacks a detailed representation of land surface-vegetation-albedo feedbacks, which can influence temperatures and hydroclimate on decadal to multi-centennial timescales through changes in vegetation cover (Forster et al., 2021; Willeit et al., 2014; Feng et al., 2022). In the current model, these feedbacks are indirectly represented via the climate feedback parameter β (see *Biogeophysical feedbacks* in IPCC (2021a), p 976). However they are not explicitly linked to the land carbon

940 reservoir (M_L), the variable most closely associated with vegetation cover. This limitation, combined with the absence of a hydrological cycle and horizontal spatial resolution, constrains SURFER's ability to capture the full consequences of vegetation feedbacks. For example, SURFER may fail to account for their contribution to polar amplification (Willeit et al., 2014; Swann et al., 2010) and their subsequent impact on sea level changes. Simulations of the last glacial inception by Willeit et al. (2023) demonstrated that dynamic vegetation responses led to an additional 15-meter decrease in sea level, highlighting the critical

945 role of these feedbacks in shaping long-term Earth system trajectories.

For the sea level rise module, the contribution of the Antarctic ice sheet should probably be split into several components. Indeed, it has been shown that the West Antarctic ice sheet, as well as some East Antarctic subglacial basins, could collapse for lower warming thresholds than the East Antarctic ice sheet and contribute to several meters of sea level rise already by 2300 for high emission scenarios (Garbe et al., 2020; Alley et al., 2015; Coulon et al., 2024).

950 Finally, in its current state, SURFFER v3.0 accounts for only one process influencing the carbon cycle on the 100 kyr timescale: the weathering of silicate rocks. Other potentially important processes acting on these time scales, such as orbital forcing variations, are currently neglected. These variations modulate the seasonal and spatial repartition of incoming solar energy and are known to drive or act as a pacemaker of the Quaternary glacial cycles (Hays et al., 1976).

Also neglected in SURER, organic carbon burial may influence the climate system through its role in long-term carbon se-

955 questration (Berner, 2004; Archer, 2010). For instance, during past oceanic anoxic events, reduced oxygen levels inhibited remineralisation processes, resulting in increased organic carbon preservation and burial in sediments and decreased atmospheric CO_2 levels (Schlanger and Jenkyns, 1976; Barclay et al., 2010). As warming is suspected to lead to oceanic deoxygenation due to reduced oxygen solubility and enhanced weathering fluxes (Schmittner et al., 2008; Ruvalcaba Baroni et al., 2020), organic carbon burial may act as a negative feedback mechanism that mitigates warming.

960 In addition, organic carbon plays a critical role in carbonate sedimentation. In oxic pore waters, the respiration of organic matter creates acidic micro-environments that enhance the dissolution of $CaCO_3$ sediments (Sarmiento and Gruber, 2006). Incorporating organic carbon burial into SURFER would require adding a sediment reservoir for organic carbon, along with accumulation and burial fluxes, similar to the implementation of $CaCO_3$ burial. Ideally, the model should also account for the flux of organic carbon from land to the ocean through river input and exchange fluxes between ocean layers due to oceanic

965 circulation. While these modifications are conceptually straightforward, parameterising the fluxes would require incorporating oxygen and nutrient cycling, which is essential to determine the rates of organic carbon production and remineralisation. Implementing these features would demand additional effort but offer a more comprehensive representation of the long-term carbon cycle and enable the study of oceanic anoxic events.

6 Conclusions

970 We have presented SURFER v3.0, a simple Earth system model that includes a dynamic carbon cycle and simulates various important quantities such as atmospheric CO_2 and CH_4 concentrations, temperature anomalies, ocean surface pH, and sea-level rise in response to anthropogenic greenhouse gases emissions. SURFER v3.0 extends SURFER v2.0 by incorporating dynamic alkalinity cycling, $CaCO_3$ sediments, and weathering processes. These additions enable SURFER v3.0 to accurately simulate the dynamics of the coupled carbon-climate system over timescales ranging from decades to millions of years. We

975 have validated this by comparing SURFER v3.0 to historical data and outputs from GCMs, EMICs, and other box models.

We have also demonstrated that SURFER v3.0 can simulate thermosteric sea-level rise reasonably well on millennial timescales, though it tends to overestimate it for shorter timescales. Furthermore, we have shown that incorporating long-term carbon cycle processes in SURFER v3.0 leads to a significant reduction in simulated contributions of Greenland and Antarctica to sea-level rise, compared to SURFER v2.0. These results highlight the critical importance of considering these

980 processes to better predict committed sea-level changes.

SURFER v3.0 is fast, transparent, easy to modify and use, and hence an ideal tool for policy assessments that wish to take into account centennial to multi-millennial time scales. In the future, we plan to add to SURFER a representation of glacial cycle dynamics and include several tipping elements to investigate the stability of the Earth system and the impact of anthropogenic emissions on its future long-term trajectories.

985 *Code availability.* The exact version of SURFER used to produce the results showed in this paper is archived on Zenodo (https://zenodo.org/ records/12774162, Couplet et al., 2024), as is the input data to run the model and most of the data to produce the plots. The code of SURFER is licensed under MIT license.

Data availability. Data from other references used in this paper for emission scenarios are as follows :

- Historical CO_2 emissions are from Friedlingstein et al. (2022) and are available at https://doi.org/10.18160/GCP-2022.

990 - Historical CH_4 emissions are from Jones et al. (2023) and are available at https://zenodo.org/records/10839859.

- CO_2 and CH_4 emissions for the SSP scenarios are available in the SSP database hosted by the IIASA Energy Program at https://tntcat.iiasa.ac.at/SspDb.

Data from other references used in this paper for comparison with SURFER's output are as follows :

Table 2. Parameters for the carbon cycle component. The rightmost column lists references used for parameter tuning and, where applicable, the calibration targets to which the parameters were fitted. The calibration to other models is performed qualitatively, without optimising well-defined metrics.

Symbol	Comment	Value	Ref/Calibration
$F_{\mathrm{CaCO_3,0}}$	PI weathering of carbonate rocks	$0.065\ \mathrm{PgC\,yr^{-1}}$	Sarmiento and Gruber (2006), Lord et al. (2016)
$F_{\mathrm{CaSiO_3,0}}$	PI weathering of silicate rocks	$0.065\ \mathrm{PgC\,yr^{-1}}$	Sarmiento and Gruber (2006), Lord et al. (2016)
k_{Ca}	parametrisation of carbonate weathering flux	$0.049\ \mathrm{K^{-1}}$	Lord et al. (2016)
k_{T}	parametrisation of silicate weathering flux	$0.095\ \mathrm{K^{-1}}$	Colbourn et al. (2013), fitted to cGENIE runs (Fig. 14)
$k_{\mathrm{A\to L}}$	controls rate of carbon uptake by vegetation	$0.044\ \mathrm{yr^{-1}}$	Fitted to historical and CMIP6 data (Figs. 4,6,7)
β_{L}	controls amount of carbon uptake by vegetation	1.7	value used in SURFER v2.0
$\bar{k}_{\mathrm{A\to U}}$	controls rate of air-sea CO_2 exchanges	$4.7\ \mathrm{kg\,(mol\,yr)^{-1}}$	Determined from physics + Yang et al. (2022)
$k_{\mathrm{U\to I}}$	DIC transfer via ocean mixing (U-I)	$0.13\ \mathrm{yr^{-1}}$	Fitted to historical and CMIP6 data (Figs. 4,6,7)
$k_{\mathrm{I\to D}}$	DIC transfer via ocean mixing (I-D)	$0.009\ \mathrm{yr^{-1}}$	fitted to cGENIE runs (Fig. 14)
$\tilde{k}_{\mathrm{U\to I}}$	Alk transfer via ocean mixing (U-I)	$0.13\ \mathrm{yr^{-1}}$	Fitted to historical and CMIP6 data (Figs. 4,6,7)
$\tilde{k}_{\mathrm{I\to D}}$	Alk transfer via ocean mixing (I-D)	$0.009\ \mathrm{yr^{-1}}$	fitted to cGENIE runs (Fig. 14)
P^{org}	organic matter export at 150 m	$7\ \mathrm{PgC\,yr^{-1}}$	Sarmiento and Gruber (2006)
$P^{\mathrm{CaCO_3}}$	$CaCO_3$ export at 150 m	$1\ \mathrm{PgC\,yr^{-1}}$	Sarmiento and Gruber (2006)
$\phi_{\mathrm{I}}^{\mathrm{org}}$	fraction of org. matter rain that remin. in layer I	0.72	Based on Eq 5.4.3 in Sarmiento and Gruber (2006)
$\phi_{\mathrm{I}}^{\mathrm{CaCO_3}}$	fraction of $CaCO_3$ rain that dissolves in layer I	0.15	Based on Archer et al. (1998)
$\phi_{\mathrm{D}}^{\mathrm{CaCO_3}}$	fraction of $CaCO_3$ rain that dissolves in layer D	0.39	Based on Archer et al. (1998)
$\sigma_{\mathrm{Alk:DIC}}$	Alk to DIC changes in organic matter production	$-16/117$	Sarmiento and Gruber (2006)
α_{diss}	parametrisation of $CaCO_3$ sediments dissolution	$-1.07\times10^{-2}\ \mathrm{PgC\,yr^{-1}(\mu mol\,kg^{-1})^{-1}}$	Based on Archer et al. (1998)
β_{diss}	parametrisation of $CaCO_3$ sediments dissolution	$1.82\times10^{-5}\ \mathrm{yr^{-1}}$	Based on Archer et al. (1998)
γ_{diss}	parametrisation of $CaCO_3$ sediments dissolution	$-4.53\times10^{-6}\ \mathrm{yr^{-1}\,(\mu mol\,kg^{-1})^{-1}}$	Based on Archer et al. (1998)
$\tau_{\mathrm{CH_4}}$	atmospheric lifetime of methane	$9.5\ \mathrm{yr}$	Saunois et al. (2020), fitted to hist. CH_4 conc. (Fig. 5)
V	volcanic outgassing	$F_{\mathrm{CaSiO_3,0}}$	Computed from equilibrium conditions (Eq 87-96)
$k_{\mathrm{I\to U}}$	DIC transfer via ocean mixing (I-U)	eq 97	Computed from equilibrium conditions (Eq 87-96)
$k_{\mathrm{D\to I}}$	DIC transfer via ocean mixing (D-I)	eq 98	Computed from equilibrium conditions (Eq 87-96)
$\tilde{k}_{\mathrm{I\to U}}$	Alk transfer via ocean mixing (I-U)	eq 99	Computed from equilibrium conditions (Eq 87-96)
$\tilde{k}_{\mathrm{D\to I}}$	Alk transfer via ocean mixing (D-I)	eq 100	Computed from equilibrium conditions (Eq 87-96)
$F_{\mathrm{diss,0}}$	parametrisation of $CaCO_3$ sediments dissolution	eq 101	Computed from equilibrium conditions (Eq 87-96)
α_{burial}	parametrisation of $CaCO_3$ sediments burial	$(F_{\mathrm{CaCO_3,0}} + F_{\mathrm{CaSiO_3,0}})/M_{\mathrm{S}}(t_{\mathrm{PI}})$	Computed from equilibrium conditions (Eq 87-96)
$E_{\mathrm{nat}}^{\mathrm{CH_4}}$	natural methane emissions	$M_{\mathrm{CH_4}}(t_{\mathrm{PI}})/\tau_{\mathrm{CH_4}}$	Computed from equilibrium conditions (Eq 87-96)

Table 3. Parameters for the climate component. The values are the same as for SURFER v2.0 (Martínez Montero et al., 2022).

Symbol	Comment	Value
$F_{2\times}$	extra radiative forcing due to a doubling of atmospheric CO_2	$3.9 \, \mathrm{W \, m^{-2}}$
β	climate feedback parameter	$1.1143 \, \mathrm{W \, m^{-2} \, {}^\circ C^{-1}}$
$\gamma_{U \to I}$	parametrisation of heat exchange between ocean layers	$0.8357 \, \mathrm{W \, m^{-2} \, {}^\circ C^{-1}}$
$\gamma_{I \to D}$	parametrisation of heat exchange between ocean layers	$0.8357 \, \mathrm{W \, m^{-2} \, {}^\circ C^{-1}}$
α_{CH_4}	parametrisation of radiative forcing of methane	$0.791 \, \mathrm{W \, m^{-2} \, PgC^{-1/2}}$
α_{SO_2}	parametrisation of radiative forcing of SO_2	$65 \, \mathrm{W \, m^{-2}}$
β_{SO_2}	parametrisation of radiative forcing of SO_2	$2246 \, \mathrm{TgS \, yr^{-1}}$
γ_{SO_2}	parametrisation of radiative forcing of SO_2	0.23

Table 4. Parameter values for the sea level rise component. The values used for the mountain glaciers parametrisation are the same as for SURFER v2.0 (Martínez Montero et al., 2022). The values of the thermal expansion coefficients are computed based on the GLO-DAPv2.2016b mapped climatology Lauvset et al. (2016).

Parameter	Comment	Value
$S_{\mathrm{gl\,pot}}$	sea level rise potential from mountain glaciers	$0.5 \, \mathrm{m}$
ξ	sensitivity coefficient for glacier parametrisation	$2 \, {}^\circ C$
τ_{gl}	timescale for glacier melt	$200 \, \mathrm{yr}$
α_U	thermal expansion coefficient for layer U	$2.20 \times 10^{-4} \, \mathrm{K^{-1}}$
α_I	thermal expansion coefficient for layer I	$1.61 \times 10^{-4} \, \mathrm{K^{-1}}$
α_D	thermal expansion coefficient for layer D	$1.39 \times 10^{-4} \, \mathrm{K^{-1}}$

Table 5. Parameter values used for Greenland and Antarctic ice sheets. The values are the same as for SURFER v2.0 (Martínez Montero et al., 2022).

Parameter	Greenland's value	Antarctica's value
T_+	1.52 °C	6.8 °C
T_-	0.3 °C	4.0 °C
V_+	0.77	0.44
V_-	0.3527	-0.3200
τ_+	5500 yr	5500 yr
τ_-	470 yr	3000 yr
k_τ	0.001	0.001
S_{pot}	7.4 m	55 m

Table 6. GLODAPv2.2016b quantities averaged over ocean layers equivalent to those of SURFER.

	Upper layer (0-150 m)	Intermediate layer (150-650 m)	Deep layer (650-3800 m)
Preindustrial DIC ($\mu\text{mol}\,\text{kg}^{-1}$)	2017.65	2152.62	2266.57
Total alkalinity ($\mu\text{mol}\,\text{kg}^{-1}$)	2310.61	2310.60	2367.21
Temperature (°C/ °K)	16.34 / 289.49	8.95 / 282.10	2.65 / 275.80
Salinity (psu)	34.93	34.77	34.70

Table 7. Initial conditions for SURFER v3.0. The upper part of the table correspond to the model 17 variables. The lower part of the table fixes salinity and preindustrial temperature, this is necessary to compute the dissociation constants and the solubility constant of CO_2.

Variable	Comment	Initial (PI) Value
M_A	mass of carbon in atmospheric CO_2	580.27 PgC
$M_A^{CH_4}$	mass of carbon in atmospheric CH_4	1.49 PgC
M_L	mass of carbon on land (soils+vegetation)	2200 PgC
M_L^*	additional land variable that integrates land-use emission	2200 PgC
M_U	dissolved inorganic carbon mass in ocean layer U	1344.78 PgC
M_I	dissolved inorganic carbon mass in ocean layer I	4772.02 PgC
M_D	dissolved inorganic carbon mass in ocean layer D	31655.16 PgC
Q_U	alkalinity mass in ocean layer U	1536.67 PgC
Q_I	alkalinity mass in ocean layer I	5122.24 PgC
Q_D	alkalinity mass in ocean layer D	33060.77 PgC
M_S	erodible $CaCO_3$ sediments mass	1600 PgC
δT_U	temperature anomaly in ocean layer U	0 K
δT_I	temperature anomaly in ocean layer I	0 K
δT_D	temperature anomaly in ocean layer D	0 K
S_{gl}	sea level rise contribution from mountain glaciers	0 msle
V_{GIS}	volume fraction of Greenland ice sheet with respect to preindustrial value	1
V_{AIS}	volume fraction of Antarctic ice sheet with respect to preindustrial value	1
S_U	salinity of ocean layer U (constant)	34.93 psu
S_I	salinity of ocean layer I (constant)	34.77 psu
S_D	salinity of ocean layer D (constant)	34.70 psu
$T_{U,0}$	preindustrial temperature of ocean layer U (constant)	288.38 K
$T_{I,0}$	preindustrial temperature of ocean layer I (constant)	281.75 K
$T_{D,0}$	preindustrial temperature of ocean layer D (constant)	275.76 K
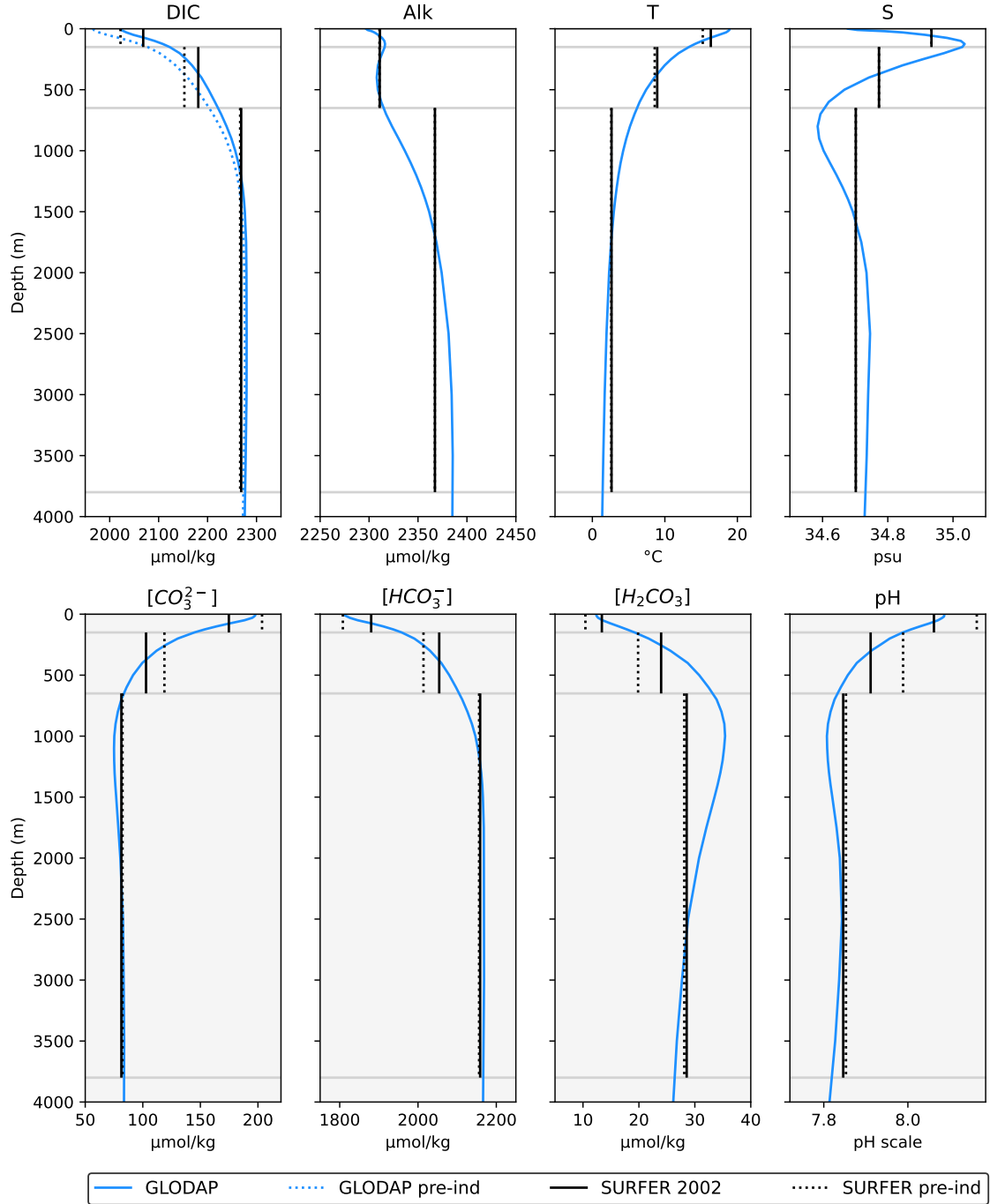
Figure 3. Horizontally averaged quantities from the GLODAPv2.2016b mapped climatologies (Lauvset et al., 2016) compared to initial and simulated values by SURFER v3.0. The carbonate species are not provided in the GLODAP climatologies. We computed their values at each ocean point based on the climatologies of DIC, Alk, temperature and salinity, and then averaged them horizontally. Details for the computation of the carbonates species are in appendix C.
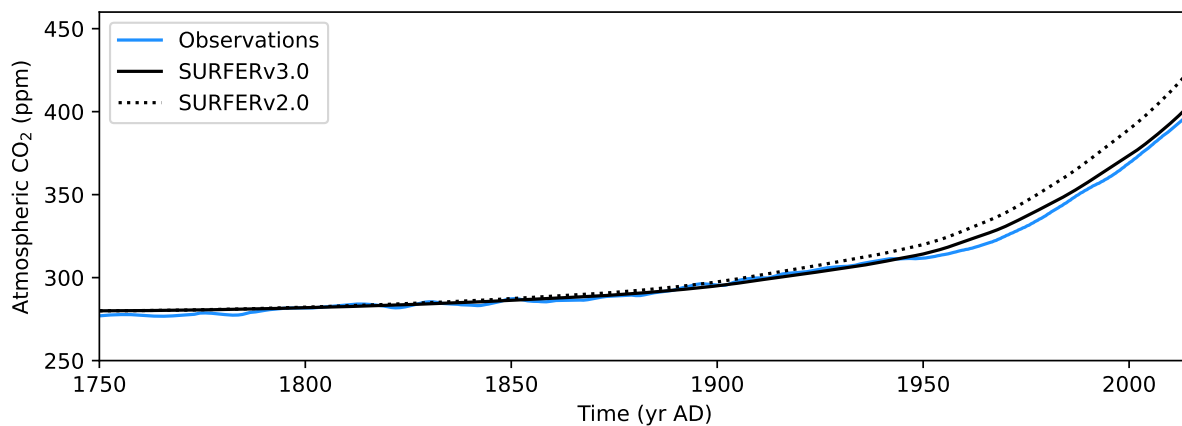
Figure 4. Historical atmospheric CO_2 concentrations. Comparaison between (smoothed) observations (Köhler et al., 2017) and outputs from SURFER v2.0 and SURFER v3.0 when forced with historical emissions.
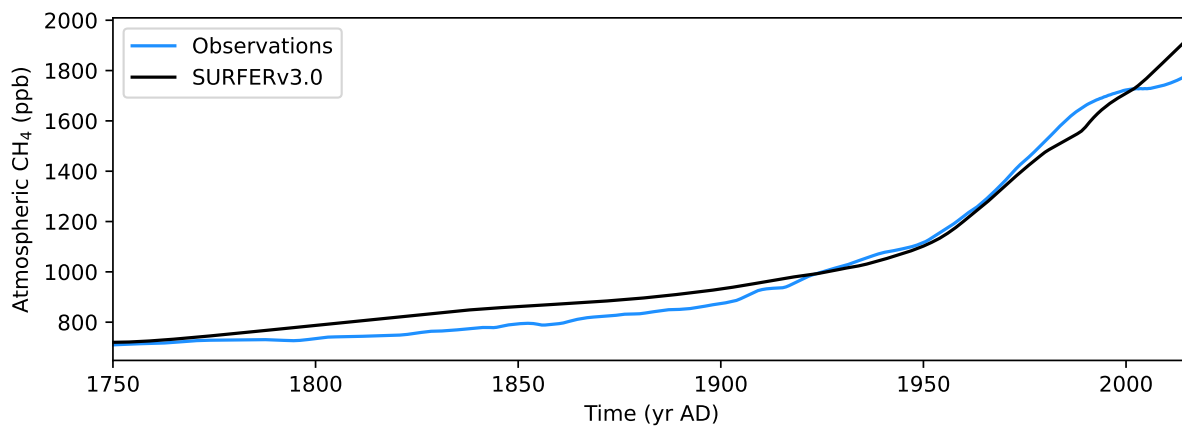
Figure 5. Historical atmospheric CH_4 concentrations. Comparaison between (smoothed) observations (Köhler et al., 2017) and outputs from SURFER v3.0 when forced with historical emissions.
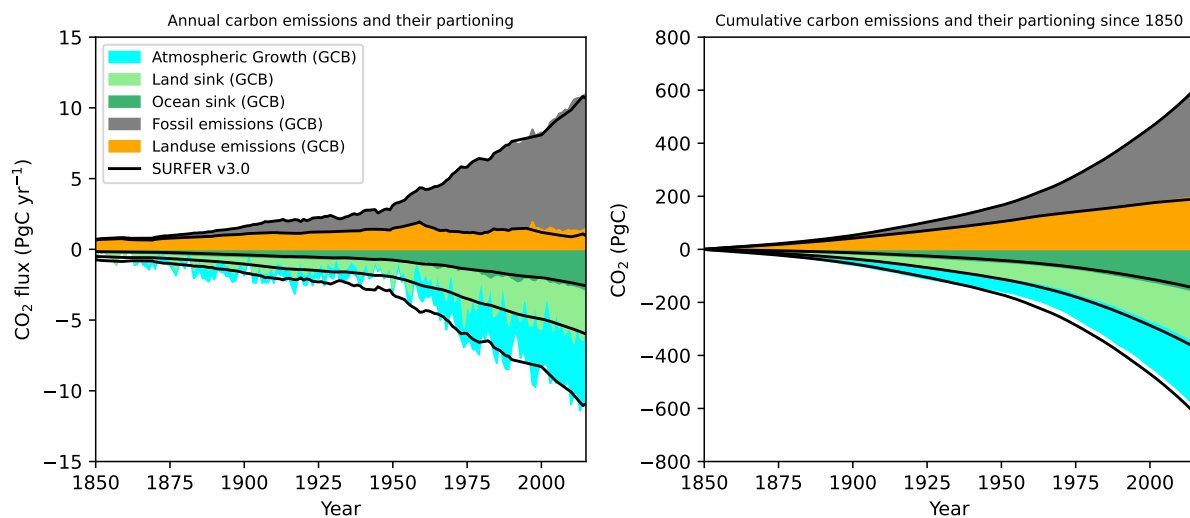
Figure 6. Partitionning of fossil and land-use CO_2 emissions in the atmosphere, ocean and land in SURFER v3.0 compared to estimates from the Global Carbon Budget (GCB) (Friedlingstein et al., 2022).
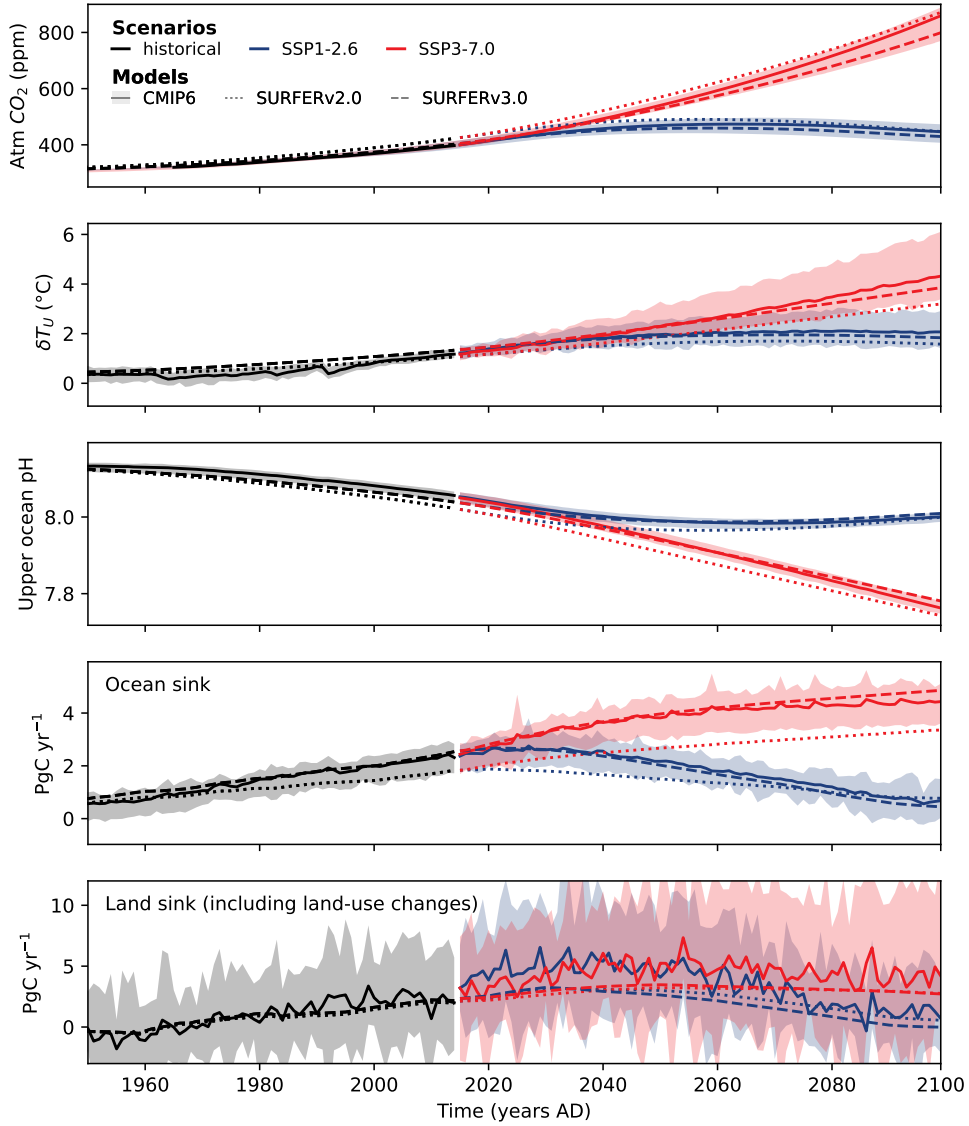
Figure 7. Comparison between SURFER v3.0, SURFER v2.0 and the CMIP6 model ensemble mean for the historical period (1750-2014) and the near future (2015-2100) under SSP1-2.6 and SSP3-7.0 scenarios. The CMIP6 data is from concentration driven runs, except the atmospheric CO_2 which comes from emission driven runs. The ocean sink is computed in SURFER as $F_{A \to U} - F_{A \to U}(t_{PI})$. The land sink is taken here as the Net Biome Produtivity (NBP) which includes land-use fluxes. In SURFER, it is computed as $F_{A \to U} - E_{\text{land-use}}^{CO_2} - E_{\text{land-use}}^{CH_4}$.
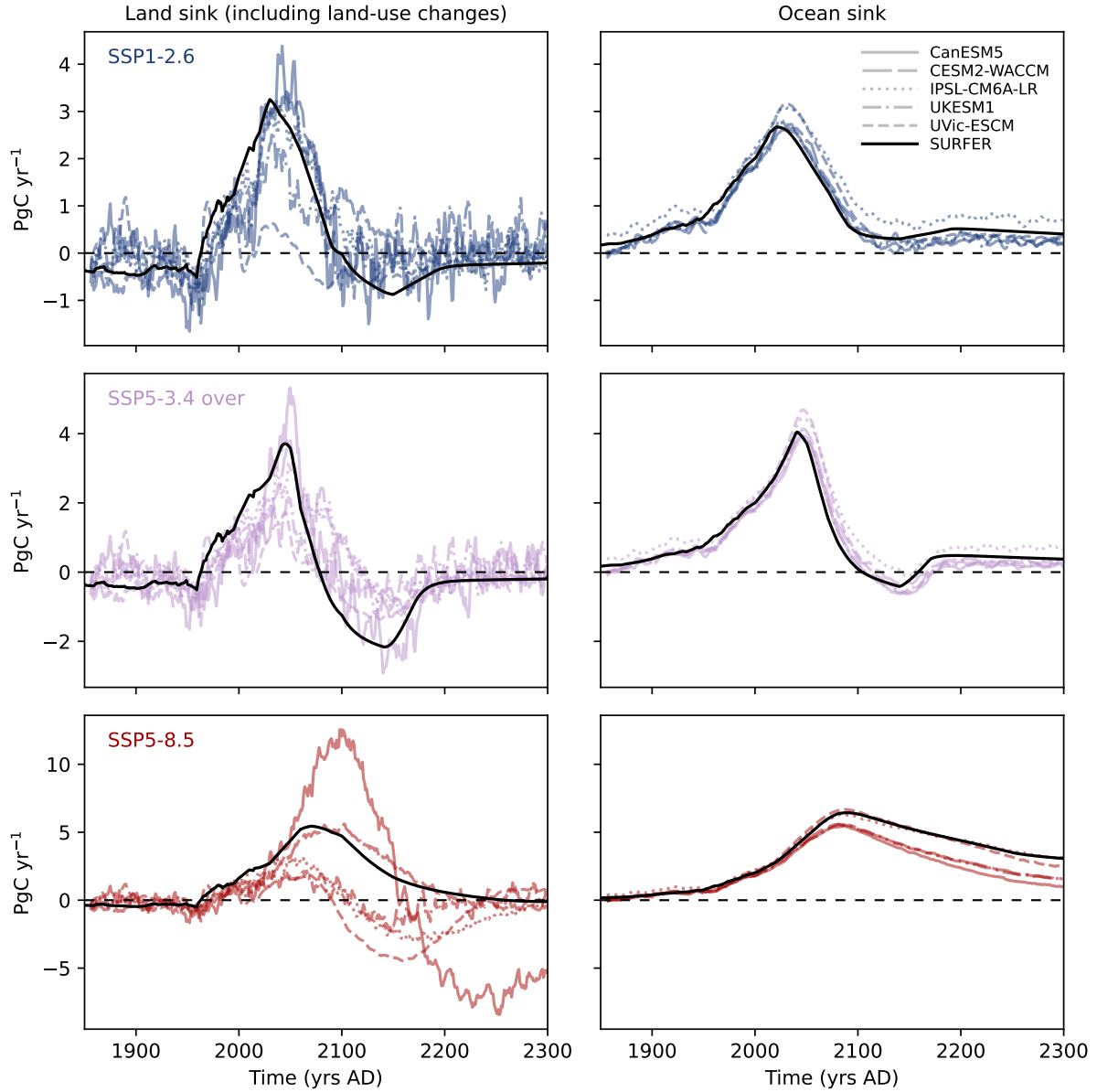
Figure 8. Comparison of atmosphere-to-ocean and atmosphere-to-land carbon fluxes as simulated by SURFER v3.0 and CMIP6 models for the historical period (1750-2014) and the future (2015-2300) under SSP1-2.6, SSP5-3.4 over, and SSP5-8.5 scenarios. The ocean sink is computed in SURFER as $F_{A \to U} - F_{A \to U}(t_{PI})$. The land sink is taken here as the Net Biome Produtivity (NBP) which includes land-use fluxes. In SURFER, it is computed as $F_{A \to U} - E_{\text{land-use}}^{CO_2} - E_{\text{land-use}}^{CH_4}$.
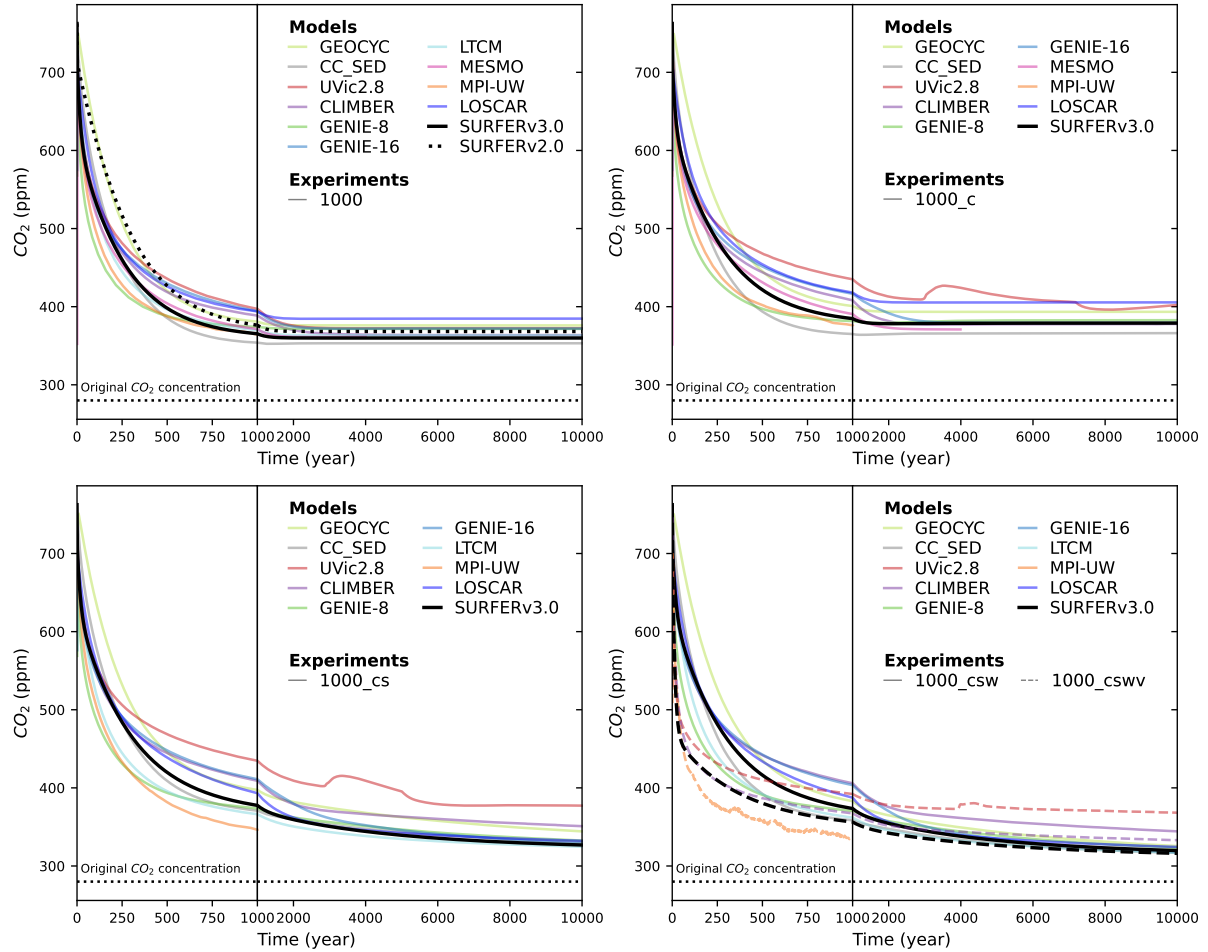
Figure 9. Atmospheric CO_2 simulated by different models and SURFER v3.0 after a 1000 PgC emission pulse for the LTMIP experiments. The five experiments are the baseline (ocean only) experiment, the climate (C), the climate plus sediments (CS), the climate plus sediments plus weathering (CSW) and the climate plus sediments plus weathering plus vegetation (CSWV) experiments. We have added the results of the LOSCAR model (Zeebe, 2012) which wasn't part of the original LTMIP publication (Archer et al., 2009).
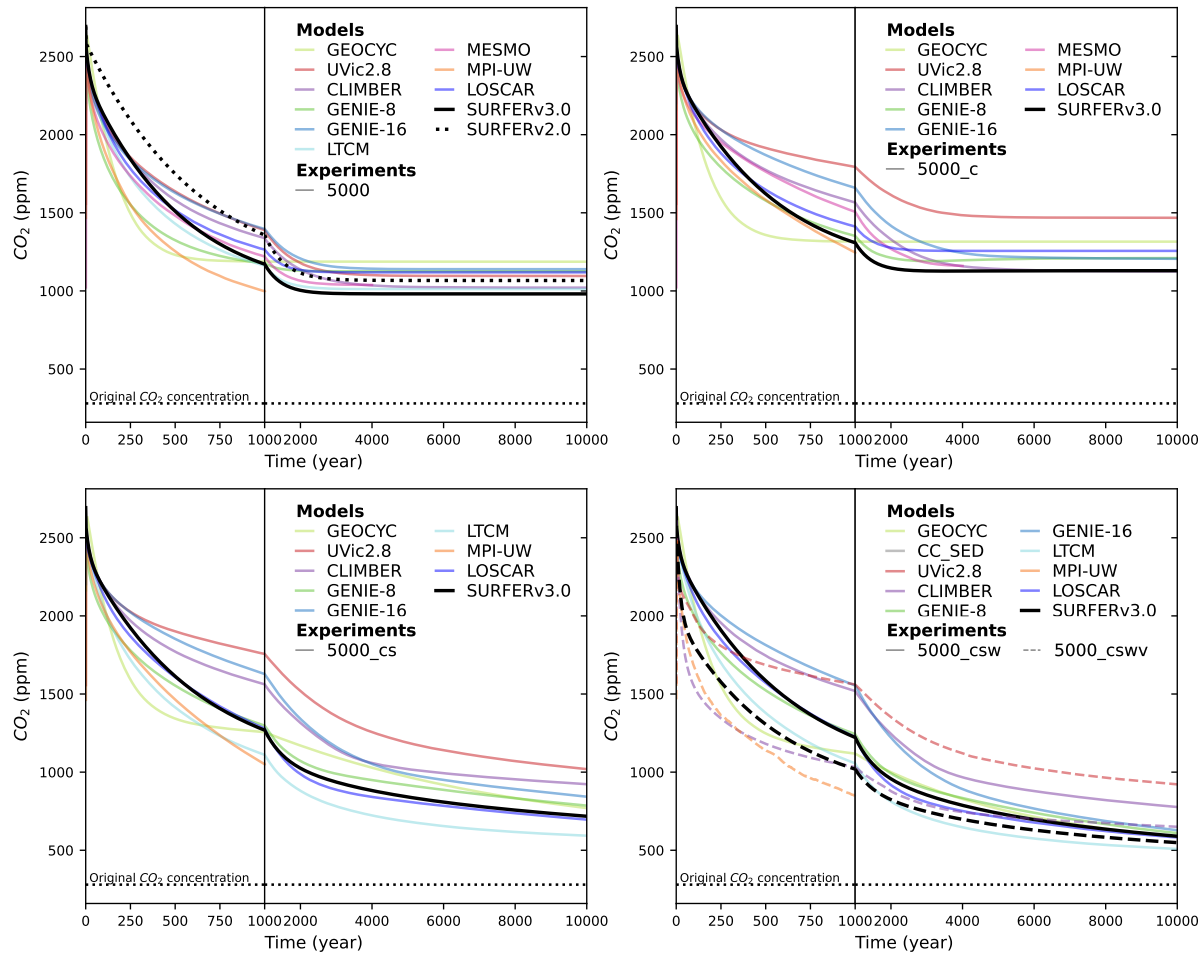
Figure 10. Atmospheric CO_2 simulated by different models and SURFER v3.0 after a 5000 PgC emission pulse for the LTMIP experiments. The five experiments are the baseline (ocean only) experiment, the climate (C), the climate plus sediments (CS), the climate plus sediments plus weathering (CSW) and the climate plus sediments plus weathering plus vegetation (CSWV) experiments. We have added the results of the LOSCAR model (Zeebe, 2012) which wasn't part of the original LTMIP publication (Archer et al., 2009).
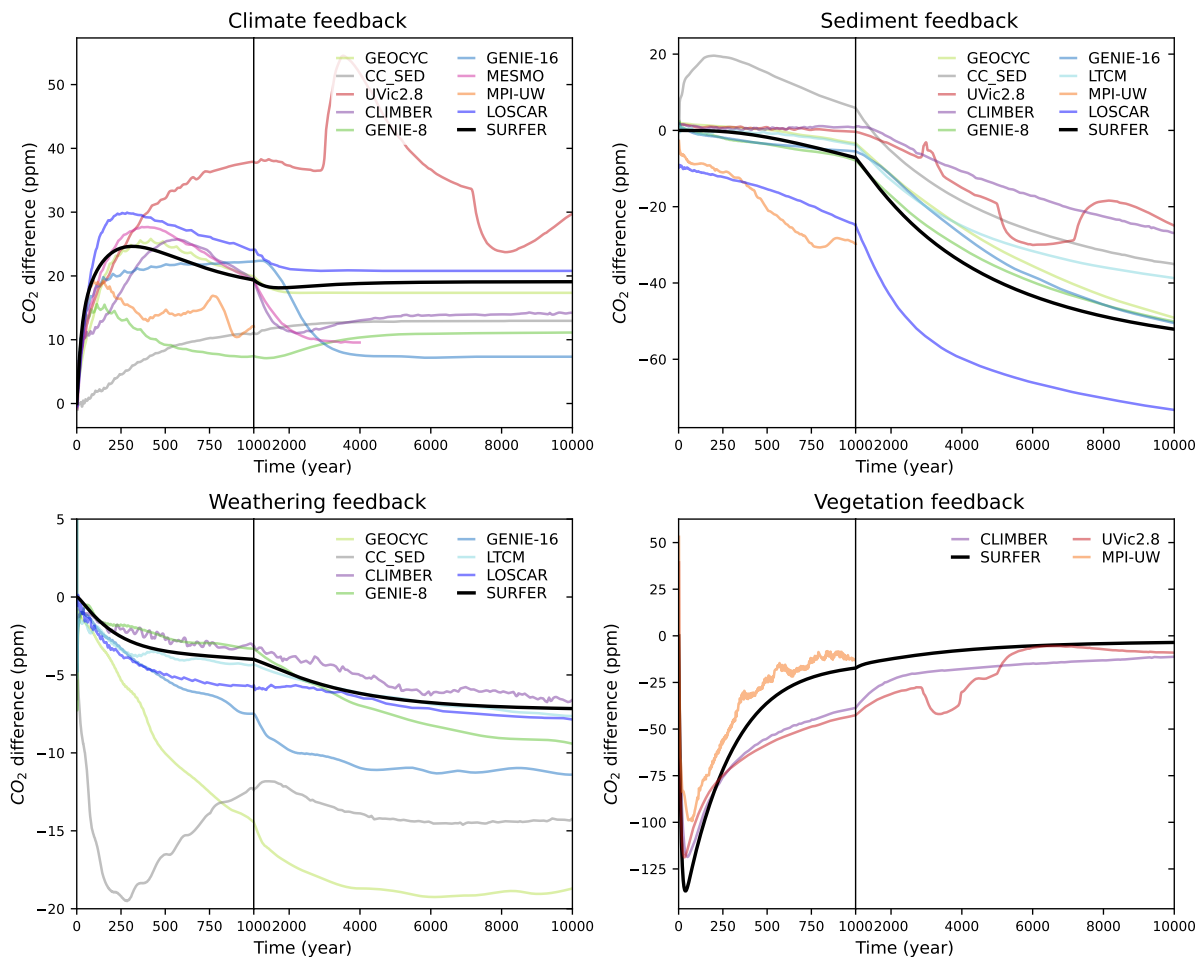
Figure 11. Impacts of the climate, sediments, weathering, and vegetation feedbacks on the atmospheric CO_2 concentration, after a 1000 PgC emission pulse. Here, a feedback is defined as the difference in CO_2 concentration resulting from the addition of the associated process.
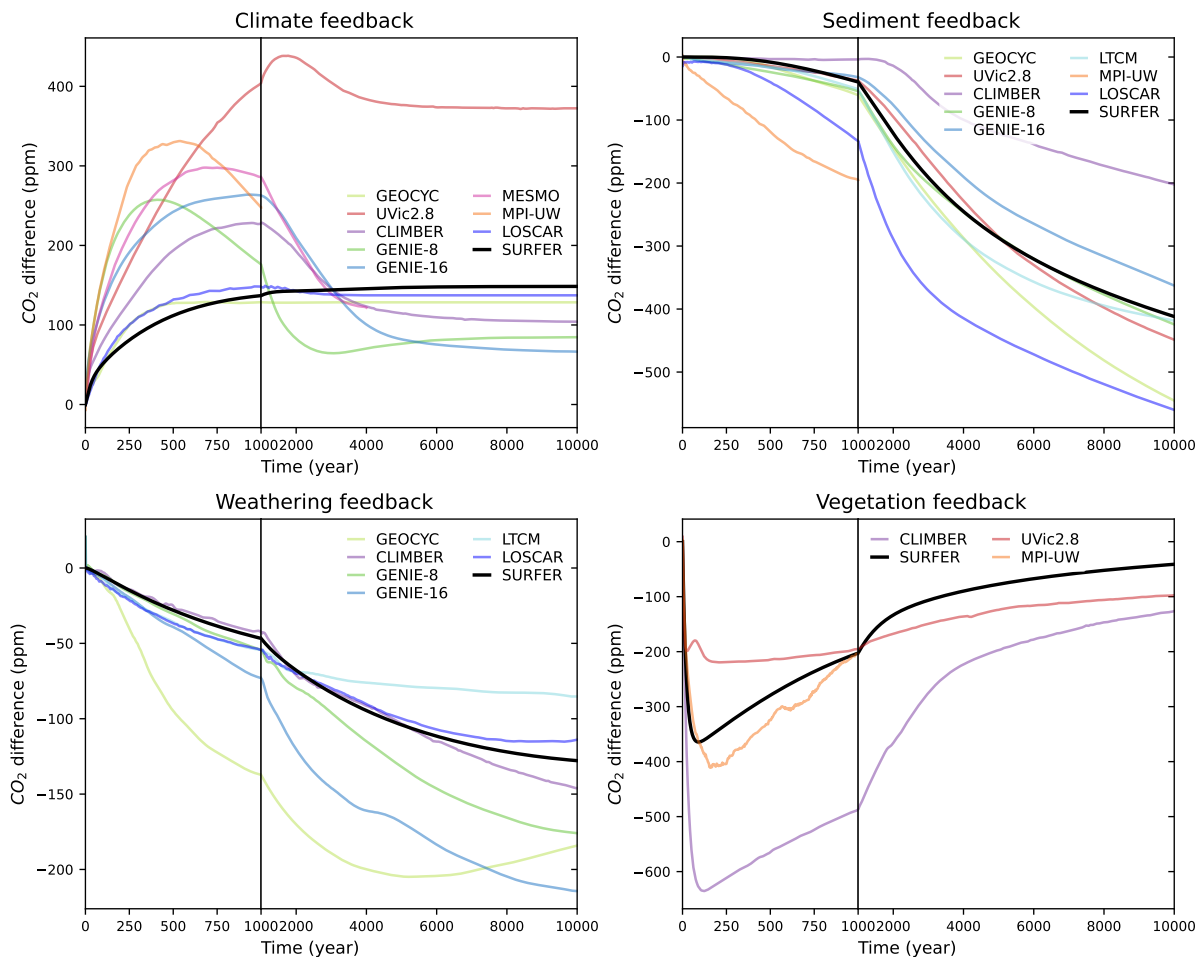
Figure 12. Impacts of the climate, sediments, weathering, and vegetation feedbacks on the atmospheric CO_2 concentration, after a 5000 PgC emission pulse. Here, a feedback is defined as the difference in CO_2 concentration resulting from the addition of the associated process.
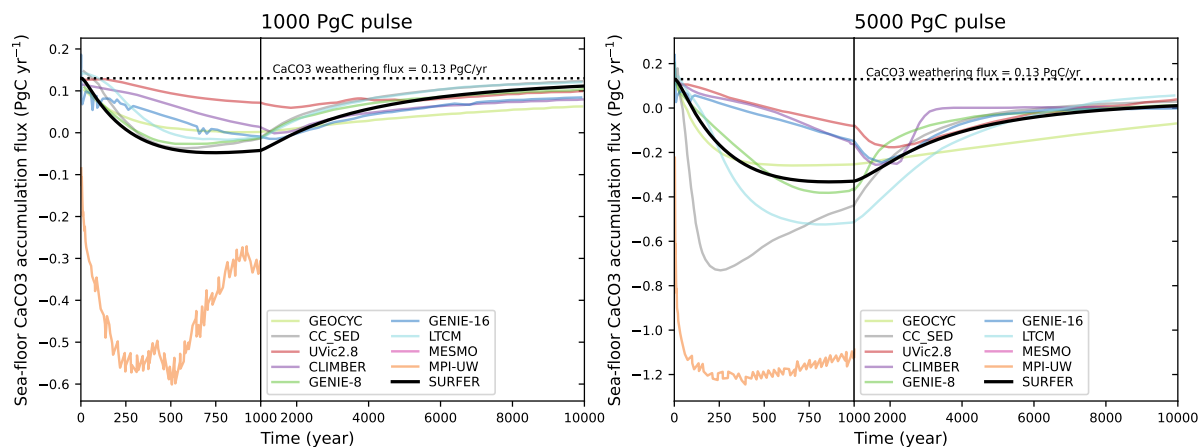
Figure 13. CaCO$_3$ accumulation fluxes in sediments for the different models. Negative values indicate net dissolution of CaCO$_3$.
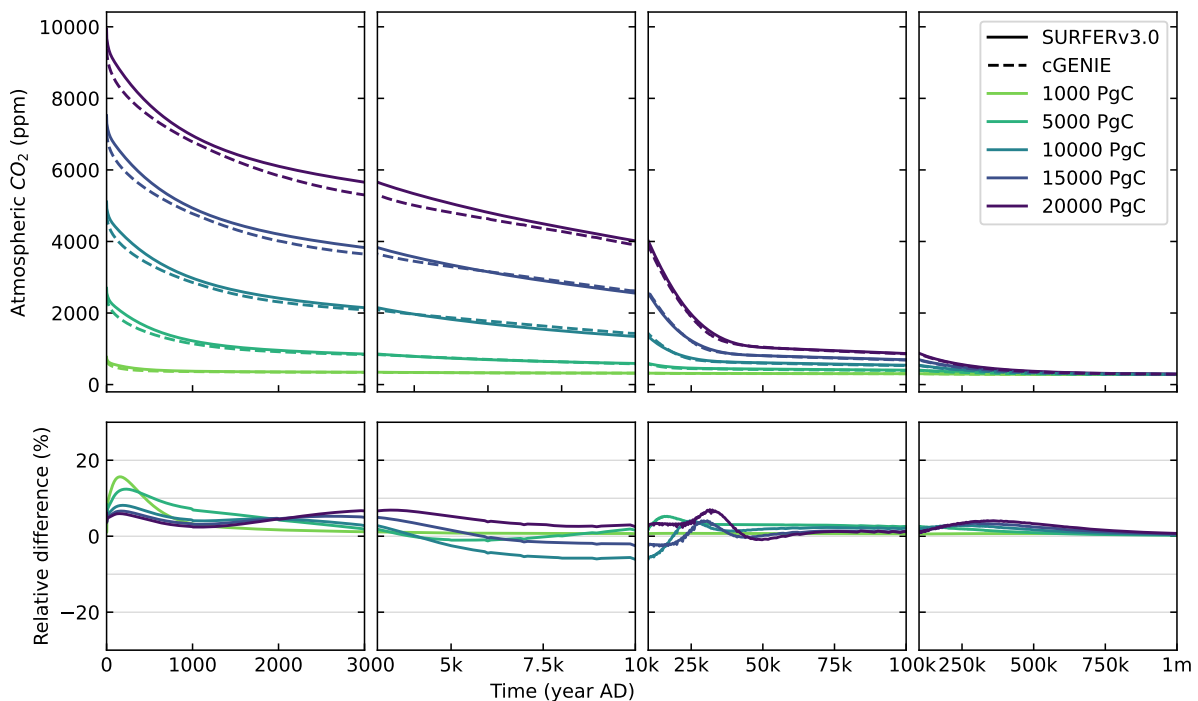
Figure 14. Atmospheric CO$_2$ concentrations simulated by cGENIE and SURFER v3.0 after emissions pulses of different sizes. The bottom plot shows the relative difference between SURFER v3.0 and cGENIE.
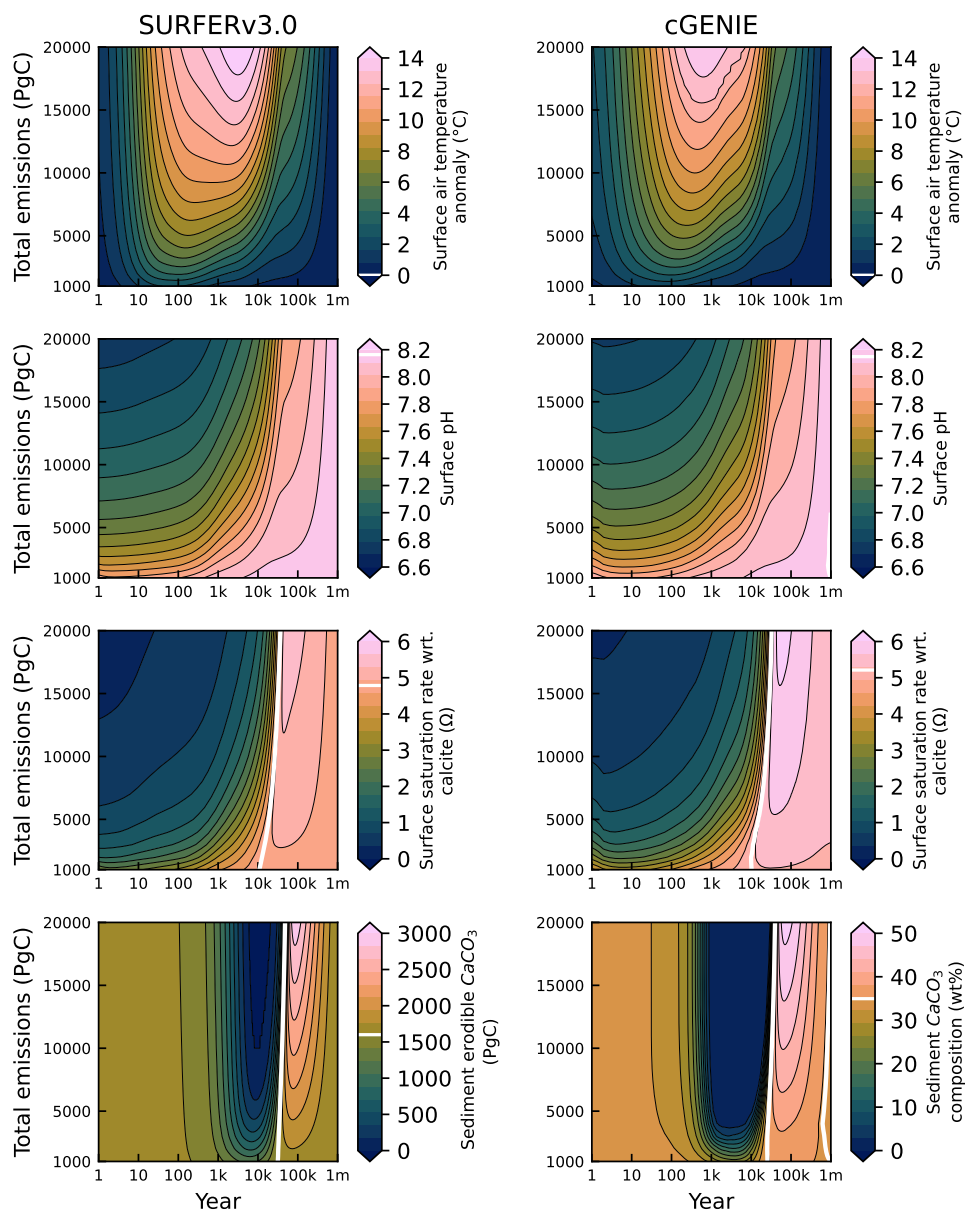
Figure 15. Global mean temperature anomaly, surface ocean pH, surface ocean saturation state with respect to calcite, and $CaCO_3$ sediments content in SURFER v3.0 and cGENIE after emissions pulses ranging from 1000 PgC to 20000 PgC. White lines indicate preindustrial values used in each model. Note : SURFER v3.0 and cGENIE use different units for the $CaCO_3$ sediments content. SURFER uses the total erodible $CaCO_3$ mass, while cGENIE uses the mean dry weight fraction (mass of $CaCO_3$ divided by the mass of $CaCO_3$ and non erodible material in sediments). Although these two quantities are strongly correlated, they do not necessarily depend linearly on one another, complicating direct comparisons.
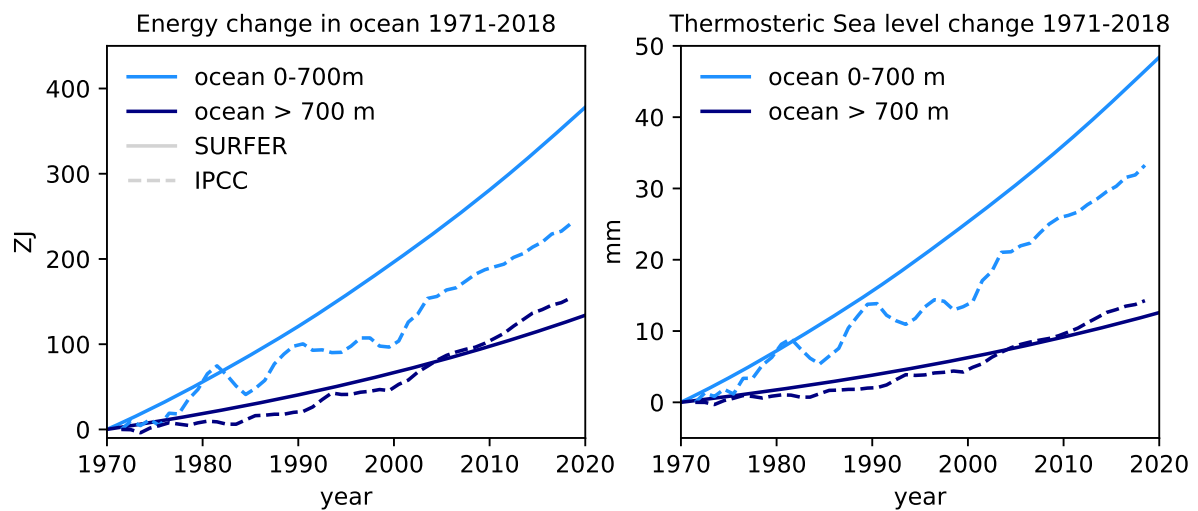
Figure 16. Ocean heat content and thermosteric sea level changes between the years 1971 and 2018 as estimated by the IPCC (Fox-Kemper et al., 2021), and simulated by SURFER v3.0.
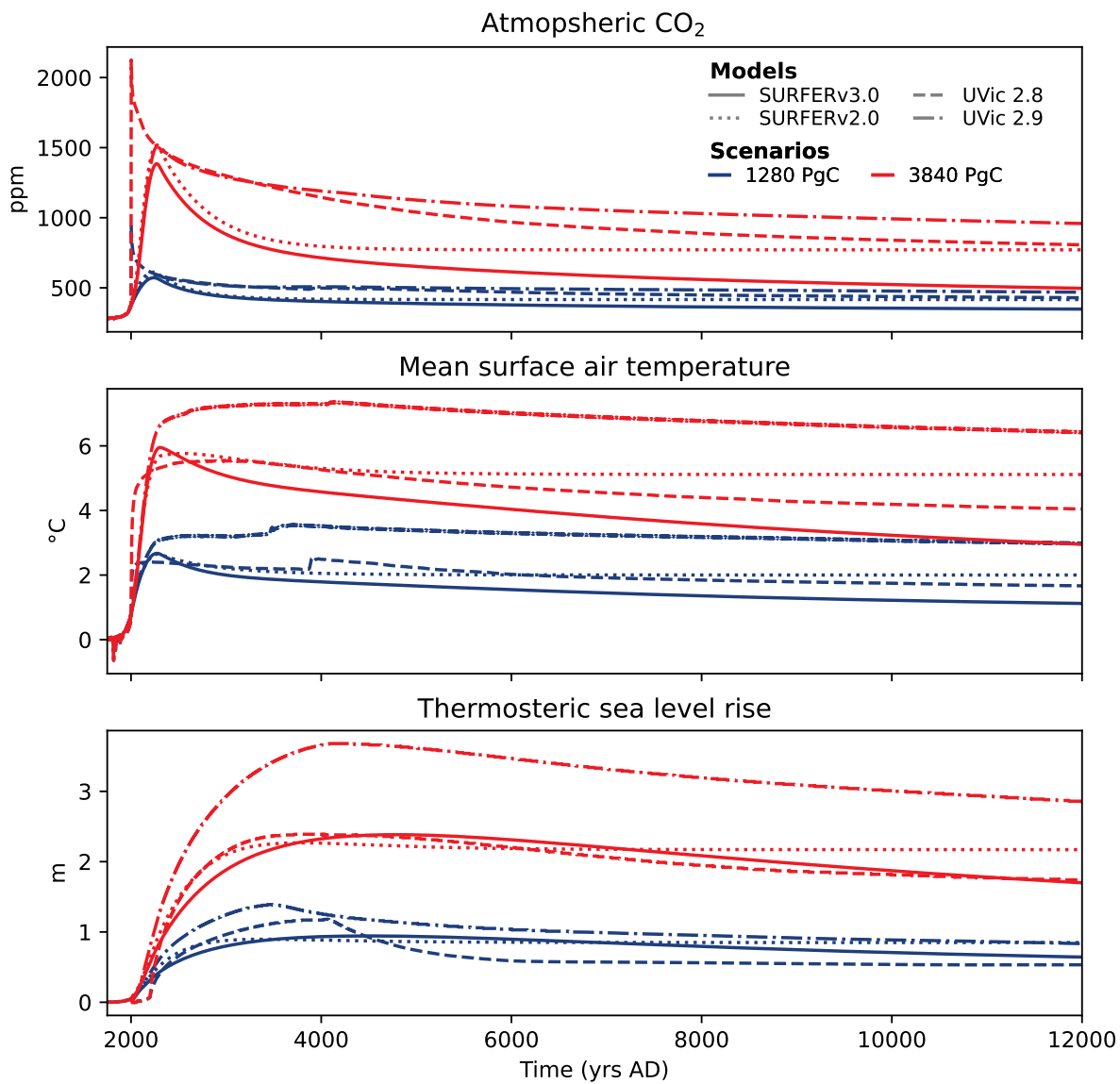
Figure 17. Atmospheric CO_2, surface temperature, and thermosteric sea level rise simulated by SURFER v3.0, SURFER v2.0, and two versions of the UVic model of intermediate complexity for two emission scenrarios : 1280 PgC (blue) and 3840 PgC (red).
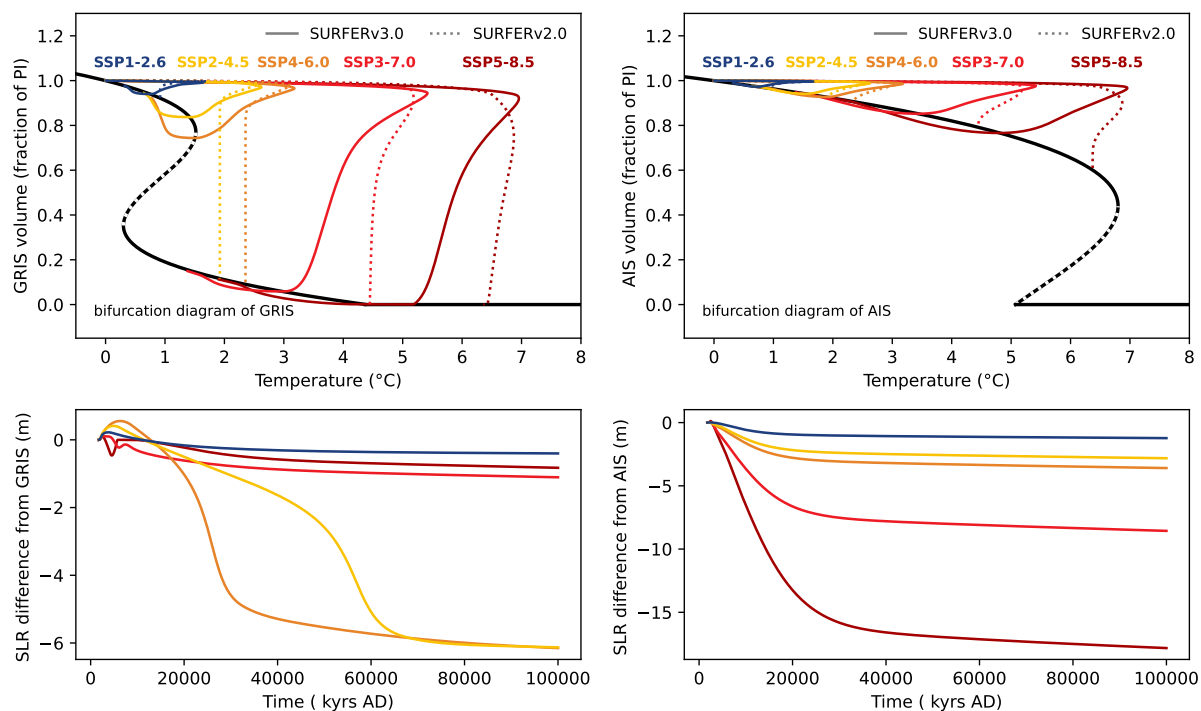
Figure 18. Comparison of Greenland and Antarctic sea level rise contributions in SURFER v3.0 and SURFER v2.0 for SSP emission scenarios. Top plots: Volume fractions of Greenland and Antarctica ice sheets as a function of temperature increase. Equilibrium values are shown in black, with stable equilibria represented by solid lines and unstable equilibria by dashed lines. Bottom plots: difference in sea level rise contributions from Greenland and Antarctica in SURFER v3.0 and SURFER v2.0. Negatives values indicate a reduced sea level rise contribution in SURFER v3.0 compared to SURFER v2.0.

Appendix A: Emission scenarios

Historical and SSP runs (Figures 3-8,16, 18, D1-D8)

For CO_2 emissions up to 1989 (included), we use the data from the Global Carbon Budget (Friedlingstein et al., 2022). Fossil emissions start in 1750 and we include the cement carbonation sink in them. Land-use emissions are only provided from the year 1850 and so we assume that they have grown linearly from zero since 1750. This adds around 33 PgC of emissions compared to a scenario where land-use emissions are considered zero before 1850.

For CH_4 emissions up to 1989 (included), we use the data from Jones et al. (2023). Both fossil and land-use emissions start in 1830 so, similarly to the CO_2 land-use emissions, we assume that they increased linearly from 0 since 1750. This adds a total of $\sim$1147 $MtCH_4$ of emissions compared to a scenario where land-use and fossil CH_4 emissions are considered zero before 1830.

For all emissions (CO_2 and CH_4, fossil and land-use) from 1990 to 2100, we use the values provided in the SSP database (https://tntcat.iiasa.ac.at/SspDb/dsd, Riahi et al. (2017); Gidden et al. (2019)). All SSP scenarios have the same emissions between 1990 and 2015, so we perform our historical runs (1750-2014) with the values from any SSP scenarios. The CO_2 and CH_4 emissions provided in 1990 by Friedlingstein et al. (2022) and Jones et al. (2023) are not equal to the values provided in 1990 in the SSP database, which causes small jumps in our emissions. For emissions between 2100 and 2300, we use the SSP extensions as described in Meinshausen et al. (2020). Before the year 1750, after 2300, all anthropogenic emissions are set to zero.

Pulse experiments (Figures 9-15)

For these experiments, the model is started with an additional amount of carbon x in the atmospheric reservoir, depending on the emission pulse : $M_A(t_{PI}) = 580.3 + x$ PgC. No other emissions are used.

Others (Figure 17)

For the experiments in section 4.1 where we compare SURFER to UVic, we use the CO_2 emissions provided in the supplementary material of Clark et al. (2016), while CH_4 emissions are set to zero.

Appendix B: Temperature and pressure dependance of solubility and dissociation constants

For the temperature (and salinity) dependence of K_0, K_1, K_2, K_b, K_w, and $K_{sp}^{CaCO_3}$, we use the equations from Sarmiento and Gruber (2006), and originally from Weiss (1974); Mehrbach et al. (1973); Dickson and Millero (1987); Millero (1995);

Dickson (1990); Mucci (1983):

$$\ln K_0 = -60.2409 + 93.4517\left(\frac{100}{T}\right) + 23.3585 \cdot \ln\left(\frac{T}{100}\right)$$
$$+ S\left(0.023517 - 0.023656\left(\frac{T}{100}\right) + 0.0047036\left(\frac{T}{100}\right)^2\right), \tag{B1}$$

$$-\log K_1^0 = -62.008 + \frac{3670.7}{T} + 9.7944 \cdot \ln T$$
$$- 0.0118 \cdot S + 0.000116 \cdot S^2, \tag{B2}$$

$$-\log K_2^0 = +4.777 + \frac{1394.7}{T} - 0.0184 \cdot S + 0.000118 \cdot S^2, \tag{B3}$$

$$\ln K_b^0 = \frac{1}{T}\left(-8966.9 - 2890.53 \cdot S^{1/2} - 77.942 \cdot S + 1.728 \cdot S^{3/2} - 0.0996 \cdot S^2\right)$$
$$+ 148.0248 + 137.1942 \cdot S^{1/2} + 1.62142 \cdot S + 0.053105 \cdot S^{1/2}T$$
$$+ \ln T(-24.4344 - 25.085 \cdot S^{1/2} - 0.2474 \cdot S), \tag{B4}$$

$$\ln K_w^0 = 148.96502 + \frac{-13847.26}{T} - 23.6521 \cdot \ln T$$
$$S^{1/2}\left(-5.977 + \frac{118.67}{T} + 1.0495 \cdot \ln T\right) - 0.01615 \cdot S, \tag{B5}$$

$$\ln K_{sp}^{CaCO_3,0} = -395.8293 + \frac{6537.773}{T} + 71.595 \cdot \ln T - 0.17959 \cdot T$$
$$+ \left(-1.78938 + \frac{410.64}{T} + 0.0065453 \cdot T\right)S^{1/2}$$
$$- 0.17755 \cdot S + 0.0094979 \cdot S^{2/3}. \tag{B6}$$

Here, K_0, K_1^0, K_2^0, K_w^0, K_b^0, and $K_{sp}^{CaCO_3,0}$ are the values of the constants at atmospheric pressure, given in $\mathrm{mol\,(kg\,atm)^{-1}}$ for K_0, in $\mathrm{mol\,kg^{-1}}$ for K_1^0, K_2^0, K_b^0, and in $(\mathrm{mol\,kg^{-1}})^2$ for K_w^0 and $K_{sp}^{CaCO_3,0}$, T is the temperature in Kelvin and S is the salinity on the practical salinity scale. In SURFER, only temperature anomalies are computed, meaning that to compute the absolute temperature and then the dissociation constants, we need to provide an initial temperature for each layer. This is done in section 2.4.2.

The pressure (depth) dependence for K_1, K_2, K_w, K_b, and $K_{sp}^{CaCO_3}$ is from Millero (1995),

$$\ln\left(K_i^p/K_i^0\right) = -\frac{\Delta V_i}{RT}P + \frac{0.5\Delta K_i}{RT}P^2, \tag{B7}$$

where K_i^p is the value of the dissociation constant at pressure P (in bar), K_i^0 is the value of the dissociation constant at atmospheric pressure (1.01325 bar or 101325 Pa), T is the temperature in Kelvin and R is the gas constant in $\mathrm{bar\,cm^3\,mol^{-1}\,K^{-1}}$ (10 times the value in $\mathrm{J\,mol^{-1}\,K^{-1}}$). The quantities ΔV_i and ΔK_i are changes in molal volume and compressibility and are estimated following :

$$\Delta V_i = a_{0,i} + a_{1,i}(T - 273.15) + a_{2,i}(T - 273.15)^2, \tag{B8}$$
$$1000\Delta K_i = b_{0,i} + b_{1,i}(T - 273.15). \tag{B9}$$

Table B1. Parametrisation for the effect of pressure on dissociation constants ; coefficients for equations B8 and B9. The values are taken from Millero (1995). We have flipped the signs of a_1 and a_2 for K_b, and b_1 for K_{sp}^{CaCO3} to match the values given in Millero (1979).

	a_0	a_1	a_2	b_0	b_1
K_1	-25.50	0.1271	0	-3.08	0.0877
K_2	-15.82	-0.0219	0	1.13	-0.1475
K_b	-29.48	0.1622	-0.002608	-2.84	0
K_w	-25.60	0.2324	-0.0036246	-5.13	0.0794
K_{sp}^{CaCO3}	-48.76	-0.5304	0	-11.76	0.3692

Values for the coefficients are in table B1.

Hydrostatic balance provides the pressure at a given depth, thus, pressure (in bar) is given by $P = \rho g z / 100000$ where $\rho = 1026\ kg/m^3$ is sea water mean density, $g = 9.81\ \mathrm{kg\,m\,s^{-2}}$ is the gravitational acceleration and z is the depth (in m). For the computation of mean quantities in the different ocean levels U, I and D, we use the depths $z_U = 75$ m, $z_I = 400$ m and $z_D = 2225$ m which corresponds to the mid-depth points of the layers.

Appendix C: Alkalinity and solving the carbonate system

In SURFER v2.0, we approximated alkalinity by carbonate alkalinity

$$\text{Alk} \approx \text{Alk}_C = \left[\text{HCO}_3^-\right] + 2\left[\text{CO}_3^{2-}\right] . \tag{C1}$$

To compute $[\text{H}^+]$ and the other carbonate species, we had to rewrite eq C1 as a function of the four known quantities DIC, Alk, T, and S, and the unknown quantity $[\text{H}^+]$. Using the definition of DIC (eq 11) and of the dissociation constants K_1 and K_2 (eq 17 and eq 18) we can express DIC as a function of $[\text{HCO}_3^-]$ and $[\text{H}^+]$:

$$\text{DIC} = \left(1 + \frac{K_2}{[\text{H}^+]} + \frac{[\text{H}^+]}{K_1}\right)\left[\text{HCO}_3^-\right], \tag{C2}$$

or equivalently, we can express $\left[\text{HCO}_3^-\right]$ as a function of DIC and $[\text{H}^+]$

$$\left[\text{HCO}_3^-\right] = \frac{\text{DIC} \cdot K_1 [\text{H}^+]}{K_1 K_2 + K_1 [\text{H}^+] + [\text{H}^+]^2} . \tag{C3}$$

Using equation 18, we can then express $[\text{CO}_3^{2-}]$ as a function of DIC and $[\text{H}^+]$

$$[\text{CO}_3^{2-}] = \frac{[\text{HCO}_3^-] K_2}{[\text{H}^+]}$$
$$= \frac{\text{DIC} \cdot K_1 K_2}{K_1 K_2 + K_1 [\text{H}^+] + [\text{H}^+]^2} . \tag{C4}$$

Inserting eqs C3 and C4 in C1, we get

$$\text{Alk}_\text{C} = \text{DIC} \cdot \frac{K_1[\text{H}^+] + K_1 K_2}{K_1 K_2 + K_1[\text{H}^+] + [\text{H}^+]^2} \,, \tag{C5}$$

which we can solve for $[\text{H}^+]$, given Alk, DIC and the dissociations constants K_1 and K_2 (which depend on T and S). To do so, we write eq C5 as a degree 2 polynomial equation

$$P_\text{C}([\text{H}^+]) \equiv [\text{H}^+]^2 + a_1[\text{H}^+] + a_0 \,, \tag{C6}$$

with

$$a_1 = K_1 \left(1 - \frac{\text{DIC}}{\text{Alk}} \right) \,, \tag{C7}$$

$$a_0 = K_1 K_2 \left(1 - \frac{2 \cdot \text{DIC}}{\text{Alk}} \right) \,. \tag{C8}$$

The positive root is given by

$$[\text{H}^+] = \frac{K_1}{2 \cdot \text{Alk}} \left(\sqrt{(\text{DIC} - \text{Alk})^2 - 4 \frac{K_2}{K_1} \text{Alk} \cdot (\text{Alk} - 2 \cdot \text{DIC})} + (\text{DIC} - \text{Alk}) \right) \,. \tag{C9}$$

Then, $[\text{HCO}_3^-]$ can be computed from equation C3, $[\text{CO}_3^{2-}]$ can be computed from equation C4, and finally, $[\text{H}_2\text{CO}_3^*]$ can be computed from equation 17.

In SURFER v3.0, we approximate alkalinity by the carbonate, borate and water self-ionisation alkalinity

$$\text{Alk} \approx \text{Alk}_\text{CBW} = \left[\text{HCO}_3^-\right] + 2\left[\text{CO}_3^{2-}\right] + \left[\text{OH}^-\right] - \left[\text{H}^+\right] + \left[\text{B(OH)}_4^-\right] \tag{C10}$$

As before, to compute $[\text{H}^+]$ and the other carbonate species, we have to rewrite eq C10 as a function of the 4 know quantities DIC, Alk, T, and S and the unknown quantity $[\text{H}^+]$. We already know how express $[\text{HCO}_3^-]$ and $[\text{CO}_3^{2-}]$ as a function of DIC and $[\text{H}^+]$ (eqs C3 and C4). Equation 19 further gives us

$$\left[\text{OH}^-\right] = \frac{K_\text{w}}{[\text{H}^+]} \,, \tag{C11}$$

and we can use equations 20 and 21 to obtain

$$\left[\text{B(OH)}_4^-\right] = \frac{c_\text{b} \cdot S \cdot K_\text{b}}{[\text{H}^+] + K_\text{b}} \,. \tag{C12}$$

Inserting these results in equation C10, we get

$$\text{Alk} \approx \text{Alk}_{CBW} = \text{DIC} \cdot \frac{K_1[\text{H}^+] + K_1 K_2}{K_1 K_2 + K_1[\text{H}^+] + [\text{H}^+]^2} + \frac{K_\text{w}}{[\text{H}^+]} - \left[\text{H}^+\right] + \frac{c_\text{b} \cdot S \cdot K_\text{b}}{[\text{H}^+] + K_\text{b}} \tag{C13}$$

which we can solve for $[\text{H}^+]$, given Alk, DIC and the dissociations constants K_1, K_2, K_w and K_b (which depend on T and S). To do this, we follow Munhoven (2013) and we write eq C13 as a polynomial equation that is now of degree 5

$$P_\text{CBW}([\text{H}^+]) \equiv [\text{H}^+]^5 + q_4[\text{H}^+]^4 + q_3[\text{H}^+]^3 + q_2[\text{H}^+]^2 + q_1[\text{H}^+] + q_0 \,, \tag{C14}$$

with

$$q_4 = \text{Alk} + K_1 + K_b, \tag{C15}$$

$$q_3 = (\text{Alk} - \text{DIC} + K_b)K_1 + (\text{Alk} - c_b \cdot S)K_b + K_1K_2 - K_w, \tag{C16}$$

$$q_2 = (\text{Alk} - 2 \cdot \text{DIC} + K_b)K_1K_2 + (\text{Alk} - \text{DIC} - c_b \cdot S)K_1K_b - K_1K_w - K_bK_w, \tag{C17}$$

$$q_1 = (\text{Alk} - 2 \cdot \text{DIC} - c_b \cdot S)K_1K_2K_b - K_1K_2K_w - K_1K_bK_w, \tag{C18}$$

$$q_0 = -K_1K_2K_bK_w. \tag{C19}$$

We solve this equation using the Newton-Raphson method. To ensure quick convergence, we need a good initial guess that is not too far from the real solution. We adopt the following procedure from Munhoven (2013) and Humphreys et al. (2022). We define the following coefficients

$$c_2 = K_b\left(1 - \frac{c_b \cdot S}{\text{Alk}}\right) + K_1\left(1 - \frac{\text{DIC}}{\text{Alk}}\right), \tag{C20}$$

$$c_1 = K_1K_b\left(1 - \frac{c_b \cdot S}{\text{Alk}} - \frac{\text{DIC}}{\text{Alk}}\right) + K_1K_2\left(1 - 2\frac{\text{DIC}}{\text{Alk}}\right), \tag{C21}$$

$$c_0 = K_1K_2K_b\left(1 - \frac{2 \cdot \text{DIC} + c_b \cdot S}{\text{Alk}}\right), \tag{C22}$$

from which we construct the quantities

$$H_{\min} = \frac{-c_2 + \sqrt{c_2^2 - 3c_1}}{3}, \tag{C23}$$

and

$$H_0 = H_{\min} + \sqrt{-\frac{H_{\min}^3 + c_2 H_{\min}^2 + c_1 H_{\min} + c_0}{\sqrt{c_2^2 - 3c_1}}}. \tag{C24}$$

The initial guess for the Newton-Raphson method is taken as

$$[\text{H}^+]_0 = \begin{cases} 10^{-3} & \text{if Alk} \leq 0, \\ H_0 & \text{if } 0 < \text{Alk} < 2 \cdot \text{DIC} + c_b \cdot S \text{ and } c_2^2 - 3c_1 > 0, \\ 10^{-7} & \text{if } 0 < \text{Alk} < 2 \cdot \text{DIC} + c_b \cdot S \text{ and } c_2^2 - 3c_1 < 0, \\ 10^{-10} & \text{if Alk} \geq 2 \cdot \text{DIC} + c_b \cdot S. \end{cases} \tag{C25}$$

The rationale behind this choice is given in Munhoven (2013) and Humphreys et al. (2022). With it, we only need 5 Newton-Raphson iterations to obtain an accurate value for $[\text{H}^+]$ and pH, which is defined as

$$\text{pH} = -\log_{10}([\text{H}^+]). \tag{C26}$$

Once $[\text{H}^+]$ is computed, $[\text{HCO}_3^-]$ and $[\text{CO}_3^{2-}]$ can be computed from equations C3 and C4, $[\text{H}_2\text{CO}_3{}^*]$ can be computed from equation 17, $[\text{OH}^-]$ can be computed from equation C11, and $[\text{B(OH)}_4^-]$ can be computed from equation C12. Equation

C10 is solved following this procedure at every time step of the numerical integration of the model. This is because we need $[H^+]_U$ for the computation of B_U in the atmosphere to upper ocean carbon flux $F_{A \to U}$ (see equations 27 and 28), and we need $[CO_3^{2-}]_D$ for the computation of the dissolution flux F_{diss} (see eq 48). This is also the procedure used to obtain climatologies (and vertical profiles) of the carbonate species from the GLODAP climatologies of DIC, Alk, temperature and salinity (see Figure 3). In this case, we computed the carbonate species at each ocean point where DIC, Alk, temperature and salinity were all given.

To determine the initial condition for the dissolved inorganic carbon mass in the upper layer $M_U(t_{PI})$, we need to compute $DIC_U(t_{PI})$ as a function of $Alk_U(t_{PI})$, $T_U(t_{PI})$, S_U, and $[H_2CO_3^*]_U(t_{PI})$, which is fixed by equilibrium conditions (eq 108). Now DIC is an unknown and we can't use the procedure described above. Instead, we write Alk as a function of $[H_2CO_3^*]$ and $[H^+]$ (and the dissociation). Using equations 17 and 18 we get

$$[HCO_3^-] = \frac{K_1[H_2CO_3^*]}{[H^+]}, \tag{C27}$$

$$[CO_3^{2-}] = \frac{K_1 K_2 [H_2CO_3^*]}{[H^+]^2}, \tag{C28}$$

and thus

$$Alk \approx Alk_{CBW} = \frac{K_1[H_2CO_3^*]}{[H^+]} + 2\frac{K_1 K_2 [H_2CO_3^*]}{[H^+]^2} + \frac{K_w}{[H^+]} - [H^+] + \frac{c_b \cdot S \cdot K_b}{[H^+] + K_b}. \tag{C29}$$

This equation can be solved numerically for $[H^+]$ using any algorithm. The speed of the algorithm is not of great importance here since we only perform the computation for the setting of the initial conditions, and not at each time step of the numerical integration. Once $[H^+]$ is obtained, $[HCO_3^-]$ and $[CO_3^{2-}]$ are recovered with equations 17 and 18 and DIC can then be computed as the sum of $[HCO_3^-]$, $[CO_3^{2-}]$ and $[H_2CO_3^*]$.

Appendix D: Sensitivity analysis

We present here a sensitivity analysis of the model in response to changes in specific parameters. While the primary goal is to assess how these sometimes arbitrary parameter choices affect model behaviour, an added benefit is the ability to investigate the timescales on which the associated processes are significant.

We first test how atmospheric CO_2 levels simulated for the SSP3-7.0 scenario from 1750 AD to 1 000 000 AD respond to changes in 20 parameters associated with the carbon cycle component of SURFER v3.0 (all parameters from the first part of table 2, except τ_{CH_4}). Most parameters are adjusted one at a time, with interdependent parameters and $M_U(t_{PI})$ being modified accordingly to obey the preindustrial equilibrium condition (see second part of table 2). Each parameter is varied within a range of 0.25 to 1.75 times its default value. Note that these ranges do not necessarily reflect physically plausible values.

Changing $k_{A \to U}$ in the range described above has a negligible impact on the atmospheric CO_2 draw-down (figure D1). This is because regardless of the values set for $k_{A \to U}$, the transfer rate of CO_2 between the atmosphere and the ocean surface layer is very fast compared to the subsequent transport of dissolved carbon at depth, which therefore is the real limiting factor of for oceanic CO_2 uptake. Indeed, we observe that increasing $k_{U \to I}$ or $k_{I \to D}$ leads to an increased CO_2 uptake for up to 100
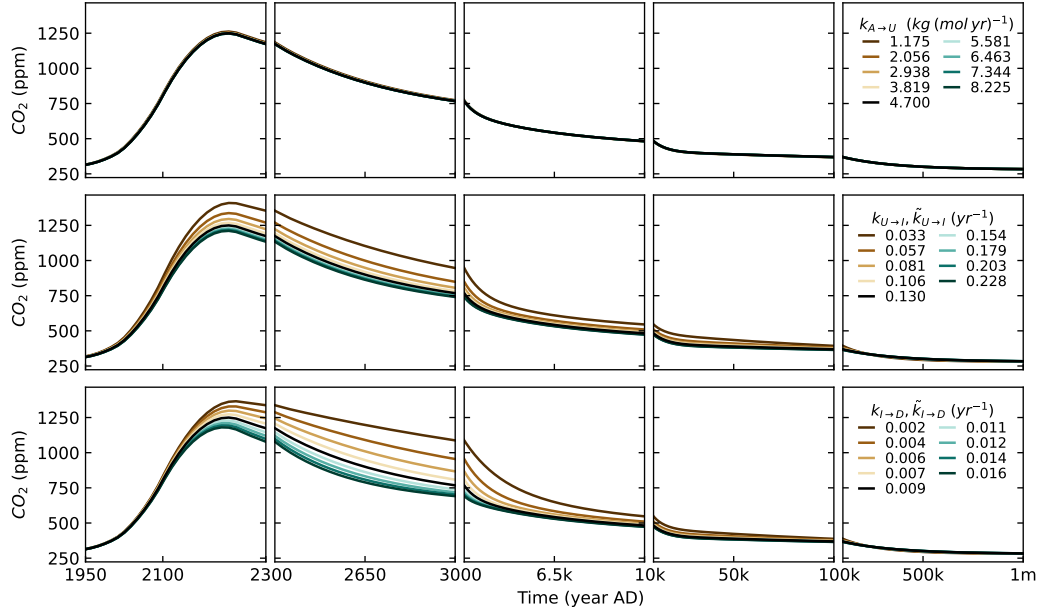
Figure D1. Atmospheric CO_2 concentration simulated by SURFER v3.0 under the SSP3-7.0 scenario for different values of $k_{A \to U}$, $k_{U \to I}$, and $k_{I \to D}$ (and $\tilde{k}_{U \to I}$, and $\tilde{k}_{I \to D}$). Black lines indicate the atmospheric CO_2 concentration simulated for the default parameter values, as described in section 2.4.1.

kyr. After that, the ocean, atmosphere and sediments reservoir are in equilibrium, and atmospheric CO_2 is regulated by the imbalance between volcanism and weathering. Changing $k_{I \to D}$ only has a very little effect before 2100 AD, reflecting the longer time scales associated with the deeper ocean. Note that we have varied $\tilde{k}_{U \to I}$ and $\tilde{k}_{I \to D}$ simultaneously as $k_{U \to I}$ and $k_{I \to D}$ because these parameters are all linked to the implicit ocean circulation.

Figure D2 shows the sensitivity of atmospheric CO_2 to changes in parameters associated with the carbonate and soft-tissue pumps. Overall, varying these parameters has a small or negligible impact. This is due to the preindustrial equilibrium condition that we impose, which creates a compensating effect. For example, if we have stronger pumps initially, we need stronger upwelling fluxes at equilibrium and so higher $k_{I \to U}$ and $k_{D \to I}$ (and $\tilde{k}_{I \to U}$ and $\tilde{k}_{D \to I}$). This leads to weaker $F^{\text{res}}_{U \to I}$ and $F^{\text{res}}_{I \to D}$ (and $\tilde{F}^{\text{res}}_{U \to I}$ and $\tilde{F}^{\text{res}}_{U \to I}$) fluxes which mostly compensates the effects of stronger pumps in transient runs (see equations 43-46). This compensation effect is not exact and we can observe a small impact for changes in P^{org} and ϕ^{org}_I. In comparison, the impact for changes in P^{CaCO_3}, $\phi^{\text{CaCO}_3}_I$, and $\sigma_{Alk:\text{DIC}}$ are almost non-existent because these parameters are associated to smaller DIC and alkalinity fluxes. Changing $\phi^{\text{CaCO}_3}_D$ has no impact on model results because we keep P^{CaCO_3} constant. In this case the terms in F_{acc} involving $\phi^{\text{CaCO}_3}_D$ cancel out (see equations 35, 48, and 101). Still, we have kept the parameter to facilitate further model updates. Increasing P^{org} implies that we need stronger upwelling fluxes to respect the

preindustrial condition, and so overall the ocean is better ventilated and it is harder to store carbon in the deep ocean, slowing down atmospheric CO_2 uptake. Increasing $\phi_{\text{I}}^{\text{org}}$ has the opposite effect: it leads to a weaker soft-tissue pump, which implies weaker upwelling fluxes and thus a faster CO_2 uptake.

Figures D3 and D4 show the sensitivity of atmospheric CO_2 to changes in parameters associated with the dissolution of $CaCO_3$ sediments and with weathering fluxes. Atmospheric CO_2 is sensitive to changes in α_{diss} and γ_{diss}, but barely to changes in β_{diss}, meaning that the deep CO_3^{2-} conentration rather than the mass of erodible $CaCO_3$ sediments, M_{S}, is the dominant driver of dissolution in our parametrisation. With the biggest changes in atmospheric CO_2 concentration observed between 3000 yrs AD and 50 kyr AD, these experiments showcase nicely the timescales associated with sediment processes. Changes in $F_{\text{CaCO}_3,0}$ and k_{Ca}, associated to carbonate weathering have an negligible impact on CO_2 levels compared to changes in $F_{\text{CaSiO}_3,0}$ and k_{T}, associated to silicate weathering. This results from silicate weathering rather than carbonate weathering being the process that is ultimately responsible for the draw-down of excess atmospheric CO_2, at least in our model. We observe that a larger initial silicate weathering flux ($F_{\text{CaSiO}_3,0}$), or a larger response of silicate weathering to warming (k_{T}) leads to a faster uptake of CO_2, mostly noticeable after 100 kyr .

Focusing on vegetation in Figure D5, we observe that the impact of varying $k_{\text{A}\rightarrow\text{L}}$ is small and limited to years before 2300 AD. This is because the exchanges of carbon between the atmosphere and the land are relatively fast and so the limiting factor to land uptake is rather the amount of carbon that land can store, which is controlled by β_{L}. A larger β_{L} means that more carbon can be stored in the land reservoir for a given atmospheric concentration, thus increasing the land sink. Together with $k_{\text{U}\rightarrow\text{I}}$ and $k_{\text{I}\rightarrow\text{D}}$ (and $\tilde{k}_{\text{U}\rightarrow\text{I}}$ and $\tilde{k}_{\text{I}\rightarrow\text{D}}$), β_{L} is the parameter that has the biggest influence on CO_2 uptake up to the year 6500AD, showing that the fertilisation effect and oceanic invasion of CO_2 are the main processes driving atmospheric CO_2 draw-down on these timescales in SURFER v3.0.

We also test how simulated atmospheric CO_2 levels, temperatures and sea level rise respond to changes in $\gamma_{\text{U}\rightarrow\text{I}}$, $\gamma_{\text{I}\rightarrow\text{D}}$, and β, which are parameters linked to the climate module of SURFER v3.0. The experimental setup is the same as the one described above.

Figures D6 and D7 show the sensitivity analysis for $\gamma_{\text{U}\rightarrow\text{I}}$ and $\gamma_{\text{I}\rightarrow\text{D}}$. Increasing $\gamma_{\text{U}\rightarrow\text{I}}$ decreases the heat accumulation and thus temperatures in the surface layer, but increases temperature in the intermediate and deep layers. On the other hand, increasing $\gamma_{\text{I}\rightarrow\text{D}}$ decreases the heat accumulation and temperature in the surface and intermediate layers, but increases the temperature in the deep layer. For both parameters, an increase leads to an overall increase in thermosteric sea level rise because the deep layer dominates the thermal expansion. Although both parameters impact surface temperature, they have almost no impact on atmospheric CO_2 because SURFER v3.0 has a very weak carbon-climate feedback (see discussion, section 5). We also observe little to no impact on temperatures after 10 000 kyr , suggesting that by that time, the ocean has reached thermal equilibrium.

In Figure D8, we investigate SURFER v3.0 's response to changes in β, the climate feedback parameter. Decreasing β while keeping $F_{2\times}$ constant increases the equilibrium climate sensitivity. In this case, we vary β in the range 0.780-1.671 $\text{W m}^{-2}\,^{\circ}\text{C}^{-1}$ giving an ECS range of 2.33-5 °C which is within the estimated very likely 2-5°C range given by the IPCC (Smith et al., 2021). Lower values for β, and thus higher values of climate sensitivity naturally lead to more warming and

consequently a higher sea level rise. Big differences in projected sea level rise after 10 kyr AD, even for close β values, are
the consequence of tipping the Greenland ice sheet. As for $\gamma_{U \to I}$, and $\gamma_{I \to D}$, changes in β do not impact CO_2 levels that much since the total carbon-climate feedback in SURFER v3.0 is weak. For higher values of climate sensitivity, the positive climate-carbon feedback resulting from the temperature-dependent solubility and dissociation constants leads to higher CO_2 levels up to around 10 kyr AD. Conversely, the negative carbon-climate feedback from silicate weathering, acting on longer timescales, results in lower CO_2 values after 10 kyr AD, and especially after 100 000 kyr.

References

Alley, R. B., Anandakrishnan, S., Christianson, K., Horgan, H. J., Muto, A., Parizek, B. R., Pollard, D., and Walker, R. T.: Oceanic Forcing of Ice-Sheet Retreat: West Antarctica and More, Annual Review of Earth and Planetary Sciences, 43, 207–231, https://doi.org/10.1146/annurev-earth-060614-105344, publisher: Annual Reviews, 2015.

Andersson, A. J. and Mackenzie, F. T.: Shallow-water oceans: a source or sink of atmospheric CO2?, Frontiers in Ecology and the Environment, 2, 348–353, https://doi.org/10.1890/1540-9295(2004)002[0348:SOASOS]2.0.CO;2, _eprint: https://onlinelibrary.wiley.com/doi/pdf/10.1890/1540-9295%282004%29002%5B0348%3ASOASOS%5D2.0.CO%3B2, 2004.

Archer, D.: The Global Carbon Cycle, Princeton University Press, ISBN 978-0-691-14414-6, https://doi.org/10.2307/j.ctvcm4hx8, 2010.

Archer, D., Kheshgi, H., and Maier-Reimer, E.: Multiple timescales for neutralization of fossil fuel CO$_2$, Geophysical Research Letters, 24, 405–408, https://doi.org/10.1029/97GL00168, 1997.

Archer, D., Kheshgi, H., and Maier-Reimer, E.: Dynamics of fossil fuel CO$_2$ neutralization by marine CaCO$_3$, Global Biogeochemical Cycles, 12, 259–276, https://doi.org/10.1029/98GB00744, 1998.

Archer, D., Eby, M., Brovkin, V., Ridgwell, A., Cao, L., Mikolajewicz, U., Caldeira, K., Matsumoto, K., Munhoven, G., Montenegro, A., and Tokos, K.: Atmospheric Lifetime of Fossil Fuel Carbon Dioxide, Annual Review of Earth and Planetary Sciences, 37, 117–134, https://doi.org/10.1146/annurev.earth.031208.100206, 2009.

Armstrong McKay, D., Staal, A., Abrams, J. F., Winkelmann, R., Sakschewski, B., Loriani, S., Fetzer, I., Cornell, S. E., Rockström, J., and Lenton, T. M.: Updated assessment suggests >1.5°C global warming could trigger multiple climate tipping points, preprint, Climatology (Global Change), https://doi.org/10.1002/essoar.10509769.1, 2021.

Armstrong McKay, D. I., Staal, A., Abrams, J. F., Winkelmann, R., Sakschewski, B., Loriani, S., Fetzer, I., Cornell, S. E., Rockström, J., and Lenton, T. M.: Exceeding 1.5°C global warming could trigger multiple climate tipping points, Science, 377, eabn7950, https://doi.org/10.1126/science.abn7950, 2022.

Barclay, R. S., McElwain, J. C., and Sageman, B. B.: Carbon sequestration activated by a volcanic CO2 pulse during Ocean Anoxic Event 2, Nature Geoscience, 3, 205–208, https://doi.org/10.1038/ngeo757, publisher: Nature Publishing Group, 2010.

Berner, R. A.: The Phanerozoic Carbon Cycle: CO2 and O2, Oxford University Press, Oxford, New York, ISBN 978-0-19-517333-8, 2004.

Berner, R. A., Lasaga, A. C., and Garrels, R. M.: The carbonate-silicate geochemical cycle and its effect on atmospheric carbon dioxide over the past 100 million years, American Journal of Science, 283, 641–683, https://doi.org/10.2475/ajs.283.7.641, publisher: American Journal of Science, 1983.

Brantley, S. L., Shaughnessy, A., Lebedeva, M. I., and Balashov, V. N.: How temperature-dependent silicate weathering acts as Earth's geological thermostat, Science, 379, 382–389, https://doi.org/10.1126/science.add2922, _eprint: https://www.science.org/doi/pdf/10.1126/science.add2922, 2023.

Breedam, J. V., Goelzer, H., and Huybrechts, P.: Semi-equilibrated global sea-level change projections for the next 10 000 years, 2020.

Brovkin, V., Brücher, T., Kleinen, T., Zaehle, S., Joos, F., Roth, R., Spahni, R., Schmitt, J., Fischer, H., Leuenberger, M., Stone, E. J., Ridgwell, A., Chappellaz, J., Kehrwald, N., Barbante, C., Blunier, T., and Dahl Jensen, D.: Comparative carbon cycle dynamics of the present and last interglacial, Quaternary Science Reviews, 137, 15–32, https://doi.org/10.1016/j.quascirev.2016.01.028, 2016.

Canadell, J., Monteiro, P., Costa, M., Cotrim da Cunha, L., Cox, P., Eliseev, A., Henson, S., Ishii, M., Jaccard, S., Koven, C., Lohila, A., Patra, P., Piao, S., Rogelj, J., Syampungani, S., Zaehle, S., and Zickfeld, K.: Global Carbon and other Biogeochemical Cycles and Feedbacks, in: Climate Change 2021: The Physical Science Basis. Contribution of Working Group I to the Sixth Assessment Re-

port of the Intergovernmental Panel on Climate Change, edited by Masson-Delmotte, V., Zhai, P., Pirani, A., Connors, S., Péan, C., Berger, S., Caud, N., Chen, Y., Goldfarb, L., Gomis, M., Huang, M., Leitzell, K., Lonnoy, E., Matthews, J., Maycock, T., Waterfield, T., Yelekçi, O., Yu, R., and Zhou, B., pp. 673–816, Cambridge University Press, Cambridge, United Kingdom and New York, NY, USA, https://doi.org/10.1017/9781009157896.007, type: Book Section, 2021.

Chandra, N., Patra, P. K., Fujita, R., Höglund-Isaksson, L., Umezawa, T., Goto, D., Morimoto, S., Vaughn, B. H., and Röckmann, T.: Methane emissions decreased in fossil fuel exploitation and sustainably increased in microbial source sectors during 1990–2020, Communications Earth & Environment, 5, 1–15, https://doi.org/10.1038/s43247-024-01286-x, publisher: Nature Publishing Group, 2024.

Clark, P. U., Shakun, J. D., Marcott, S. A., Mix, A. C., Eby, M., Kulp, S., Levermann, A., Milne, G. A., Pfister, P. L., Santer, B. D., Schrag, D. P., Solomon, S., Stocker, T. F., Strauss, B. H., Weaver, A. J., Winkelmann, R., Archer, D., Bard, E., Goldner, A., Lambeck, K., Pierrehumbert, R. T., and Plattner, G.-K.: Consequences of twenty-first-century policy for multi-millennial climate and sea-level change, Nature Climate Change, 6, 360–369, https://doi.org/10.1038/nclimate2923, 2016.

Colbourn, G., Ridgwell, A., and Lenton, T. M.: The Rock Geochemical Model (RokGeM) v0.9, Geoscientific Model Development, 6, 1543–1573, https://doi.org/10.5194/gmd-6-1543-2013, 2013.

Colbourn, G., Ridgwell, A., and Lenton, T. M.: The Time Scale of the Silicate Weathering Negative Feedback on Atmospheric Co2, Global Biogeochemical Cycles, 29, 583–596, https://doi.org/10.1002/2014GB005054, 2015.

Coulon, V., Klose, A. K., Kittel, C., Edwards, T., Turner, F., Winkelmann, R., and Pattyn, F.: Disentangling the drivers of future Antarctic ice loss with a historically calibrated ice-sheet model, The Cryosphere, 2024.

Couplet, V., Crucifix, M., and Martínez Montero, M.: SURFERv3.0 code, https://zenodo.org/records/12774162, publisher: Zenodo, 2024.

Crameri, F.: Scientific colour maps, https://doi.org/10.5281/zenodo.8409685, 2023.

DeVries, T. and Weber, T.: The export and fate of organic matter in the ocean: New constraints from combining satellite and oceanographic tracer observations, Global Biogeochemical Cycles, 31, 535–555, https://doi.org/10.1002/2016GB005551, _eprint: https://onlinelibrary.wiley.com/doi/pdf/10.1002/2016GB005551, 2017.

Dickson, A. G.: Thermodynamics of the dissociation of boric acid in synthetic seawater from 273.15 to 318.15 K, Deep Sea Research Part A. Oceanographic Research Papers, 37, 755–766, https://doi.org/10.1016/0198-0149(90)90004-F, 1990.

Dickson, A. G. and Millero, F. J.: A comparison of the equilibrium constants for the dissociation of carbonic acid in seawater media, p. 11, 1987.

Eby, M., Zickfeld, K., Montenegro, A., Archer, D., Meissner, K. J., and Weaver, A. J.: Lifetime of Anthropogenic Climate Change: Millennial Time Scales of Potential CO2 and Surface Temperature Perturbations, Journal of Climate, 22, 2501–2511, https://doi.org/10.1175/2008JCLI2554.1, publisher: American Meteorological Society Section: Journal of Climate, 2009.

Edwards, N. R. and Marsh, R.: Uncertainties due to transport-parameter sensitivity in an efficient 3-D ocean-climate model, Climate Dynamics, 24, 415–433, https://doi.org/10.1007/s00382-004-0508-8, 2005.

Feng, R., Bhattacharya, T., Otto-Bliesner, B. L., Brady, E. C., Haywood, A. M., Tindall, J. C., Hunter, S. J., Abe-Ouchi, A., Chan, W.-L., Kageyama, M., Contoux, C., Guo, C., Li, X., Lohmann, G., Stepanek, C., Tan, N., Zhang, Q., Zhang, Z., Han, Z., Williams, C. J. R., Lunt, D. J., Dowsett, H. J., Chandan, D., and Peltier, W. R.: Past terrestrial hydroclimate sensitivity controlled by Earth system feedbacks, Nature Communications, 13, 1–11, https://doi.org/10.1038/s41467-022-28814-7, number: 1 Publisher: Nature Publishing Group, 2022.

Fewster, R. E., Morris, P. J., Ivanovic, R. F., Swindles, G. T., Peregon, A. M., and Smith, C. J.: Imminent loss of climate space for permafrost peatlands in Europe and Western Siberia, Nature Climate Change, 12, 373–379, https://doi.org/10.1038/s41558-022-01296-7, 2022.

Forster, P., Storelvmo, T., Armour, K., Collins, W., Dufresne, J.-L., Frame, D., Lunt, D., Mauritsen, T., Palmer, M., Watanabe, M., Wild, M., and Zhang, H.: The Earth's Energy Budget, Climate Feedbacks, and Climate Sensitivity, in: Climate Change 2021: The Physical Science Basis. Contribution of Working Group I to the Sixth Assessment Report of the Intergovernmental Panel on Climate Change, edited by Masson-Delmotte, V., Zhai, P., Pirani, A., Connors, S., Péan, C., Berger, S., Caud, N., Chen, Y., Goldfarb, L., Gomis, M., Huang, M., Leitzell, K., Lonnoy, E., Matthews, J., Maycock, T., Waterfield, T., Yelekçi, O., Yu, R., and Zhou, B., pp. 923–1054, Cambridge University Press, Cambridge, United Kingdom and New York, NY, USA, https://doi.org/10.1017/9781009157896.009, type: Book Section, 2021.

Fox-Kemper, B., Hewitt, H., Xiao, C., Aðalgeirsdóttir, G., Drijfhout, S., Edwards, T., Golledge, N., Hemer, M., Kopp, R., Krinner, G., Mix, A., Notz, D., Nowicki, S., Nurhati, I., Ruiz, L., Sallée, J.-B., Slangen, A., and Yu, Y.: Ocean, Cryosphere and Sea Level Change, in: Climate Change 2021: The Physical Science Basis. Contribution of Working Group I to the Sixth Assessment Report of the Intergovernmental Panel on Climate Change, edited by Masson-Delmotte, V., Zhai, P., Pirani, A., Connors, S., Péan, C., Berger, S., Caud, N., Chen, Y., Goldfarb, L., Gomis, M., Huang, M., Leitzell, K., Lonnoy, E., Matthews, J., Maycock, T., Waterfield, T., Yelekçi, O., Yu, R., and Zhou, B., pp. 1211–1362, Cambridge University Press, Cambridge, United Kingdom and New York, NY, USA, https://doi.org/10.1017/9781009157896.011, type: Book Section, 2021.

Friedlingstein, P., O'Sullivan, M., Jones, M. W., Andrew, R. M., Gregor, L., Hauck, J., Le Quéré, C., Luijkx, I. T., Olsen, A., Peters, G. P., Peters, W., Pongratz, J., Schwingshackl, C., Sitch, S., Canadell, J. G., Ciais, P., Jackson, R. B., Alin, S. R., Alkama, R., Arneth, A., Arora, V. K., Bates, N. R., Becker, M., Bellouin, N., Bittig, H. C., Bopp, L., Chevallier, F., Chini, L. P., Cronin, M., Evans, W., Falk, S., Feely, R. A., Gasser, T., Gehlen, M., Gkritzalis, T., Gloege, L., Grassi, G., Gruber, N., Gürses, , Harris, I., Hefner, M., Houghton, R. A., Hurtt, G. C., Iida, Y., Ilyina, T., Jain, A. K., Jersild, A., Kadono, K., Kato, E., Kennedy, D., Klein Goldewijk, K., Knauer, J., Korsbakken, J. I., Landschützer, P., Lefèvre, N., Lindsay, K., Liu, J., Liu, Z., Marland, G., Mayot, N., McGrath, M. J., Metzl, N., Monacci, N. M., Munro, D. R., Nakaoka, S.-I., Niwa, Y., O'Brien, K., Ono, T., Palmer, P. I., Pan, N., Pierrot, D., Pocock, K., Poulter, B., Resplandy, L., Robertson, E., Rödenbeck, C., Rodriguez, C., Rosan, T. M., Schwinger, J., Séférian, R., Shutler, J. D., Skjelvan, I., Steinhoff, T., Sun, Q., Sutton, A. J., Sweeney, C., Takao, S., Tanhua, T., Tans, P. P., Tian, X., Tian, H., Tilbrook, B., Tsujino, H., Tubiello, F., van der Werf, G. R., Walker, A. P., Wanninkhof, R., Whitehead, C., Willstrand Wranne, A., Wright, R., Yuan, W., Yue, C., Yue, X., Zaehle, S., Zeng, J., and Zheng, B.: Global Carbon Budget 2022, Earth System Science Data, 14, 4811–4900, https://doi.org/10.5194/essd-14-4811-2022, 2022.

Garbe, J., Albrecht, T., Levermann, A., Donges, J. F., and Winkelmann, R.: The hysteresis of the Antarctic Ice Sheet, Nature, 585, 538–544, https://doi.org/10.1038/s41586-020-2727-5, 2020.

Gidden, M. J., Riahi, K., Smith, S. J., Fujimori, S., Luderer, G., Kriegler, E., van Vuuren, D. P., van den Berg, M., Feng, L., Klein, D., Calvin, K., Doelman, J. C., Frank, S., Fricko, O., Harmsen, M., Hasegawa, T., Havlik, P., Hilaire, J., Hoesly, R., Horing, J., Popp, A., Stehfest, E., and Takahashi, K.: Global emissions pathways under different socioeconomic scenarios for use in CMIP6: a dataset of harmonized emissions trajectories through the end of the century, Geoscientific Model Development, 12, 1443–1475, https://doi.org/10.5194/gmd-12-1443-2019, publisher: Copernicus GmbH, 2019.

Goosse, H.: Climate System Dynamics and Modelling, Cambridge University Press, Cambridge, ISBN 978-1-107-08389-9, https://doi.org/10.1017/CBO9781316018682, 2015.

Hauck, J., Zeising, M., Le Quéré, C., Gruber, N., Bakker, D. C. E., Bopp, L., Chau, T. T. T., Gürses, , Ilyina, T., Landschützer, P., Lenton, A., Resplandy, L., Rödenbeck, C., Schwinger, J., and Séférian, R.: Consistency and Challenges in the Ocean Carbon Sink Estimate for the Global Carbon Budget, Frontiers in Marine Science, 7, https://doi.org/10.3389/fmars.2020.571720, publisher: Frontiers, 2020.

Hays, J. D., Imbrie, J., and Shackleton, N. J.: Variations in the Earth's Orbit: Pacemaker of the Ice Ages, Science, 194, 1121–1132, https://doi.org/10.1126/science.194.4270.1121, publisher: American Association for the Advancement of Science, 1976.

Henson, S. A., Laufkötter, C., Leung, S., Giering, S. L. C., Palevsky, H. I., and Cavan, E. L.: Uncertain response of ocean biological carbon export in a changing world, Nature Geoscience, 15, 248–254, https://doi.org/10.1038/s41561-022-00927-0, number: 4 Publisher: Nature Publishing Group, 2022.

1340   Humphreys, M. P., Lewis, E. R., Sharp, J. D., and Pierrot, D.: PyCO2SYS v1.8: marine carbonate system calculations in Python, Geoscientific Model Development, 15, 15–43, https://doi.org/10.5194/gmd-15-15-2022, publisher: Copernicus GmbH, 2022.

IPCC: Climate Change 2021: The Physical Science Basis. Contribution of Working Group I to the Sixth Assessment Report of the Intergovernmental Panel on Climate Change, vol. In Press, Cambridge University Press, Cambridge, United Kingdom and New York, NY, USA, https://doi.org/10.1017/9781009157896, type: Book, 2021a.

1345   IPCC: Summary for Policymakers, in: Climate Change 2021: The Physical Science Basis. Contribution of Working Group I to the Sixth Assessment Report of the Intergovernmental Panel on Climate Change, edited by Masson-Delmotte, V., Zhai, P., Pirani, A., Connors, S., Péan, C., Berger, S., Caud, N., Chen, Y., Goldfarb, L., Gomis, M., Huang, M., Leitzell, K., Lonnoy, E., Matthews, J., Maycock, T., Waterfield, T., Yelekçi, O., Yu, R., and Zhou, B., p. 3-32, Cambridge University Press, Cambridge, United Kingdom and New York, NY, USA, https://doi.org/10.1017/9781009157896.001, type: Book Section, 2021b.

1350   Jones, C. D., Frölicher, T. L., Koven, C., MacDougall, A. H., Matthews, H. D., Zickfeld, K., Rogelj, J., Tokarska, K. B., Gillett, N. P., Ilyina, T., Meinshausen, M., Mengis, N., Séférian, R., Eby, M., and Burger, F. A.: The Zero Emissions Commitment Model Intercomparison Project (ZECMIP) contribution to C4MIP: quantifying committed climate changes following zero carbon emissions, Geoscientific Model Development, 12, 4375–4385, https://doi.org/10.5194/gmd-12-4375-2019, publisher: Copernicus GmbH, 2019.

Jones, M. W., Peters, G. P., Gasser, T., Andrew, R. M., Schwingshackl, C., Gütschow, J., Houghton, R. A., Friedlingstein, P., Pongratz, J., and
1355   Le Quéré, C.: National contributions to climate change due to historical emissions of carbon dioxide, methane, and nitrous oxide since 1850, Scientific Data, 10, 155, https://doi.org/10.1038/s41597-023-02041-1, 2023.

Kaufhold, C., Willeit, M., Liu, B., and Ganopolski, A.: Assessing the lifetime of anthropogenic $CO2$ and its sensitivity to different carbon cycle processes, 2024.

Keir, R. S.: On the Late Pleistocene ocean geochemistry and circulation, Paleoceanography, 3, 413–445,
1360   https://doi.org/10.1029/PA003i004p00413, 1988.

Kohfeld, K. E. and Ridgwell, A.: Glacial-interglacial variability in atmospheric $CO2$, in: Geophysical Monograph Series, edited by Le Quéré, C. and Saltzman, E. S., vol. 187, pp. 251–286, American Geophysical Union, Washington, D. C., ISBN 978-0-87590-477-1, https://doi.org/10.1029/2008GM000845, 2009.

Kukla, T., Ibarra, D. E., Lau, K. V., and Rugenstein, J. K. C.: All aboard! Earth system investigations with the CH2O-CHOO TRAIN v1.0,
1365   Geoscientific Model Development, 16, 5515–5538, https://doi.org/10.5194/gmd-16-5515-2023, publisher: Copernicus GmbH, 2023.

Kump, L. R., Brantley, S. L., and Arthur, M. A.: Chemical Weathering, Atmospheric $CO2$, and Climate, Annual Review of Earth and Planetary Sciences, 28, 611–667, https://doi.org/10.1146/annurev.earth.28.1.611, publisher: Annual Reviews, 2000.

Köhler, P. and Munhoven, G.: Late Pleistocene Carbon Cycle Revisited by Considering Solid Earth Processes, Paleoceanography and Paleoclimatology, 35, e2020PA004 020, https://doi.org/10.1029/2020PA004020, _eprint:
1370   https://onlinelibrary.wiley.com/doi/pdf/10.1029/2020PA004020, 2020.

Köhler, P., Nehrbass-Ahles, C., Schmitt, J., Stocker, T. F., and Fischer, H.: A 156 kyr smoothed history of the atmospheric greenhouse gases CO_2, CH_4, and N_2O and their radiative forcing, Earth System Science Data, 9, 363–387, https://doi.org/10.5194/essd-9-363-2017, publisher: Copernicus GmbH, 2017.

Lauvset, S. K., Key, R. M., Olsen, A., van Heuven, S., Velo, A., Lin, X., Schirnick, C., Kozyr, A., Tanhua, T., Hoppema, M., Jutterström, S., Steinfeldt, R., Jeansson, E., Ishii, M., Perez, F. F., Suzuki, T., and Watelet, S.: A new global interior ocean mapped climatology: the 1∘ × 1∘ GLODAP version 2, 2016.

Lenton, T. M.: Land and ocean carbon cycle feedback effects on global warming in a simple Earth system model, Tellus B, 52, 1159–1188, https://doi.org/10.1034/j.1600-0889.2000.01104.x, 2000.

Lenton, T. M. and Britton, C.: Enhanced carbonate and silicate weathering accelerates recovery from fossil fuel CO_2 perturbations, Global Biogeochemical Cycles, 20, https://doi.org/10.1029/2005GB002678, _eprint: https://onlinelibrary.wiley.com/doi/pdf/10.1029/2005GB002678, 2006.

Lenton, T. M., Held, H., Kriegler, E., Hall, J. W., Lucht, W., Rahmstorf, S., and Schellnhuber, H. J.: Tipping elements in the Earth's climate system, Proceedings of the National Academy of Sciences, 105, 1786–1793, https://doi.org/10.1073/pnas.0705414105, 2008.

Lenton, T. M., Rockström, J., Gaffney, O., Rahmstorf, S., Richardson, K., Steffen, W., and Schellnhuber, H. J.: Climate tipping points — too risky to bet against, Nature, 575, 592–595, https://doi.org/10.1038/d41586-019-03595-0, 2019.

Levy, M., Bopp, L., Karleskind, P., Resplandy, L., Ethe, C., and Pinsard, F.: Physical pathways for carbon transfers between the surface mixed layer and the ocean interior, Global Biogeochemical Cycles, 27, 1001–1012, https://doi.org/10.1002/gbc.20092, _eprint: https://onlinelibrary.wiley.com/doi/pdf/10.1002/gbc.20092, 2013.

Lord, N. S., Ridgwell, A., Thorne, M. C., and Lunt, D. J.: An impulse response function for the "long tail" of excess atmospheric CO_2 in an Earth system model, Global Biogeochemical Cycles, 30, 2–17, https://doi.org/10.1002/2014GB005074, 2016.

MacDougall, A. H., Frölicher, T. L., Jones, C. D., Rogelj, J., Matthews, H. D., Zickfeld, K., Arora, V. K., Barrett, N. J., Brovkin, V., Burger, F. A., Eby, M., Eliseev, A. V., Hajima, T., Holden, P. B., Jeltsch-Thömmes, A., Koven, C., Mengis, N., Menviel, L., Michou, M., Mokhov, I. I., Oka, A., Schwinger, J., Séférian, R., Shaffer, G., Sokolov, A., Tachiiri, K., Tjiputra, J., Wiltshire, A., and Ziehn, T.: Is there warming in the pipeline? A multi-model analysis of the Zero Emissions Commitment from CO2, 2020.

Maher, K. and Chamberlain, C. P.: Hydrologic regulation of chemical weathering and the geologic carbon cycle, Science (New York, N.Y.), 343, 1502–1504, https://doi.org/10.1126/science.1250770, 2014.

Martínez Montero, M., Crucifix, M., Couplet, V., Brede, N., and Botta, N.: SURFER v2.0: a flexible and simple model linking anthropogenic CO_2 emissions and solar radiation modification to ocean acidification and sea level rise, Geoscientific Model Development, 15, 8059–8084, https://doi.org/10.5194/gmd-15-8059-2022, 2022.

McDougall, T. J. and Barker, P. M.: Getting started with TEOS-10 and the Gibbs Seawater (GSW) Oceanographic Toolbox, SCOR/IAPSO WG127, ISBN 978-0-646-55621-5, 2011.

Mehrbach, C., Culberson, C. H., Hawley, J. E., and Pytkowicx, R. M.: MEASUREMENT OF THE APPARENT DISSOCIATION CONSTANTS OF CARBONIC ACID IN SEAWATER AT ATMOSPHERIC PRESSURE1, Limnology and Oceanography, 18, 897–907, https://doi.org/10.4319/lo.1973.18.6.0897, 1973.

Meinshausen, M., Nicholls, Z. R. J., Lewis, J., Gidden, M. J., Vogel, E., Freund, M., Beyerle, U., Gessner, C., Nauels, A., Bauer, N., Canadell, J. G., Daniel, J. S., John, A., Krummel, P. B., Luderer, G., Meinshausen, N., Montzka, S. A., Rayner, P. J., Reimann, S., Smith, S. J., van den Berg, M., Velders, G. J. M., Vollmer, M. K., and Wang, R. H. J.: The shared socio-economic pathway (SSP) greenhouse gas concentrations and their extensions to 2500, Geoscientific Model Development, 13, 3571–3605, https://doi.org/10.5194/gmd-13-3571-2020, 2020.

Middelburg, J. J., Soetaert, K., and Hagens, M.: Ocean Alkalinity, Buffering and Biogeochemical Processes, Reviews of Geophysics, 58, e2019RG000 681, https://doi.org/10.1029/2019RG000681, _eprint: https://onlinelibrary.wiley.com/doi/pdf/10.1029/2019RG000681, 2020.

Millero, F. J.: The thermodynamics of the carbonate system in seawater, Geochimica et Cosmochimica Acta, 43, 1651–1661, https://doi.org/10.1016/0016-7037(79)90184-4, 1979.

Millero, F. J.: Thermodynamics of the carbon dioxide system in the oceans, Geochimica et Cosmochimica Acta, 59, 661–677, https://doi.org/10.1016/0016-7037(94)00354-O, 1995.

Milliman, J. D.: Production and accumulation of calcium carbonate in the ocean: Budget of a nonsteady state, Global Biogeochemical Cycles, 7, 927–957, https://doi.org/10.1029/93GB02524, publisher: John Wiley & Sons, Ltd, 1993.

Milliman, J. D. and Droxler, A. W.: Neritic and pelagic carbonate sedimentation in the marine environment: ignorance is not bliss, Geologische Rundschau, 85, 496–504, https://doi.org/10.1007/BF02369004, 1996.

Montero, M. M., Brede, N., Couplet, V., Crucifix, M., Botta, N., and Wieners, C.: Lost options commitment: how short-term policies affect long-term scope of action, Tech. Rep. arXiv:2309.07743, arXiv, http://arxiv.org/abs/2309.07743, arXiv:2309.07743 [physics] type: article, 2023.

Mucci, A.: The solubility of calcite and aragonite in seawater at various salinities, temperatures, and one atmosphere total pressure, American Journal of Science, 283, 780–799, https://doi.org/10.2475/ajs.283.7.780, publisher: American Journal of Science, 1983.

Munhoven, G.: Mathematics of the total alkalinity–pH equation – pathway to robust and universal solution algorithms: the SolveSAPHE package v1.0.1, Geoscientific Model Development, 6, 1367–1388, https://doi.org/10.5194/gmd-6-1367-2013, publisher: Copernicus GmbH, 2013.

Munhoven, G. and François, L. M.: Glacial-interglacial variability of atmospheric CO2 due to changing continental silicate rock weathering: A model study, Journal of Geophysical Research: Atmospheres, 101, 21 423–21 437, https://doi.org/10.1029/96JD01842, _eprint: https://onlinelibrary.wiley.com/doi/pdf/10.1029/96JD01842, 1996.

Myhre, G., Highwood, E. J., Shine, K. P., and Stordal, F.: New estimates of radiative forcing due to well mixed greenhouse gases, Geophysical Research Letters, 25, 2715–2718, https://doi.org/10.1029/98GL01908, 1998.

Nisbet, E. G., Manning, M. R., Dlugokencky, E. J., Michel, S. E., Lan, X., Röckmann, T., Denier van der Gon, H. A. C., Schmitt, J., Palmer, P. I., Dyonisius, M. N., Oh, Y., Fisher, R. E., Lowry, D., France, J. L., White, J. W. C., Brailsford, G., and Bromley, T.: Atmospheric Methane: Comparison Between Methane's Record in 2006–2022 and During Glacial Terminations, Global Biogeochemical Cycles, 37, e2023GB007 875, https://doi.org/10.1029/2023GB007875, _eprint: https://onlinelibrary.wiley.com/doi/pdf/10.1029/2023GB007875, 2023.

Petzold, L.: Automatic Selection of Methods for Solving Stiff and Nonstiff Systems of Ordinary Differential Equations, SIAM Journal on Scientific and Statistical Computing, 4, 136–148, https://doi.org/10.1137/0904010, publisher: Society for Industrial and Applied Mathematics, 1983.

Planchat, A., Bopp, L., Kwiatkowski, L., and Torres, O.: Carbonate pump feedbacks on alkalinity and the carbon cycle in the 21st century and beyond, 2023.

Raworth, K.: A Safe and Just Space for Humanity: Can we live within the doughnut?, 2012.

Riahi, K., van Vuuren, D. P., Kriegler, E., Edmonds, J., O'Neill, B. C., Fujimori, S., Bauer, N., Calvin, K., Dellink, R., Fricko, O., Lutz, W., Popp, A., Cuaresma, J. C., Kc, S., Leimbach, M., Jiang, L., Kram, T., Rao, S., Emmerling, J., Ebi, K., Hasegawa, T., Havlik, P., Humpenöder, F., Da Silva, L. A., Smith, S., Stehfest, E., Bosetti, V., Eom, J., Gernaat, D., Masui, T., Rogelj, J., Strefler, J., Drouet, L., Krey, V., Luderer, G., Harmsen, M., Takahashi, K., Baumstark, L., Doelman, J. C., Kainuma, M., Klimont, Z., Marangoni, G., Lotze-Campen, H., Obersteiner, M., Tabeau, A., and Tavoni, M.: The Shared Socioeconomic Pathways and their energy, land use, and greenhouse

gas emissions implications: An overview, Global Environmental Change, 42, 153–168, https://doi.org/10.1016/j.gloenvcha.2016.05.009, 2017.

Ridgwell, A. and Hargreaves, J. C.: Regulation of atmospheric CO_2 by deep-sea sediments in an Earth system model: REGULATION OF CO_2 BY DEEP-SEA SEDIMENTS, Global Biogeochemical Cycles, 21, n/a–n/a, https://doi.org/10.1029/2006GB002764, 2007.

Ridgwell, A., Hargreaves, J. C., Edwards, N. R., Annan, J. D., Lenton, T. M., Marsh, R., Yool, A., and Watson, A.: Marine geochemical data assimilation in an efficient Earth System Model of global biogeochemical cycling, Biogeosciences, 4, 87–104, https://doi.org/10.5194/bg-4-87-2007, publisher: Copernicus GmbH, 2007.

Ritchie, P., Karabacak, , and Sieber, J.: Inverse-square law between time and amplitude for crossing tipping thresholds, Proceedings of the Royal Society A: Mathematical, Physical and Engineering Sciences, 475, 20180 504, https://doi.org/10.1098/rspa.2018.0504, 2019.

Ritchie, P. D. L., Clarke, J. J., Cox, P. M., and Huntingford, C.: Overshooting tipping point thresholds in a changing climate, Nature, 592, 517–523, https://doi.org/10.1038/s41586-021-03263-2, 2021.

Ross, P. M., Parker, L., O'Connor, W. A., and Bailey, E. A.: The Impact of Ocean Acidification on Reproduction, Early Development and Settlement of Marine Organisms, Water, 3, 1005–1030, https://doi.org/10.3390/w3041005, number: 4 Publisher: Molecular Diversity Preservation International, 2011.

Ruvalcaba Baroni, I., Palastanga, V., and Slomp, C. P.: Enhanced Organic Carbon Burial in Sediments of Oxygen Minimum Zones Upon Ocean Deoxygenation, Frontiers in Marine Science, 6, https://doi.org/10.3389/fmars.2019.00839, publisher: Frontiers, 2020.

Sarmiento, J. L. and Gruber, N.: Ocean biogeochemical dynamics, Princeton University Press, Princeton, ISBN 978-0-691-01707-5, oCLC: ocm60651167, 2006.

Saunois, M., Stavert, A. R., Poulter, B., Bousquet, P., Canadell, J. G., Jackson, R. B., Raymond, P. A., Dlugokencky, E. J., Houweling, S., Patra, P. K., Ciais, P., Arora, V. K., Bastviken, D., Bergamaschi, P., Blake, D. R., Brailsford, G., Bruhwiler, L., Carlson, K. M., Carrol, M., Castaldi, S., Chandra, N., Crevoisier, C., Crill, P. M., Covey, K., Curry, C. L., Etiope, G., Frankenberg, C., Gedney, N., Hegglin, M. I., Höglund-Isaksson, L., Hugelius, G., Ishizawa, M., Ito, A., Janssens-Maenhout, G., Jensen, K. M., Joos, F., Kleinen, T., Krummel, P. B., Langenfelds, R. L., Laruelle, G. G., Liu, L., Machida, T., Maksyutov, S., McDonald, K. C., McNorton, J., Miller, P. A., Melton, J. R., Morino, I., Müller, J., Murguia-Flores, F., Naik, V., Niwa, Y., Noce, S., O'Doherty, S., Parker, R. J., Peng, C., Peng, S., Peters, G. P., Prigent, C., Prinn, R., Ramonet, M., Regnier, P., Riley, W. J., Rosentreter, J. A., Segers, A., Simpson, I. J., Shi, H., Smith, S. J., Steele, L. P., Thornton, B. F., Tian, H., Tohjima, Y., Tubiello, F. N., Tsuruta, A., Viovy, N., Voulgarakis, A., Weber, T. S., van Weele, M., van der Werf, G. R., Weiss, R. F., Worthy, D., Wunch, D., Yin, Y., Yoshida, Y., Zhang, W., Zhang, Z., Zhao, Y., Zheng, B., Zhu, Q., Zhu, Q., and Zhuang, Q.: The Global Methane Budget 2000–2017, Earth System Science Data, 12, 1561–1623, https://doi.org/10.5194/essd-12-1561-2020, publisher: Copernicus GmbH, 2020.

Schlanger, S. and Jenkyns, H.: Cretaceous oceanic anoxic events: causes and consequences, Geologie en mijnbouw, 55, publisher: Netherlands Journal of Geosciences Foundation, 1976.

Schmittner, A., Oschlies, A., Matthews, H. D., and Galbraith, E. D.: Future changes in climate, ocean circulation, ecosystems, and biogeochemical cycling simulated for a business-as-usual CO2 emission scenario until year 4000 AD, Global Biogeochemical Cycles, 22, https://doi.org/10.1029/2007GB002953, _eprint: https://onlinelibrary.wiley.com/doi/pdf/10.1029/2007GB002953, 2008.

Skeie, R. B., Hodnebrog, , and Myhre, G.: Trends in atmospheric methane concentrations since 1990 were driven and modified by anthropogenic emissions, Communications Earth & Environment, 4, 1–14, https://doi.org/10.1038/s43247-023-00969-1, publisher: Nature Publishing Group, 2023.

70

Smith, C., Nicholls, Z., Armour, K., Collins, W., Forster, P., Meinshausen, M., Palmer, M., and Watanabe, M.: The Earth's Energy Budget, Climate Feedbacks, and Climate Sensitivity Supplementary Material, in: Climate Change 2021: The Physical Science Basis. Contribution of Working Group I to the Sixth Assessment Report of the Intergovernmental Panel on Climate Change, edited by Masson-Delmotte, V., Zhai, P., Pirani, A., Connors, S., Péan, C., Berger, S., Caud, N., Chen, Y., Goldfarb, L., Gomis, M., Huang, M., Leitzell, K., Lonnoy, E., Matthews, J., Maycock, T., Waterfield, T., Yelekçi, O., Yu, R., and Zhou, B., Availablefromhttps://www.ipcc.ch/, type: Book Section, 2021.

Steffen, W., Rockström, J., Richardson, K., Lenton, T. M., Folke, C., Liverman, D., Summerhayes, C. P., Barnosky, A. D., Cornell, S. E., Crucifix, M., Donges, J. F., Fetzer, I., Lade, S. J., Scheffer, M., Winkelmann, R., and Schellnhuber, H. J.: Trajectories of the Earth System in the Anthropocene, Proceedings of the National Academy of Sciences, 115, 8252–8259, https://doi.org/10.1073/pnas.1810141115, 2018.

Stocker, T., Qin, D., Plattner, G.-K., Tignor, M., Allen, S., Boschung, J., Nauels, A., Xia, Y., Bex, V., and Midgley, P., eds.: Climate Change 2013: The Physical Science Basis. Contribution of Working Group I to the Fifth Assessment Report of the Intergovernmental Panel on Climate Change, Cambridge University Press, Cambridge, United Kingdom and New York, NY, USA, 2013.

Sulpis, O., Jeansson, E., Dinauer, A., Lauvset, S. K., and Middelburg, J. J.: Calcium carbonate dissolution patterns in the ocean, Nature Geoscience, 14, 423–428, https://doi.org/10.1038/s41561-021-00743-y, number: 6 Publisher: Nature Publishing Group, 2021.

Swann, A. L., Fung, I. Y., Levis, S., Bonan, G. B., and Doney, S. C.: Changes in Arctic vegetation amplify high-latitude warming through the greenhouse effect, Proceedings of the National Academy of Sciences, 107, 1295–1300, https://doi.org/10.1073/pnas.0913846107, publisher: Proceedings of the National Academy of Sciences, 2010.

Tokarska, K. B., Gillett, N. P., Weaver, A. J., Arora, V. K., and Eby, M.: The climate response to five trillion tonnes of carbon, Nature Climate Change, 6, 851–855, https://doi.org/10.1038/nclimate3036, number: 9 Publisher: Nature Publishing Group, 2016.

Turner, A. J., Frankenberg, C., and Kort, E. A.: Interpreting contemporary trends in atmospheric methane, Proceedings of the National Academy of Sciences, 116, 2805–2813, https://doi.org/10.1073/pnas.1814297116, publisher: Proceedings of the National Academy of Sciences, 2019.

Uppström, L. R.: The boron/chlorinity ratio of deep-sea water from the Pacific Ocean, Deep Sea Research and Oceanographic Abstracts, 21, 161–162, https://doi.org/10.1016/0011-7471(74)90074-6, 1974.

Vecsei, A.: A new estimate of global reefal carbonate production including the fore-reefs, Global and Planetary Change, 43, 1–18, https://doi.org/10.1016/j.gloplacha.2003.12.002, 2004.

Volk, T. and Hoffert, M. I.: Ocean Carbon Pumps: Analysis of Relative Strengths and Efficiencies in Ocean-Driven Atmospheric CO2 Changes, in: The Carbon Cycle and Atmospheric CO2: Natural Variations Archean to Present, pp. 99–110, American Geophysical Union (AGU), ISBN 978-1-118-66432-2, https://doi.org/10.1029/GM032p0099, _eprint: https://onlinelibrary.wiley.com/doi/pdf/10.1029/GM032p0099, 1985.

Walker, J. C. G., Hays, P. B., and Kasting, J. F.: A negative feedback mechanism for the long-term stabilization of Earth's surface temperature, Journal of Geophysical Research: Oceans, 86, 9776–9782, https://doi.org/10.1029/JC086iC10p09776, _eprint: https://onlinelibrary.wiley.com/doi/pdf/10.1029/JC086iC10p09776, 1981.

Weiss, R.: Carbon dioxide in water and seawater: the solubility of a non-ideal gas, Marine Chemistry, 2, 203–215, https://doi.org/10.1016/0304-4203(74)90015-2, 1974.

West, A. J., Galy, A., and Bickle, M.: Tectonic and climatic controls on silicate weathering, Earth and Planetary Science Letters, 235, 211–228, https://doi.org/10.1016/j.epsl.2005.03.020, 2005.

Willeit, M., Ganopolski, A., and Feulner, G.: Asymmetry and uncertainties in biogeophysical climate–vegetation feedback over a range of CO_2 forcings, 2014.

1525 Willeit, M., Calov, R., Talento, S., Greve, R., Bernales, J., Klemann, V., Bagge, M., and Ganopolski, A.: Glacial inception through rapid ice area increase driven by albedo and vegetation feedbacks, 2023.

Williams, R. G., Goodwin, P., Ridgwell, A., and Woodworth, P. L.: How warming and steric sea level rise relate to cumulative carbon emissions, Geophysical Research Letters, 39, https://doi.org/10.1029/2012GL052771, _eprint: https://onlinelibrary.wiley.com/doi/pdf/10.1029/2012GL052771, 2012.

1530 WMO: WMO confirms 2024 as warmest year on record at about 1.55°C above pre-industrial level, https://wmo.int/media/news/wmo-confirms-2024-warmest-year-record-about-155degc-above-pre-industrial-level, 2025.

Yang, M., Bell, T. G., Bidlot, J.-R., Blomquist, B. W., Butterworth, B. J., Dong, Y., Fairall, C. W., Landwehr, S., Marandino, C. A., Miller, S. D., Saltzman, E. S., and Zavarsky, A.: Global Synthesis of Air-Sea CO_2 Transfer Velocity Estimates From Ship-Based Eddy Covariance Measurements, Frontiers in Marine Science, 9, https://www.frontiersin.org/articles/10.3389/fmars.2022.826421, 2022.

1535 Zeebe, R. E.: LOSCAR: Long-term Ocean-atmosphere-Sediment CArbon cycle Reservoir Model v2.0.4, Geosci. Model Dev., 2012.

Zeebe, R. E. and Westbroek, P.: A simple model for the $CaCO_3$ saturation state of the ocean: The "Strangelove," the "Neritan," and the "Cretan" Ocean: MODEL FOR $CACO_3$ SATURATION STATE, Geochemistry, Geophysics, Geosystems, 4, https://doi.org/10.1029/2003GC000538, 2003.

Zickfeld, K., Eby, M., Weaver, A. J., Alexander, K., Crespin, E., Edwards, N. R., Eliseev, A. V., Feulner, G., Fichefet, T., Forest, C. E.,
1540 Friedlingstein, P., Goosse, H., Holden, P. B., Joos, F., Kawamiya, M., Kicklighter, D., Kienert, H., Matsumoto, K., Mokhov, I. I., Monier, E., Olsen, S. M., Pedersen, J. O. P., Perrette, M., Philippon-Berthier, G., Ridgwell, A., Schlosser, A., Deimling, T. S. V., Shaffer, G., Sokolov, A., Spahni, R., Steinacher, M., Tachiiri, K., Tokos, K. S., Yoshimori, M., Zeng, N., and Zhao, F.: Long-Term Climate Change Commitment and Reversibility: An EMIC Intercomparison, Journal of Climate, 26, 5782–5809, https://doi.org/10.1175/JCLI-D-12-00584.1, publisher: American Meteorological Society Section: Journal of Climate, 2013.
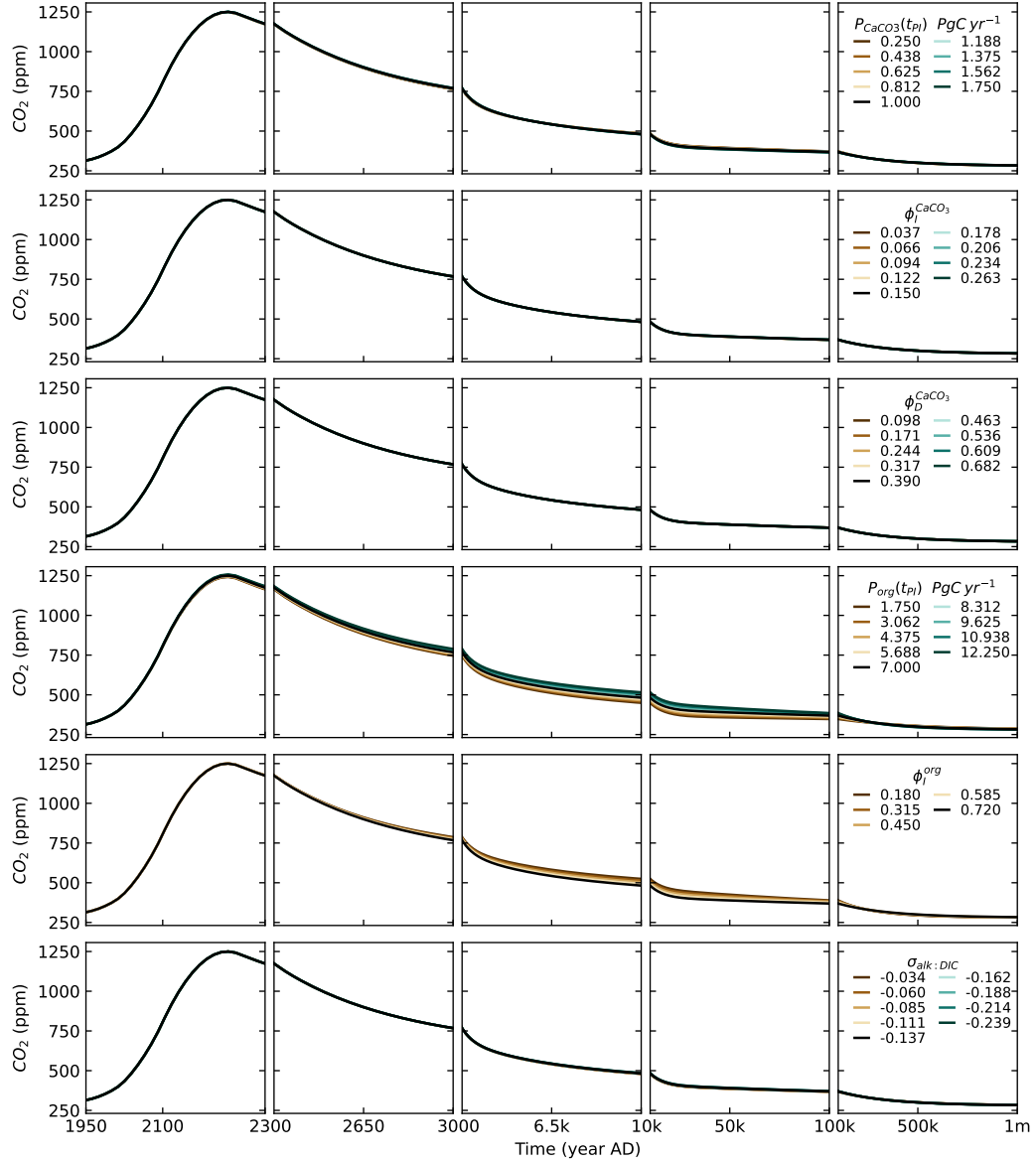
Figure D2. Atmospheric CO_2 concentration simulated by SURFER v3.0 under the SSP3-7.0 scenario for different values of P^{CaCO_3}, $\phi_I^{CaCO_3}$, $\phi_D^{CaCO_3}$, P^{org}, ϕ_I^{org}, and $\sigma_{Alk:DIC}$. Black lines indicate the atmospheric CO_2 concentration simulated for the default parameter values, as described in section 2.4.1.
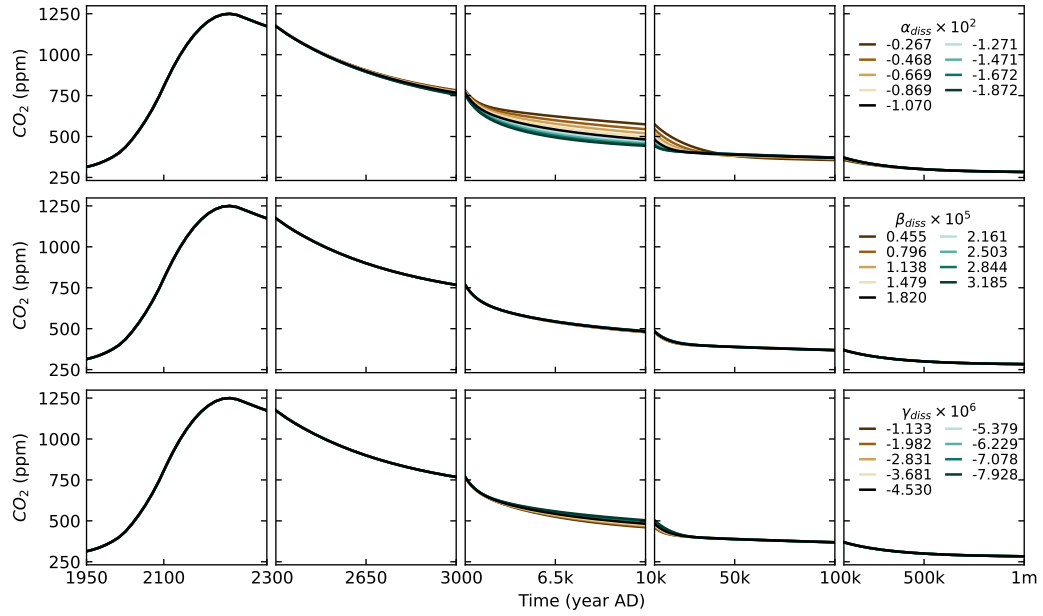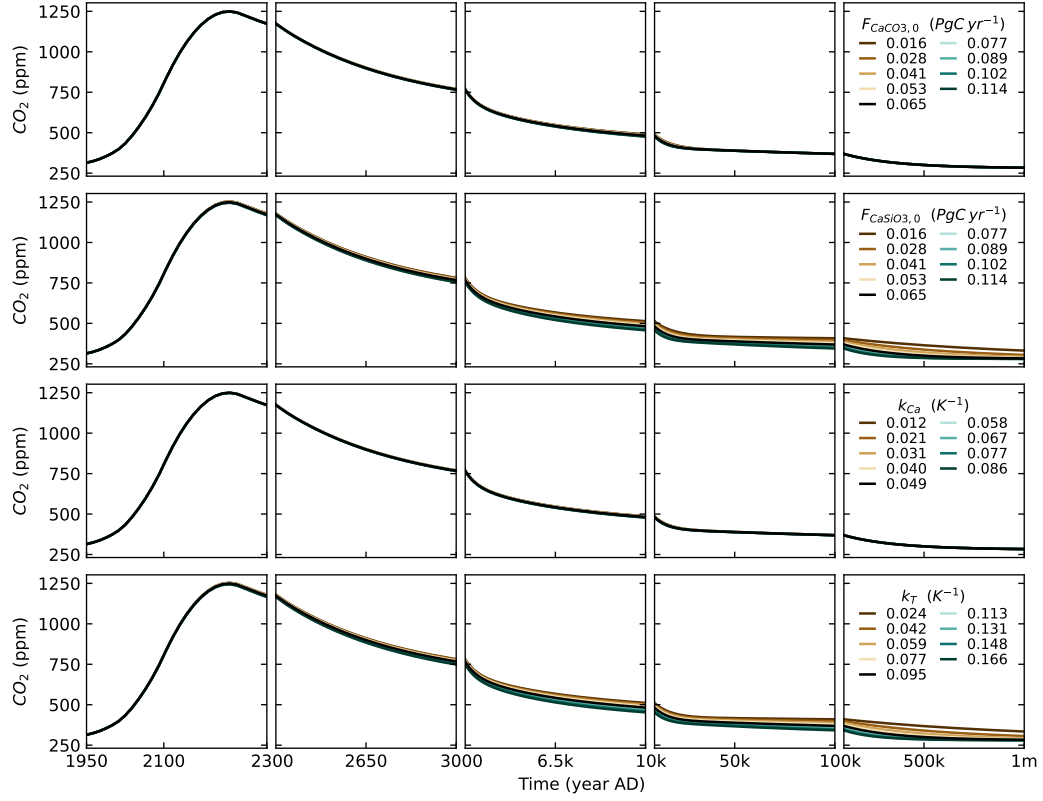
Figure D3. Atmospheric CO_2 concentration simulated by SURFER v3.0 under the SSP3-7.0 scenario for different values of α_{diss}, β_{diss}, and γ_{diss}. Black lines indicate the atmospheric CO_2 concentration simulated for the default parameter values, as described in section 2.4.1.

Figure D4. Atmospheric CO_2 concentration simulated by SURFER v3.0 under the SSP3-7.0 scenario for different values of $F_{CaCO_3,0}$, $F_{CaSiO_3,0}$, k_{Ca}, and k_T. Black lines indicate the atmospheric CO_2 concentration simulated for the default parameter values, as described in section 2.4.1.
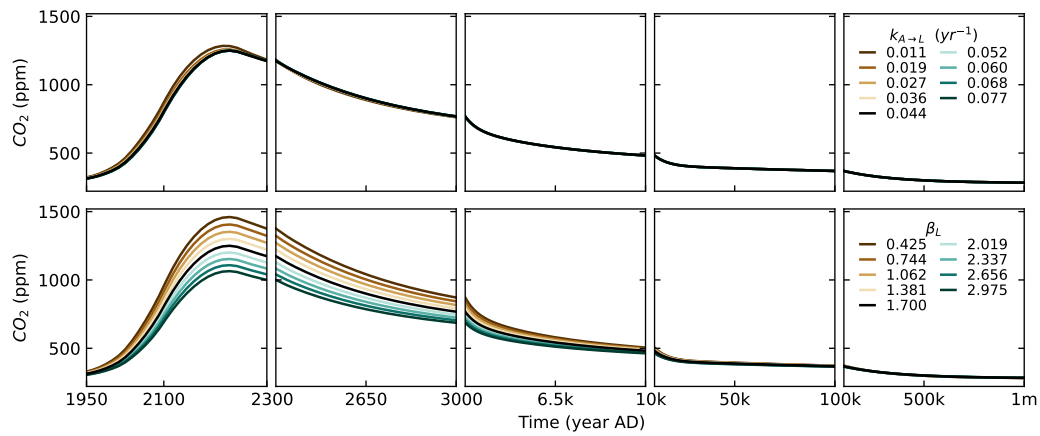
Figure D5. Atmospheric CO$_2$ concentration simulated by SURFER v3.0 under the SSP3-7.0 scenario for different values of $k_{A\to L}$, and β_L. Black lines indicate the atmospheric CO$_2$ concentration simulated for the default parameter values, as described in section 2.4.1.
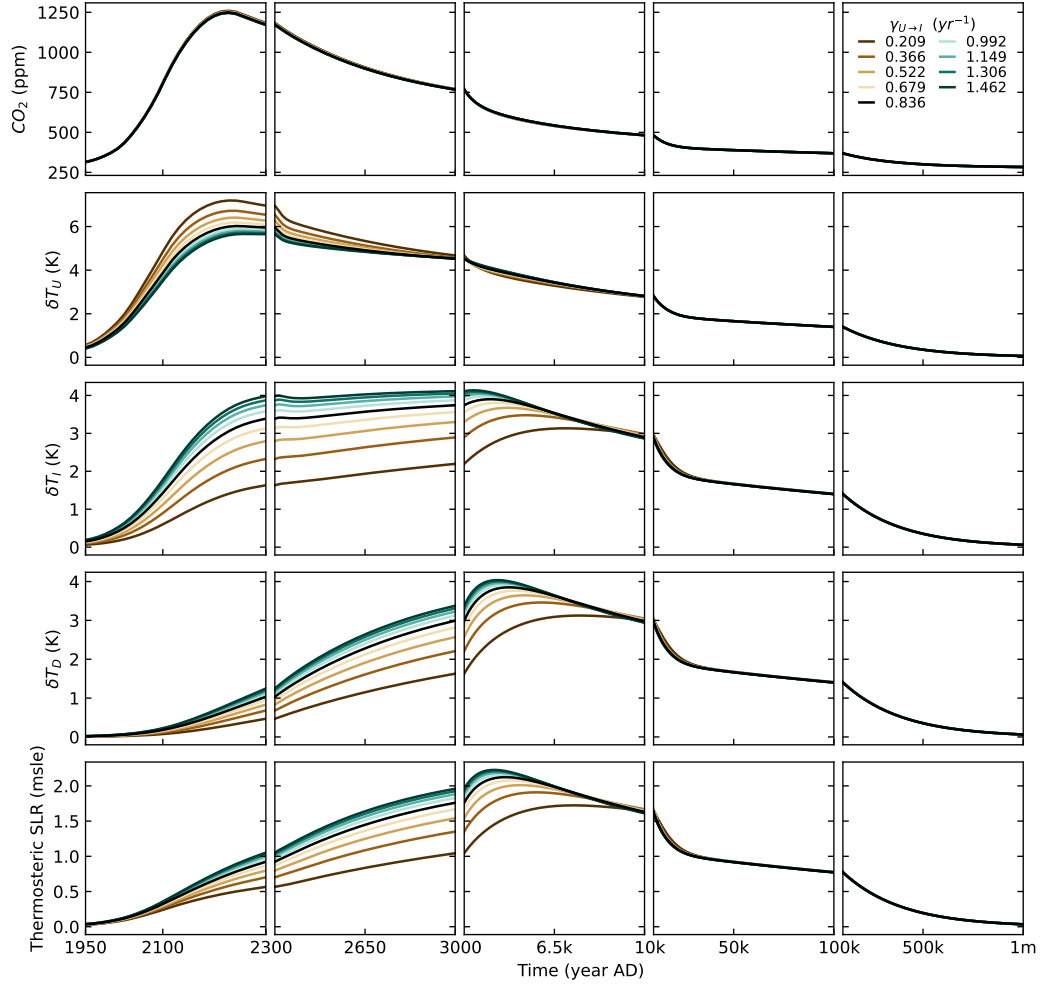
Figure D6. Atmospheric CO_2 concentration, temperatures, and thermosteric sea level rise simulated by SURFER v3.0 under the SSP3-7.0 scenario for different values of $\gamma_{U \to I}$. Black lines indicate outputs simulated for the default parameter values, as described in section 2.4.1.
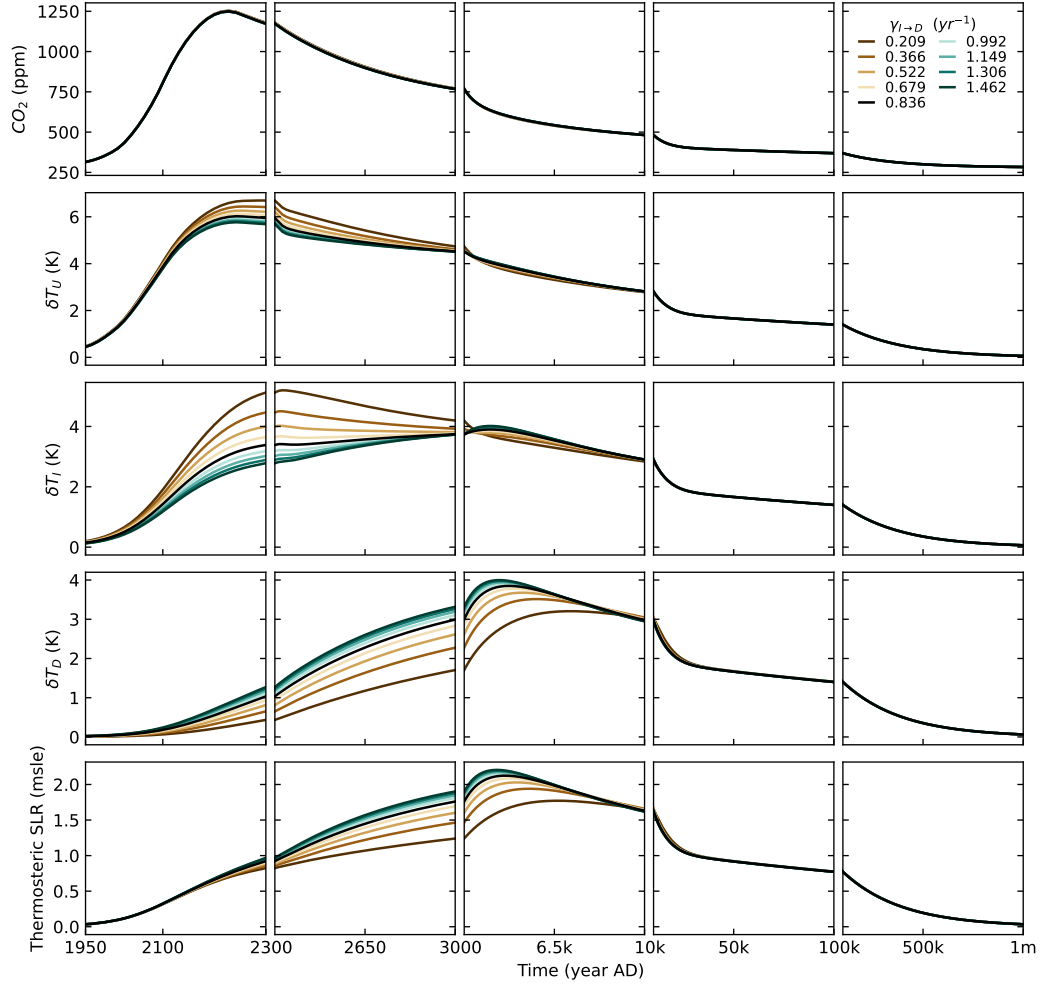
Figure D7. Atmospheric CO_2 concentration, temperatures, and thermosteric sea level rise simulated by SURFER v3.0 under the SSP3-7.0 scenario for different values of $\gamma_{I \rightarrow D}$. Black lines indicate outputs simulated for the default parameter values, as described in section 2.4.1.
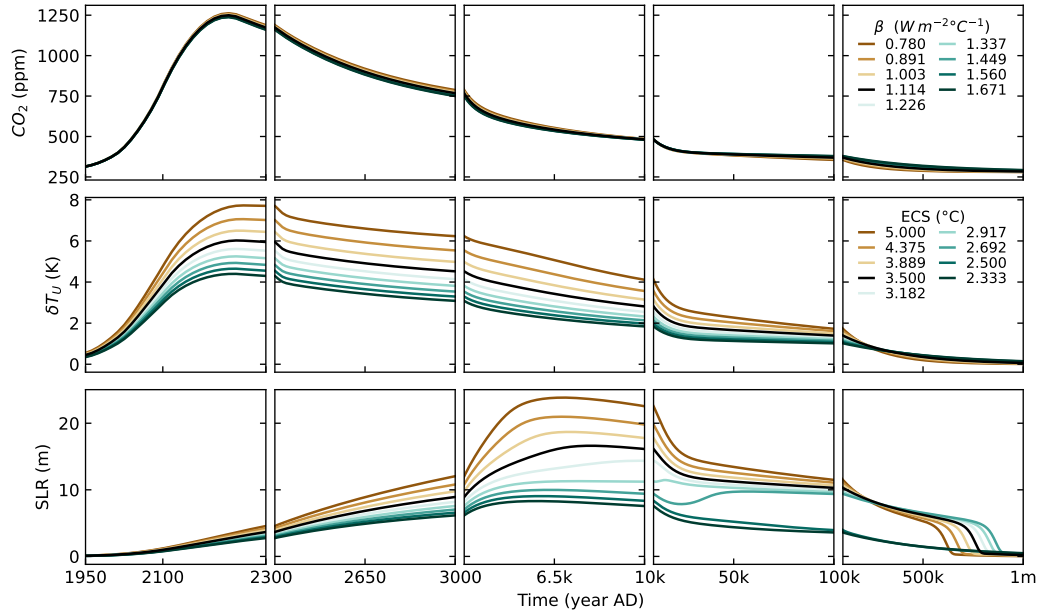
Figure D8. Atmospheric CO_2 concentration, surface temperature, and total sea level rise simulated by SURFER v3.0 under the SSP3-7.0 scenario for different values of β. The equilibrium climate sensitivity of SURFER v3.0 is related to β through ECS $= F_{2\times}/\beta$. Black lines indicate outputs simulated for the default parameter values, as described in section 2.4.1.